An Experimental Exploration of Low-Cost Sensor and Vehicle Model Solutions for Precision Ground Vehicle Navigation

by

Daniel Cody Salmon

A thesis submitted to the Graduate Faculty of
Auburn University
in partial fulfillment of the
requirements for the Degree of
Master of Science

Auburn, Alabama
December 12, 2015

Keywords: Sensor Fused Navigation; Closely Coupled Extended Kalman Filter; Vehicle Odometry; Vehicle Dynamic Model; Complementary Covariance

Approved by

David Bevly, Chair, Professor of Mechanical Engineering
John Y. Hung, Professor of Electrical and Computer Engineering
Peter Jones, Professor of Mechanical Engineering

Abstract

This thesis presents the use of a vehicle dynamic model (VDM) in conjunction with standard vehicle safety sensors to assist a low-cost Inertial Measurement Unit (IMU) and low-cost Global Positioning System (GPS) for fused precision ground vehicle navigation. Current production vehicles are outfitted with a multitude of sensors that are essential to safety packages such as: Electronic Stability Control (ESC), navigation, Adaptive Cruise Control (ACC), and lane tracking. The research presented in this thesis focuses on the sensors used with ESC and navigation, i.e. Wheel Speed Sensors (WSS), Steer Angle Sensors (SAS), IMU, and GPS. Each of the proposed measurement systems is plagued with detrimental characteristics that prevent standalone high precision and robust ground vehicle localization. The benefits of fusing GPS and an Inertial Navigation System (INS) are well documented, therefore a baseline GPS/INS localization algorithm based on well known literature is created. The benchmark system is used as a comparison medium in order to directly quantify performance of the localization algorithm utilizing VDM measurements.

Initial research demonstrates improvements in performance of the GPS/INS/VDM localization algorithm over the benchmark GPS/INS algorithm. However, the GPS/INS/VDM algorithm demonstrates degraded performance in comparison to the GPS/INS algorithm during a few driving scenarios. A constant covariance for the VDM measurements in the EKF causes the localization algorithm to drift in moments of high dynamics. Further analysis of all measurement systems leads to the development of a Complementary Covariance Filter (CCF) for the VDM measurements that allows the localization algorithm to weight the VDM measurement update accordingly during periods of high dynamics. With the CCF improvements, the updated GPS/INS/VDM algorithm is able to achieve improved or at least equivalent performance over the baseline GPS/INS localization solution for all situations.

This demonstrates that the inclusion of the VDM system along with ESC sensors provides an optimal low-cost ground vehicle localization solution when considering production cost and performance.

Acknowledgments

There are many people to thank that helped me get to this stage in both my education and my life. My entire family has played an imperative role in guiding and pushing me to achieve my goals. My mother, father, and grandparents have continuously supported major decisions throughout my academic career and taught many unforgettable lessons that have shaped me into the person I have become. I would also like to thank my sister, Nikki, for always being there for me no matter what the situation. I would like to thank many of my friends and classmates, but one in particular, Kyle Otte, assisted me in the decision to pursue a graduate degree. I would also like to thank all of the members of Central Alabama Mountain Peddlers, each of you have helped me pursue my passions outside of the office and classroom.

Academically, I would like to specifically thank Dr. David Bevly for advising me through this process of graduate school and the final stages of my undergraduate career. Additional thanks go out to all of my engineering professors, especially those in the Mechanical Engineering Department who taught me how to find the answers to the questions that we face not only in the classroom but in life. Thanks goes out to all of the great men and women that I worked alongside during my Co-op at AMRDEC. The work environment at AMRDEC led me to the realization that I was not fully prepared for the type of job I desired upon completion of my undergraduate degree. I would like to also thank Jerry Ray from AMRDEC who allowed me many opportunities to gain a great deal more valuable experience than a standard Co-Op employment might include. Additionally, I wish to acknowledge my committee, Dr. John Hung and Dr. Peter Jones, for their oversight of this thesis.

I would like to thank the members of the GPS and Vehicle Dynamics Laboratory for their collaboration and background knowledge that was provided on not only this project

but all projects I worked on during graduate studies. Particular thanks is expressed to Scott Martin for assisting me in many of my projects and helping me to gain knowledge that specifically applies to much of this thesis. Special thanks also goes out to Jonathan Ryan for giving me direction and guidance during my undergraduate research for the GAVLAB. Above all else, I would like to give thanks to the Lord Jesus Christ for placing the opportunities and people in my life that led me to this point.

Table of Contents

List of Figures

List of Tables

List of Symbols and Abbreviations

δt	Time Sample Rate
$\dot{\rho}_s$	Measured Pseudo-Range Rate to Each SV
$\hat{\dot{\rho}}_s$	Estimated Pseudo-Range Rate to Each SV
$\hat{\rho}_s$	Estimated Pseudo-Range to Each SV
λ	Longitude, $^\circ$
λ_{L1}	Wavelength of the L1 Carrier Frequency
ω_b	Gyroscope Measurements in the Body Frame
ω_e	Earth Rotation Rate
Φ	Geocentric Latitude, $^\circ$
ϕ	Roll of Vehicle WRT Local Tangent-Plane
Φ_k	Discrete State Transition Matrix
ψ	Yaw of Vehicle WRT Local Tangent-Plane
ρ_s	Measured Pseudo-Range to Each SV
τ_{acc}	Accelerometer Modeled Time Constant
τ_{gyr}	Gyrometer Modeled Time Constant
θ	Pitch of Vehicle WRT Local Tangent-Plane
B	Noise Vector Mapping Matrix

b_{cdft}	GPS Clock Drift Error
b_{cerr}	GPS Clock Offset Error
c	Speed of Light
$C_{\delta z}$	Covariance of the Measurement Innovations or Normalizing Value
C_b^e	ECEF to Body Frame Transformation Matrix
CCF	Complementary Covariance Filtering
e_{wgs}	WGS84 Eccentricity
f_d	Doppler Frequency
f_b	Accelerometer Measurements in the Body Frame
f_e	Specific Force in the ECEF Frame
g_b^e	Gravity Model Based on ECEF Position
H	Measurement Model Matrix
h	Height, m
L	Geodetic Latitude, $^\circ$
P	State Covariance Matrix
P_e	ECEF Position of the Vehicle
P_{S_e}	ECEF Position of Each Satellite Vehicle
Q	State Uncertainty due to Gaussian Noise Corruption (System Noise Covariance Matrix)
R	Measurement Covariance Matrix

R_0	WGS84 Equatorial Radius
$R_E(L)$	Transverse Radius of Curvature WRT Geodetic Latitude
$R_N(L)$	Meridian Radius of Curvature WRT Geodetic Latitude
u_S^e	ECEF Line-of-Sight Unit Vector
V_e	ECEF Velocity of the Vehicle
V_{S_e}	ECEF Velocity of Each Satellite Vehicle
X	Error State Vector
y	Normalized Measurement Innovations
z	Measurement Innovation
FDE	Fault Detection and Exclusion
RTK	Real-Time Kinematic
WRT	With Respect To

Chapter 1

Introduction and Background

Precision ground-vehicle localization and navigation utilizing sensor fusion has been around for years. However, as autonomous navigation technology becomes more prevalent on consumer vehicles, the need for a high-accuracy low-cost pose solution is increasing. Precision automotive localization has always required an expensive sensor set for true robustness and reliability. However, as research into vehicle safety control features has progressed, the sensors necessary for localization and navigation are becoming standard on many vehicles. Individuals purchasing a vehicle at this day and age expect to see safety features including but not limited to Anti-lock Brakes (ABS), Traction Control (TC), and Vehicle Stability Control (VSC). These technologies require the vehicle to have sensors that can be used in aiding a Global Positioning System (GPS) in overcoming deficiencies such as slow update rate and environmental dependencies. Inertial Measurement Units (IMU) consisting of three directional accelerometers and three directional gyroscopes are standard in GPS aiding sensor fusion; however, IMUs that are affordable enough to come standard on consumer vehicles are exceptionally noisy and usually are not full 6-Degree of Freedom (DOF). Many VSC systems only use longitudinal and lateral accelerometers and a yaw gyro due to cost and the motion constraint assumptions of an Ackerman steer vehicle. Other standard vehicle sensor sets may also be used to model vehicle dynamic behavior and predict navigation updates to assist GPS measurements. Wheel speed and steer angle sensors are significantly cheaper than a quality IMU and can be used along with known vehicle parameters and a vehicle dynamic model (VDM) to aid GPS/INS navigation yielding a GPS/INS/VDM system. This research uses direct experimental comparison to attempt to identify the advantages and disadvantages of each system in order to distinguish the best solution based on cost and accuracy.

1.1 Prior Research

The goal of this thesis is to experimentally analyze multiple methods of assisting a closely coupled GPS/INS navigation solution with standard vehicle safety sensors and a vehicle dynamic model. Many authors have analyzed various types of solutions in this field of study. Reviews of the research work found prior to assembling this thesis can be found in the following subsections.

1.1.1 GPS/INS Overview and Variations

GPS/INS integration has been around for years and studied in depth by many researchers. A robust and accurate 6-DOF navigation solution is achievable when expensive, high quality sensors are available. An in depth overview of the sensors, sensor characteristics, and algorithm architecture options can be found in [4]. Martin gives an in depth explanation of a closely coupled GPS/INS algorithm and its advantages, when combined with Differential Real Time Kinematic (DRTK) GPS, for automated vehicle convoy positioning in [8]. Elkaim's work in [9] comes a little closer to the research presented by this thesis in examining and comparing low-cost sensors for multiple applications of GPS/INS for vehicle navigation.

1.1.2 GPS/INS Aided by Odometry

The most common use of vehicle odometry (i.e. wheel speed sensors), is as a simple longitudinal velocity measurement without applying a dynamic or kinematic vehicle model. Eric Abbott, David Powell, and Yukihiro Kubo were some of the first researchers to publish studies on the ability to aid GPS/INS navigation with the integration of wheel speed sensors in [10] and [11] respectively. These papers predominately focused on limiting the error growth present in INS during GPS outage by using the wheel speed sensors to estimate vehicle velocity only in the longitudinal direction. In 2001, Gamini Dissanayake described a technique for aiding GPS and low-cost IMU's with wheel speed sensors and non-holonomic

constraints in the vertical and lateral direction [12]. The non-holonomic constraint assumes zero velocity in a given direction, which is a false assumption for the lateral direction of the vehicle even under low dynamic maneuvers. Jianchen Gao, from the University of Calgary, has published multiple articles in recent years that describe different techniques for integrating on-board vehicle sensors with a GPS/INS system for improved navigation capabilities. Gao's 2006 conference paper [13] discusses a technique for combining the measurements from vehicle wheel speed sensors with non-holonomic constraints in the lateral and vertical direction to aid GPS/INS. Gao claims greater than 75% improvement in the position and velocity solution of the GPS/INS/WSS navigation algorithm over the GPS/INS algorithm. Taking into consideration the fact that Gao is using a HG1700 tactical grade IMU for all algorithms makes the 75% improvement over the GPS/INS localization especially significant. Gao also presents methods for including a yaw rate sensor in the GPS/INS/WSS navigation algorithm in [13], but the yaw rate sensor adds negligible gains in benefits in comparison to wheel speed sensor aiding. Gao published a second paper [14] later in 2006 that attempts to improve the original paper's solution by removing the non-holonomic constraint by aiding the navigation algorithm with G sensors to measure lateral and longitudinal specific force. Gao uses the added sensors to decompose the wheel speed sensor measurements into longitudinal and lateral velocities whenever the side slip angle is greater than 7°. The G sensor aiding method is proven to outperform the non-holonomic constraint method. Finally, Gao presented a paper in 2007 [15] in which a low-cost IMU was used rather than the HG1700 tactical grade IMU. A 90% improvement was claimed when utilizing the wheel speed sensor data over the GPS/INS system. The system improves to greater than 92% when using all sensors available in this research in order to detect when the non-holonomic constraint assumptions are violated. In 2010, Toa Li, also from the University of Calgary, published further research in GPS/INS aiding through wheel speed sensors in [16]. Li uses the wheel speed sensors and non-holonomic constraints in the vertical and lateral direction to derive three dimensional velocity updates. Li was using a reduced order IMU (i.e. lateral and

longitudinal accelerometers and a yaw gyro) in the research to demonstrate improved performance when taking advantage of the available wheel speed sensor measurements. During the same year, Somieski published research comparing navigation solutions aiding a single-frequency GNSS receiver with differential wheel speed calculations versus a combination of wheel speed sensors combined with a gyroscope [17]. Somieski was able to prove that the gyro plus wheel speed aiding yielded highly improved results through experimental data in [17]. Finally, in 2013, Andrew Hazlett published a masters thesis describing a GPS/INS navigation aided by differential wheel speed sensors as shown in [18] and [19]. Hazlett uses the difference between the speed of the left and right rear wheels to determine a yaw rate as well as a vehicle velocity, and he was able to present improvement over the GPS/INS only algorithm through simulation results of an extended kalman filter and unscented kalman filter implementations.

Much of the research related to aiding a navigation solution with wheel odometry attempts to take advantage of non-holonomic velocity constraints given the nature of the motion of an Ackerman steer vehicle. In 2011, Ryan proved that these constraint assumptions are false even in low dynamic situations [2], which showed that non-holonomic lateral velocity constraints fail as soon as the vehicle experiences a slight change in yaw.

1.1.3 Vehicle Model and Sensor Aided Navigation

Alternatively to the prior work of the authors listed in Section 1.1.2, this thesis utilizes a dynamic vehicle model along with the wheel speed sensors and steer angle sensor to improvement the GPS/INS solution. Many authors have performed previous research into the benefits of aiding a navigation solution with a vehicle model. Bonnifait published [20] concerning experimental research on the advantages a localization system using GPS, wheel speed sensors, and steer angle sensors. Bonnifait's work explores the advantages to using a dynamic model, or odometric technique, against using differential odometry of the rear wheels only and a kinematic model. Bonnifait proves significant improvement in dead

reckoning capabilities with the dynamic model versus the kinematic model. However; this technique suffers from many errors, as will be discussed later in this thesis, when considering full 6 degree of freedom localization. Similar approaches to Bonnifait can be seen in [21] and [22]. In 2003, Xin Ma published research aiding GPS/INS with a vehicle kinematic model that used both wheel speed sensors and steer angle sensors as seen in [23]. Ma concluded from the research that the heading solution from the kinematic model proved to be less accurate than the heading solution derived from the IMU measurements.

The previously described vehicle models assume planar motion by only accounting for longitudinal velocity, lateral velocity, and heading. Travis demonstrated a method for accounting for the body roll dynamics and body pitch dynamics of the vehicle within the dynamic model in 2006 [24]. Travis also researched the effects of vehicle side slip and wheel slip on ground vehicle navigation in the masters thesis [24].

Further variety of applications for the type of research presented in this thesis can be seen in [25]. Lie aids a GPS/INS navigation solution with a low-fidelity model of an aircraft's dynamics in order to estimate the the aircraft airspeed, angle of attack, and sideslip angle without the use of a pitot-static system or angle of attack/sideslip vanes. Further research into using a vehicle dynamic model to aid in aircraft navigation was recently published by Crocoll in [3]. Crocoll attempts to present an improved method for combining the aircraft's vehicle model with IMU data in the prediction step of the Kalman filter. Crocell's research is an attempt to use a unified model method to computationally simplify a technique used to deal with multiple models in filtering published by Koifman and Bar-Itzhack in [26].

1.2 Contributions

The focus of the research presented in this thesis is the experimental analysis of aiding a low-cost GPS/INS EKF localization system with measurements from a standalone dynamic vehicle model utilizing the measurements from standard vehicle safety sensors. Taking that into consideration, the following contributions to the field of study are made:

- Determination if the vehicle model and vehicle safety sensors are of benefit in comparison to a GPS/INS system. The initial results were presented by the author of this thesis at the Institute of Navigation Position, Location, and Navigation Symposium in May 2014 [27].

- Determination of the optimal vehicle model to use in the navigation algorithm when considering complexity and desired performance.

- Comparative analysis of multiple navigation algorithms using real world collected data to determine the optimal sensor set and algorithm when considering cost and accuracy.

- Development of a complementary covariance algorithm for the measurements generated by the dynamic vehicle model utilizing the vehicle safety sensors'.

Chapter 2

Vehicle Model and Navigation Sensors

2.1 Vehicle Sensing Capabilities

Autonomous vehicles are typically outfitted with a multitude of sensors. This thesis focuses on navigation systems incorporating GPS, inertial measurement units, and whether or not that solution can be improved with the aiding of standard vehicle safety sensors and a vehicle dynamic model. The following is an introduction to these sensors and their capabilities.

2.1.1 Global Position System

GPS consists of three segments including the space segment, the control segment, and the user segment which combine to provide users with accurate position, velocity and time. The space segment is composed of a minimum of 24 satellites in six orbital planes. Generally there are approximately 32 satellites in orbit, oriented to allow users to have a clear line of sight to at least four satellites at any given time. The control segment is based at Schriever Air Force Base (AFB) in Colorado Springs, Colorado with additional monitoring stations around the Earth and is tasked with maintaining satellite orbits and accurate timing for the system. The user segment is the GPS receiver which tracks radio signals broadcast by each GPS satellite [28]. GPS satellites transmit on three frequencies in the L band: L1 at 1575.42 MHz, L2 at 1227.60 MHz and L5 at 1176.45 MHz. Each transmitted signal contains a ranging code and navigation message modulated on a sinusoidal carrier.

The ranging codes are pseudo-random binary sequences unique to each satellite and are referred to as pseudo-random noise (PRN) codes. The PRN codes are selected to be orthogonal to one another allowing a receiver to access various satellite signals broadcast

at the same frequency through Code Division Multiple Access (CDMA) [6]. Both military and civilian ranging codes are modulated on the L1 and L2 carrier frequencies. The civilian ranging code, called the Course Acquisition (C/A) code, is 1023 chips long and repeats every one millisecond. The military ranging code, or P code, is much longer, 6.1871×10^{12} chips, and is broadcast at ten times the rate of the C/A code. Encryption of the P code limits the availability of the signal to military users with access to the encryption key. Originally, the L2 carrier was modulated with only the encrypted P code making it unavailable to civilian users. The launch of Block IIR-M satellites beginning in 2005 marked the introduction of the L2C ranging code providing civilian users with dual frequency capabilities [29]. Despite the fact that the L2C code is available on a limited number of satellites in the constellation, many civilian users can now access L2 P coded signals through semi-codeless tracking techniques [30].

The navigation message provides the user with satellite information and the signal transmission time [31]. Satellite information includes almanac data, ephemeris data, and satellite health which allow the user to determine the satellite's position and velocity. The distance from a given satellite to the receiver is calculated from the time of flight (TOF) of the signal. The TOF formulation relies on a receiver generated replica of the ranging code. The replica is shifted in time to match the satellite transmitted ranging code. With perfect time synchronization between the satellite clock and the receiver clock, the time shift is due to the TOF of the signal. The range from the receiver to the satellite is equal to the TOF times the speed of light. The user's position is then constrained to a sphere centered at the satellite's position with a radius equal to the measured range. With three accurate measurements, the user's position can be determined by trilateration. However, the measured range is corrupted with timing errors due to the inaccuracy of both the satellite and receiver clocks and is therefore referred to as the pseudo-range measurement. Satellite clock corrections terms are transmitted with the ephemeris data and are used to significantly

reduce the error introduced by the satellite clock. By including a fourth measurement, the user estimates a three dimensional position and the range bias due to the receiver clock error.

GPS errors are not limited to satellite and receiver clock errors. Additional error sources include but are not limited to satellite ephemeris errors, propagation delays due to the atmosphere, multipath and receiver noise. Satellite ephemeris errors result from inaccurate information in the transmitted navigation message and lead to ranging errors of approximately 2.1 meters on average. Atmospheric delays are attributed to two layers of the atmosphere: the ionosphere and the troposphere. Ionospheric delays are typically the dominant GPS error source resulting in average range errors of 4.0 meters without accurate modeling. The tropospheric delays are less severe with associated range errors of approximately 0.5 meters. Multipath, which is the error due to reflected GPS signals, and receiver noise contribute additional range errors of approximately 1.0 meter and 0.5 meters respectively. The cumulative effect of these errors and the residual satellite clock error is a range error with a standard deviation of 5 meters. For a typical satellite geometry, this error will result in horizontal position errors near 10 meters and vertical position errors near 13 meters [28] [8].

2.1.2 Inertial Measurement Unit

Inertial Measurement Units (IMU) are comprised of a combination of accelerometers and gyroscopes providing measurements of specific force and angular velocity about the units sensitive axes hundreds of times per second. The IMU may be mounted in a strapdown or gimbaled configuration with most modern applications using the strapdown approach. IMUs are available in a variety of grades ranging from automotive to marine with a wide range of accuracy and stability.

In principle, an accelerometer measures the displacement of an internal proof mass relative to the IMU case caused by an externally applied force. For a sensor in free fall near the surface of the Earth, the acceleration due to gravity is experienced by the proof mass and IMU case resulting in a measurement of zero acceleration (neglecting drag effects).

The same sensor on the surface of the Earth measures the force of the Earth pushing up on the IMU case and not on the proof mass. Therefore, accelerometers are said to measure the specific force acting on the unit. Accelerometers used in strapdown applications are commonly either pendulous or vibrating beam [4].

Gyroscopes measure the rate of change of the angular position of the IMU about a sensitive axis. Common gyroscopes include spinning mass, optical, and vibratory devices. These sensors operate on principles such as the conservation of angular momentum, the Sagnac effect, or Coriolis acceleration. Additional information on gyroscope operation is available in [4].

IMU errors include but are not limited to scale factor errors, misalignment errors, biases, and random noise. The accelerometer and gyroscope biases are often the dominant errors sources of a low-cost IMU. The bias term is composed of a static turn-on bias and a dynamic in-run bias. Table 2.1 shows typical bias values for various IMU grades as given in [4] [8].

Table 2.1: Typical Accelerometer and Gyro Biases for Different Grades of IMU (From: [4])

IMU Grade	Accel Bias (m/s^2)	Gyro Bias ($^\circ/hr$)
Marine	10^{-4}	0.001
Aviation	$3 \times 10^{-4} - 10^{-3}$	0.01
Intermediate	$10^{-3} - 10^{-2}$	0.1
Tactical	$10^{-2} - 10^{-1}$	$1 - 100$
Automotive (MEMS)	> 1	> 100

2.1.3 Vehicle CAN Bus

The vehicle Controller Area Network(CAN) bus has been set as the standard for ground vehicle data acquisition. Further information describing the selection of this standard can be found in [32]. This thesis focuses primarily on the addition of the Anti-lock Braking System (ABS) Wheel Speed Sensors (WSS) and the Vehicle Stability Control (VSC) Steer

Angle Sensor (SAS). The ABS system is in place to prevent wheel slip under heavy braking. Large wheel slip induces a lower effective friction coefficient between the vehicle tire and road surface, which in turn increases the minimum stopping distance for any given speed. Current vehicle ABS systems incorporate wheel speed sensors for increased accuracy especially at low speeds which is essential for vehicles equipped with a Traction Control System (TCS). The wheel speed sensors are proximity sensors that react to changes in the magnetic field in order to detect forward and backward movement. The VSC steer angle sensor is usually mounted to the steering shaft and consists of two potentiometers offset by 90°. These two potentiometers allow the sensor to cover one full steering-wheel turn and then the values are repeated after ±180°. The steer angle sensor uses this information to maintain knowledge of the number of steering wheel revolutions as well as the angle.

The sensor errors present within the wheel speed sensor and steer angle sensor systems are minimal compared to the errors present in converting the sensor output to desired measurement. The wheel speed sensors simply give a measurement for the angular rotation of each of the four wheels. An accurate estimate of the wheel radius is required in order to calculate the longitudinal velocity of each wheel. Wheel slip is the other main source of error when calculating vehicle speed based on wheel speed sensors.Wheel slip is unobservable without the use of external sensors.

The steer angle sensor outputs a measurement of the steering wheel angle, but the wheel angle at the tire with respect to the direction of the vehicle is the desired value for navigation calculations. The ratio between the two values can be approximated as linear with a scaling factor, but the unknown errors in the manner in which steering linkages react to each other still exist. Roll and other motion can also change the ratio. The steer angle measurement can also be plagued by errors due to wheel misalignment although these errors can be estimated with GPS [2].

2.2 Vehicle Model Variations

The most prevalent model used to describe vehicle dynamics is the bicycle model. The three basic variations of the bicycle model are the kinematic model, the lateral model, and the four-wheel model as shown in Figure 2.1, Figure 2.2, and Figure 2.3 respectively. The kinematic model relies on the assumption of zero lateral tire velocity i.e. slip angles of zero at each tire at all times. The lateral velocity assumption is rendered false as a vehicle generates speed or begins any turn maneuver [1]. The lateral dynamic vehicle model differs from the kinematic model by compensating for the lateral tire slip angles of the front and rear tire as represented by α_f and α_r respectively in Figure 2.2. The lateral bicycle model still has limitations as the model is unable to account for the roll angle of the vehicle. In situations where the roll angle of the vehicle is of greater concern, the four wheel dynamic bicycle model can be used [24]. This thesis focuses primarily on the two-wheel and four-wheel dynamic vehicle model. Further explanation of general vehicle dynamic modeling and vehicle dynamics concepts can be found in [33].

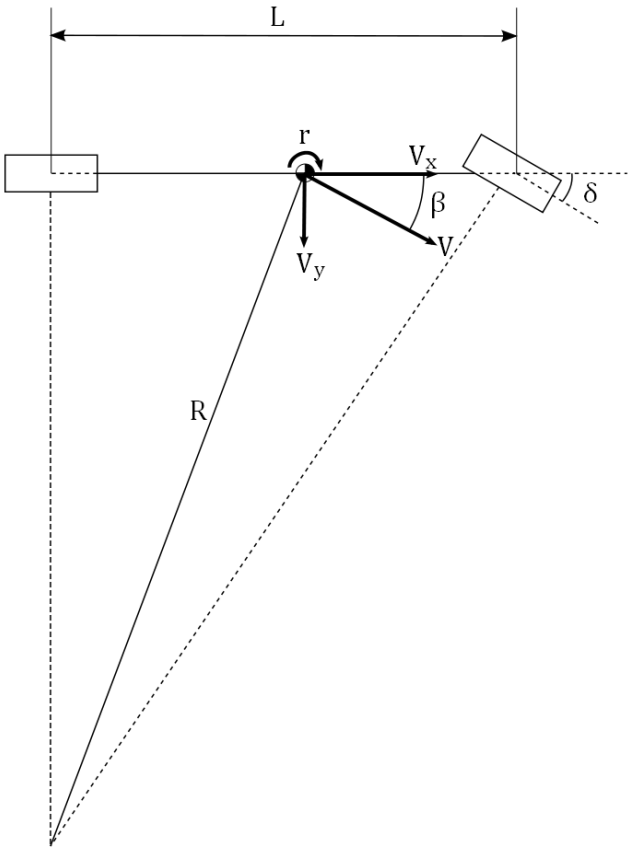

Figure 2.1: Kinematic Bicycle Model [1]

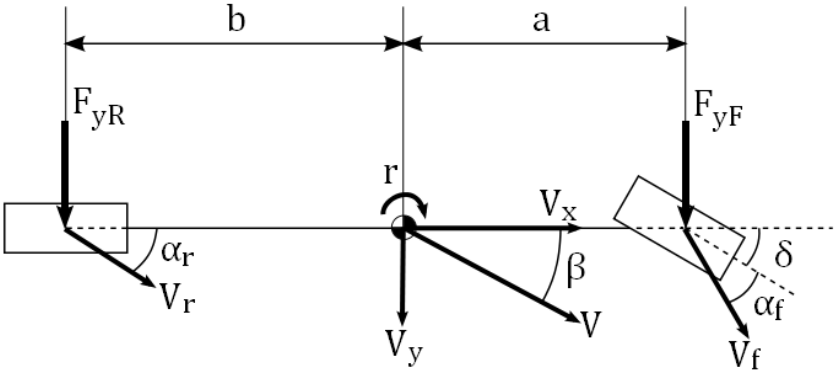

Figure 2.2: Lateral Dynamic Bicycle Model [1]

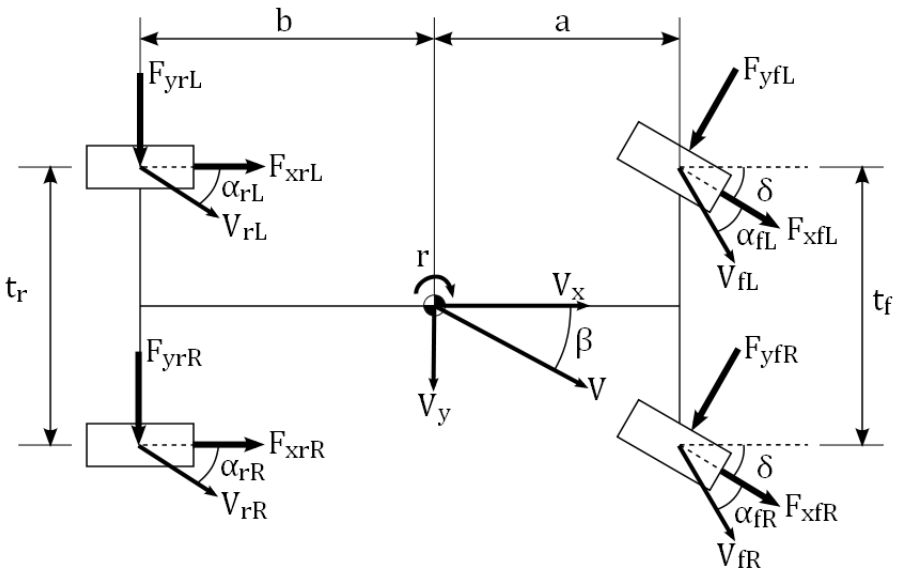

Figure 2.3: Four Wheel Bicycle Model [1]

2.3 Dynamic Vehicle Model Development

The initial studies by the author of this thesis into aiding a GPS/INS navigation system with a dynamic vehicle model were presented in [27]. This early work was performed under the assumption that the most accurate and detailed vehicle model possible was a necessity. The initial design took advantage of the four-wheel vehicle model in order to calculate measurements of all six degrees of freedom (DOF) for the vehicle body. The main benefit of the six DOF dynamic model lies in the ability to calculate the weight distribution of the vehicle body based on the dynamics the vehicle is undergoing. Vehicle body roll and pitch are exceptionally important when considering vehicle safety and rollover prevention, but these values are relatively insignificant from a localization and navigation stand point. The initial work presented in [27] also utilized a nonlinear tire model in order to use the vehicle measurements used for navigation.

The vehicle model utilized in the research presented by this thesis is far less complex than the six DOF, nonlinear model described in [27]. The first assumption taken advantage of in simplifying the dynamic vehicle model is that a vehicle never leaves the linear region

of the tire curve during general vehicle maneuvering. Therefore, foregoing the nonlinear tire model for a linear version was an easy simplification that yielded comparable results for the navigation calculations. The tire cornering stiffness, C_α, is experimentally determined from data collected by a 3 antenna GPS receiver described in Section 3.3.1. The 3 antenna GPS receiver allows for accurate calculation of both the yaw of the vehicle and the course of the vehicle. The vehicle must experience high dynamics in order to excite the higher lateral forces of the linear region of the tire curve. Therefore, the high speed data collection was performed in the enclosed track owned by Auburn University's National Center for Asphalt Technology. The experimental tire curve's for the front and rear tire can be seen in Figure 2.4 and Figure 2.5 respectively. These tire curves yield approximate tire cornering stiffness values of $600N/deg$ and $950N/deg$ for the front and rear tires respectively which are utilized in the vehicle dynamic model measurement calculations.

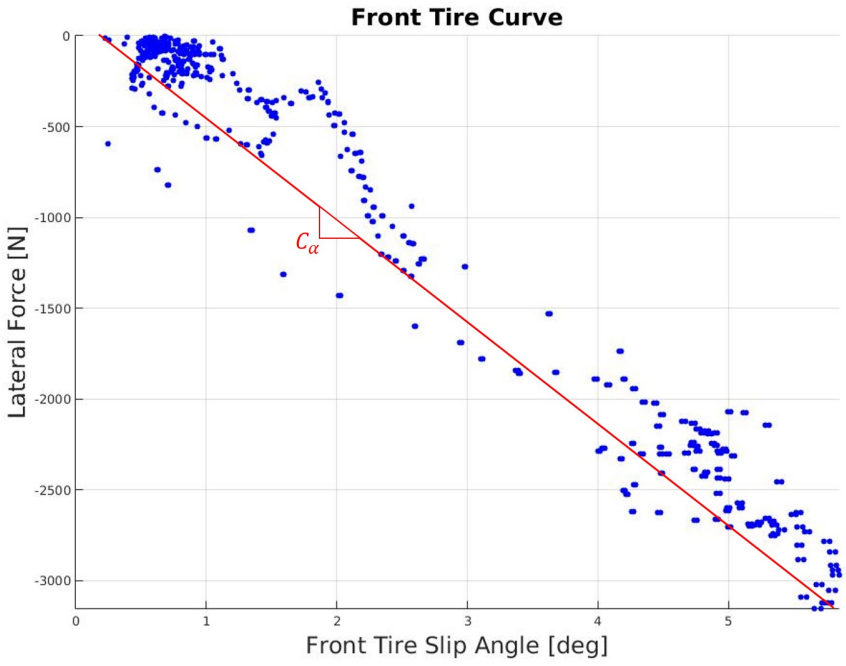

Figure 2.4: Front Tire Curve

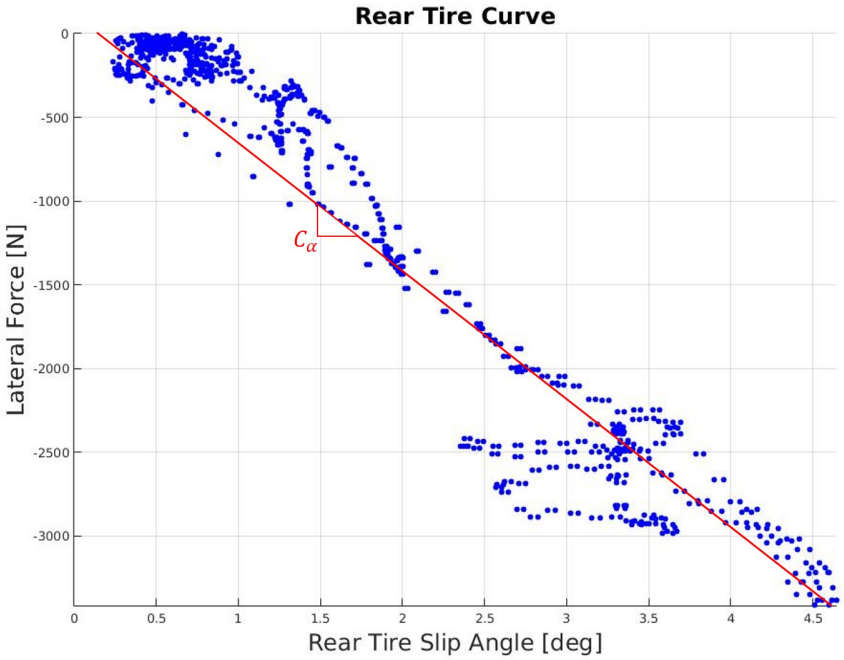

Figure 2.5: Rear Tire Curve

The yaw of the vehicle gives the instantaneous direction in which the vehicle is directed in the east north frame while the course measurement gives the instantaneous direction of the velocity vector of the vehicle also in the east north frame. This concept is visually demonstrated by Figure 2.6 and the conclusion can be made that when the velocity of the vehicle is purely in the longitudinal direction then the vehicle course and yaw measurements will be equivalent since there is zero sideslip.

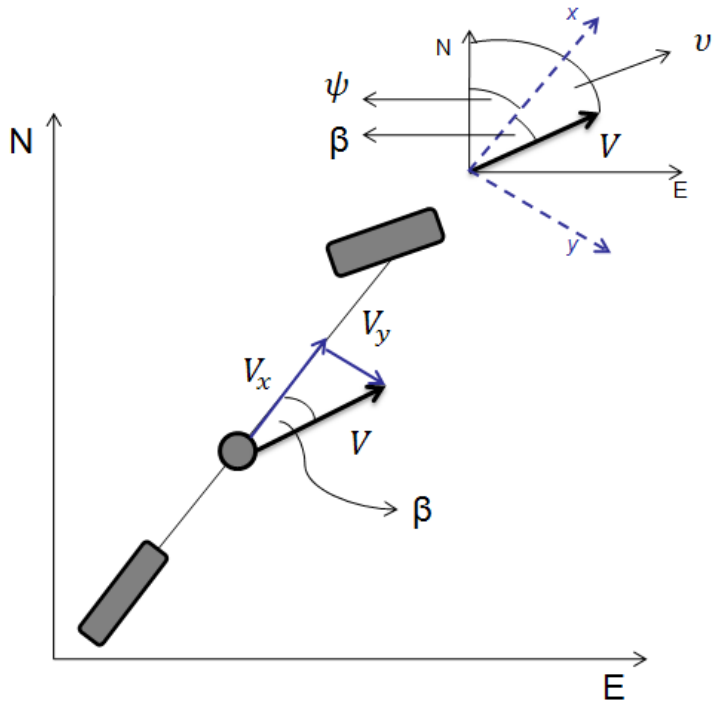

Figure 2.6: Sideslip Visualization [2]

Also, the availability of two dead reckoning sensors in a GPS/INS/VDM navigation filter allows optimization by more heavily weighting IMU measurements during moments of high dynamics, which will be shown in Chapter 4. The second simplification of the dynamic vehicle model is the conversion of the four-wheel model to the two-wheel model as seen in Figure 2.7. This simplification takes advantage of the availability of wheel speed measurements at all four wheels and combining the inner and outer wheels by axle after the tire forces at each wheel are calculated.

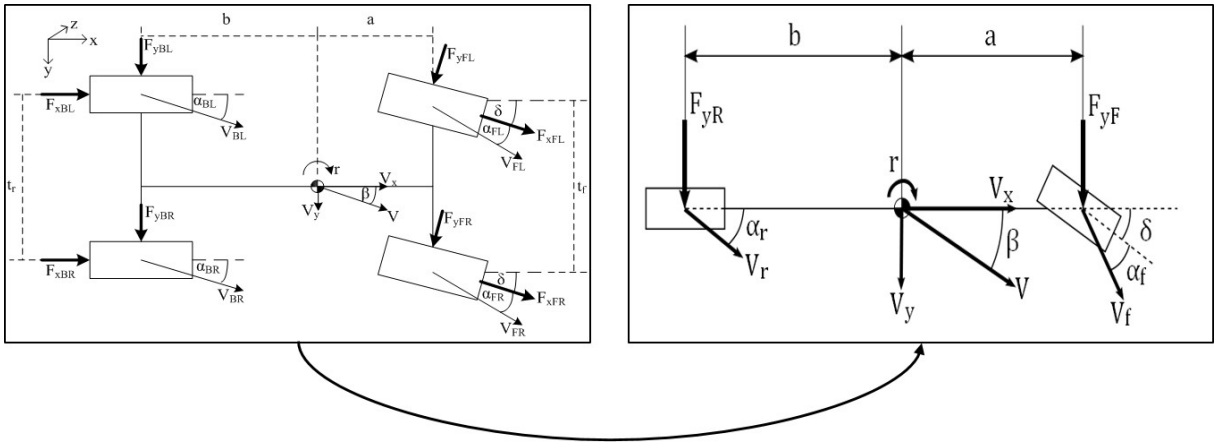

Figure 2.7: Four Wheel to Two Wheel Bicycle Model

The dynamic vehicle model initializes by calculating the slip angle of each wheel using Equation (2.1).

$$\alpha_{FR} = atan\left(\frac{V_y + (a * r)}{V_x - \left(\frac{t_f}{2} * r\right)}\right) - \delta \tag{2.1a}$$

$$\alpha_{FL} = atan\left(\frac{V_y + (a * r)}{V_x + \left(\frac{t_f}{2} * r\right)}\right) - \delta \tag{2.1b}$$

$$\alpha_{BR} = atan\left(\frac{V_y + (b * r)}{V_x - \left(\frac{t_f}{2} * r\right)}\right) \tag{2.1c}$$

$$\alpha_{FR} = atan\left(\frac{V_y + (b * r)}{V_x + \left(\frac{t_f}{2} * r\right)}\right) \tag{2.1d}$$

The parameters seen in Equation (2.1) are visually described by Figure 2.3. The lateral tire force is then calculated as a linear function of the tire cornering stiffness, C_α, and the tire slip, α, at each tire as seen in Equation (2.2).

$$F_{lat} = -C_\alpha * \alpha \tag{2.2}$$

After calculating the lateral tire force at each wheel, the forces are combined by axle to yield the two-wheel bicycle model seen in Figure 2.2. Following the simplification of the four-wheel model to a two wheel model, the yaw acceleration, $\ddot{\psi}$ or $\dot{r}$, is calculated using Equation (2.3).

$$\ddot{\psi}_{k+1} = \dot{r}_{k+1} = \frac{a * F_{yF} * cos(\delta) - b * F_{yR}}{I_z} \tag{2.3}$$

The yaw acceleration is then numerically intergrated via the trapezoid method to yield the yaw rate as seen in Equation (2.4).

$$\dot{\psi}_{k+1} = r_{k+1} = r_k + \frac{\dot{r}_k + \dot{r}_{k+1}}{2} * \Delta t \tag{2.4}$$

The sideslip rate, $\dot{\beta}$, is then calculated using Equation (2.5),

$$\dot{\beta}_{k+1} = \frac{F_{yF} * cos(\delta) + F_{yR}}{m * V_x} - r \tag{2.5}$$

and then the sideslip rate is numerically integrated to yield the sideslip of the vehicle as seen in Equation (2.6).

$$\beta_{k+1} = \beta_k + \frac{\dot{\beta}_k + \dot{\beta}_{k+1}}{2} * \Delta t \tag{2.6}$$

The sideslip of the vehicle can then be used in Equations (2.7) and (2.8) to calculate longitudinal and lateral velocity of the vehicle respectively.

$$V_x = V * cos(\beta) \tag{2.7}$$

$$V_y = V * sin(\beta) \tag{2.8}$$

Where:

$$V = R_{eff} * \omega \tag{2.9}$$

The longitudinal and lateral velocity are the measurements required by the GPS/INS/VDM navigation filter that is described in detail in Chapter 4. Sensitivity to errors in tire parameter estimates can severely affect the accuracy of the the vehicle dynamic model navigation solution. However, GPS measurements can be used to accurately estimate the necessary tire parameters in an initialization or characterization step in a real time implementation.

Chapter 3

GPS and INS Sensor Fused Navigation

GPS has many advantages when considering localization and navigation with respect to a global reference frame. However, global positioning sensors also have limitations, especially when using lower priced units. The Novatel OEM star single board, single frequency GPS receiver, shown in Figure 3.1, is only capable of outputting a position, velocity, and time (PVT) solution at an update rate of $1Hz$ for the lowest cost version. There are also many factors, such as data collection environment, external interference, and weather, that can affect the quality of GPS measurements regardless of the quality and/or price of the receiver. In these cases, a separate sensor or set of sensors is used to aid the GPS receiver and overcome the limitations present in GPS based navigation. The most common solution to overcome GPS limitations is to aid the receiver with an Inertial Measurement Unit (IMU) and navigation processor referred to as an inertial navigation system (INS). An INS has many advantages for navigation, some of which are: a high output rate, reliable angular rate measurements which can be converted to attitude, reliable acceleration measurements which can be integrated to find velocity and position, and it is not affected by data collection environment, external interference, or weather. However, the INS is limited by IMU error as discussed in Section (2.1.2).

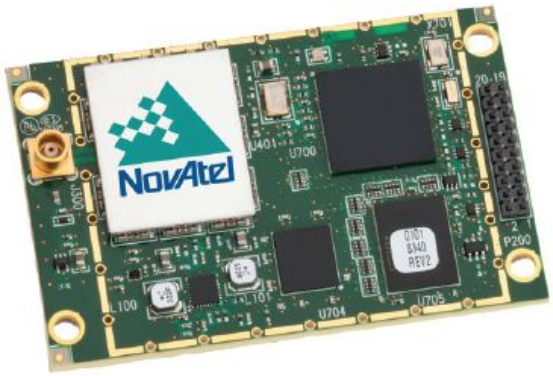

Figure 3.1: OEMstar single board, L1 only receiver

State estimation algorithms play an integral role in sensor fusion navigation algorithms. The Kalman filter is the base of many state estimation algorithms used for navigation [4]. However, the Kalman filter is intended for use on linear systems. Due to the nonlinearities present in INS alignment and calibration and the processing of ranging measurements for GPS, a nonlinear state estimation algorithm is required. Many solutions that deal with nonlinearities can be found in [4]. However, this thesis utilizes the extended Kalman filter (EKF). The system matrix and measurement matrix can be replaced by nonlinear functions in the time update and measurement update, which will be described in greater detail later in this chapter [4].

3.1 GPS and INS Integration Architectures

Multiple algorithm architectures are available for GPS/INS integration. The most commonly used architectures are often referred to as loosely coupled, closely/tightly coupled, and deeply coupled and increase in complexity in that order [4].

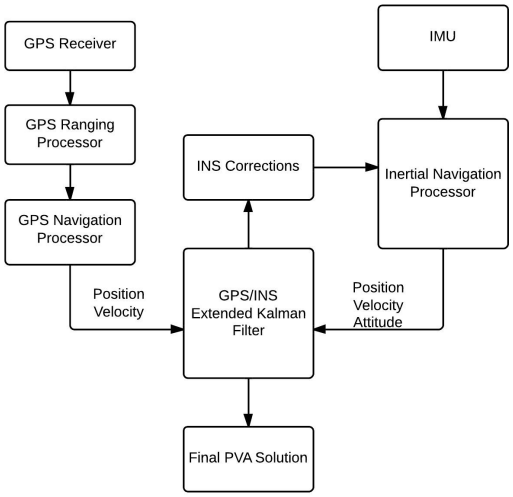

Figure 3.2: Loosely Coulpled GPS/INS Integration Architecture

The loosely coupled architecture has the advantage of being the simplest form of GPS/INS integration. The algorithm uses the position and velocity measurements output by the GPS receiver's navigation processor to directly compare to the position and velocity predicted by the inertial navigation processor. The loosely coupled architecture can be visualized in Figure 3.2. This simple architecture also has many drawbacks, the first and most significant of which is that no GPS position and velocity information is available to update the filter and limit INS drift unless at least four satellites are available to the GPS receiver. Also, a loosely coupled filter lacks the ability to monitor the measurement quality for each individual satellite. Therefore, a single bad measurement can degrade the overall PVT solution output by the GPS. A key benefit to using the Kalman filter as a state estimator is the ability to determine the proper weighting of multiple sensor measurements based on the confidence in the accuracy of each measurement. Few GPS receivers output reliable error covariance predictions which forces the assumption of a conservative GPS solution covariance, limiting the Kalman gain [4].

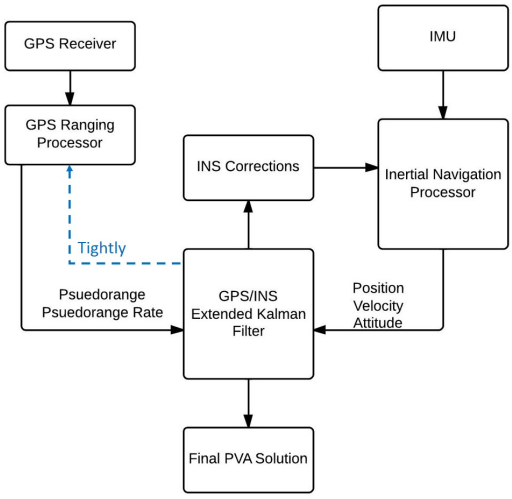

Figure 3.3: Closely/Tightly Coupled GPS/INS Integration Architecture

The closely and tightly coupled architectures overcome the most significant limitation of a more centralized loosely coupled filter by taking advantage of GPS information even in situations in which there are less than four satellites available to the receiver. The closely coupled Kalman filter is based on the inertial navigation solution and predicts pseudo-ranges and pseudo-range rates between the antenna and each satellite based on the calculated positions and velocities of the antenna and each satellite in view. The predicted pseudo-ranges and pseudo-range rates are compared to the respective measurements from the GPS ranging processor, which can be visualized in Figure 3.3. The closely coupled architecture also allows the implementation of fault detection and exclusion (FDE) algorithms to be performed on the measurements of each satellite separately. The closely coupled filter was chosen as the basis for all algorithms throughout this thesis due to the advantages outweighing the slight increase in complexity. The tightly coupled filter yields similar advantages but the complexity of adding a feedback loop to the GPS receiver to aid tracking loops is not feasible when utilizing the low-cost receiver unit.

The deeply coupled architecture, sometimes called ultra-tightly coupled, increases the ability of the navigation algorithm to use GPS aiding in scenarios of lower carrier to noise

levels on the GPS signals. The deeply coupled algorithm achieves this by feeding commands from the navigation filter into the GPS receiver as seen in Figure 3.4, which causes a drastic increase in the complexity of the algorithm.

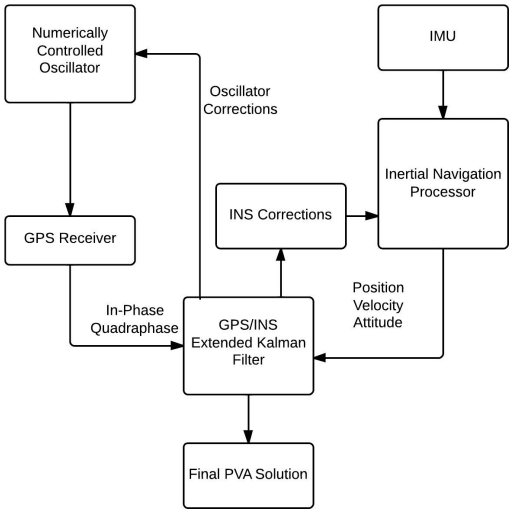

Figure 3.4: Deeply Coupled GPS/INS Integration Architecture

3.2 Closely Coupled GPS and INS Navigation Filter

The closely coupled architecture is thought by many to hold the greatest advantages for navigation when performance and complexity are both taken into consideration. The closely coupled extended Kalman filter used for the GPS/INS navigation algorithm in this research is a seventeen state system which consists of three degree of freedom (DOF) error states of position, velocity, and attitude as well as bias states for each of the six DOF of the IMU. The final two states of the EKF are the the GPS receiver clock error bias and the clock error drift. The navigation filter, which is based in the ECEF coordinate frame is described by the state vector seen in Equation (3.1).

$$X = [\ \delta P_e \quad \delta V_e \quad \delta \Psi \quad b_a \quad b_g \quad b_{cerr} \quad b_{cdft}\ ]^T \tag{3.1}$$

The position, velocity, and attitude states shown in Equation (3.1) are preceded by the delta function, δ, to demonstrate that this is actually an error state Kalman filter as well as the errors from linearizing. Therefore the initial nine states in the the state matrix are actually the error between the predicted and actual value for the given parameter. The final terms of the state matrix do not require the δ as these states are errors associated with the sensor measurements utilized by the navigation filter. The navigation filter consists of a continuous propagation step or time update which is then corrected by a measurement update whenever the data is available.

3.2.1 GPS/INS Time Update

Each of the seventeen states requires a mathematical model to describe the dynamics. Attitude information is maintained through the coordinate transformation matrix, C_b^e, described in Appendix (A). C_b^e is propagated forward in time through the precision attitude updates based on the three gyroscope measurements, ω_b, as shown in Equation (3.2).

$$C_b^e(+) = C_{earth} * C_b^e(-) * C_{b+}^{b-} \tag{3.2a}$$

$$C_{b+}^{b-} = I_3 + \frac{sin|\alpha_{ib}^b|}{|\alpha_{ib}^b|}[Skew(\alpha_{ib}^b)] + \frac{1 - cos|\alpha_{ib}^b|}{|\alpha_{ib}^b|^2}[Skew(\alpha_{ib}^b)]^2 \tag{3.2b}$$

$$\alpha_{ib}^b = \omega_b * \delta t \tag{3.2c}$$

$$C_{earth} = \begin{pmatrix} cos(\omega_e \delta t) & sin(\omega_e \delta t) & 0 \\ -sin(\omega_e \delta t) & cos(\omega_e \delta t) & 0 \\ 0 & 0 & 1 \end{pmatrix} \tag{3.2d}$$

The accelerometer measurements, f_b, are then converted from the body frame to specific force measurements in the ECEF frame, f_e, using Equation (3.3).

$$f_e = \frac{C_b^e(+) + C_b^e(-)}{2} * f_b \tag{3.3}$$

The ECEF frame velocity and position, V_e and P_e respectively, are calculated using trapezoidal numerical integration techniques as shown in Equations (3.4) and (3.5).

$$V_e(+) = V_e(-) + (f_e + g_b^e\,(P_e(-)) - 2[Skew(\omega_b)]V_e(-)) * \delta t \tag{3.4}$$

$$P_e(+) = P_e(-) + \frac{1}{2}\,(V_e(-) + V_e(+)) * \delta t \tag{3.5}$$

A model for the bias error states is used to propagate the states forward in time. The bias error for the accelerometer and gyroscope are modeled as a first order Gaussian Markov Process as demonstrated by Equations (3.6) and (3.7) respectively.

$$\dot{b}_{acc} = \frac{-1}{\tau_{acc}} b_{acc} + \nu_{acc} \tag{3.6}$$

$$\dot{b}_{gyr} = \frac{-1}{\tau_{gyr}} b_{gyr} + \nu_{gyr} \tag{3.7}$$

The time constants, τ_{acc} and τ_{gyr}, are set to $500s$ and $1300s$ respectively, based on experimental identification presented in [34]. The noise terms, ν_{acc} and ν_{gyr}, are modeled under the assumption of zero mean white Gaussian noise. Once all sensor measurements have been corrected to account for bias and converted to the desired ECEF frame, the extended Kalman filter propagation of error states, X, and state covariance, P, can be calculated as shown in Equations (3.8) and (3.9).

$$X(+) = \Phi_k * X(-) \tag{3.8}$$

$$P(+) = \Phi_k * P(-) * \Phi_k^T + Q \tag{3.9}$$

The system model, F, is shown in Equation (3.11) and is used in the calculation of the discrete state transition matrix, Φ_k. The discrete state transition matrix, shown in Equations (3.8) and (3.9) is used to propagate the error states and the state covariance forward in time. The state transition matrix is approximated through the truncation of the

Taylor series expansion of $e^{F\Delta t}$ to the first order resulting in Equation (3.10) [8].

$$\Phi_k = I_{17x17} + F * \delta t \tag{3.10}$$

$$F = \begin{bmatrix} 0_{3x3} & I_{3x3} & 0_{3x3} & 0_{3x3} & 0_{3x3} & 0_{3x2} \\ G & -2\Omega_e & -F_e & C_b^e & 0_{3x3} & 0_{3x2} \\ 0_{3x3} & 0_{3x3} & -\Omega_e & 0_{3x3} & C_b^e & 0_{3x2} \\ 0_{3x3} & 0_{3x3} & 0_{3x3} & \frac{-1}{\tau_{acc}} * I_{3x3} & 0_{3x3} & 0_{3x2} \\ 0_{3x3} & 0_{3x3} & 0_{3x3} & 0_{3x3} & \frac{-1}{\tau_{gyr}} * I_{3x3} & 0_{3x2} \\ 0_{2x3} & 0_{2x3} & 0_{2x3} & 0_{2x3} & 0_{2x3} & f_{clk} \end{bmatrix} \tag{3.11}$$

Equations (3.12) and (3.13) show the computation for the gravitational terms relating ECEF velocity to the ECEF position.

$$G = -\frac{2 * g_b^e(P_e)}{r_{eS}^e * P_e * \sqrt{P_e^2}} \tag{3.12}$$

$$r_{eS}^e = \frac{R_0\sqrt{1 - (e_{wgs} * sin(L))^2}}{\sqrt{cos(L)^2 + \left(1 - e_{wgs}^2\right) * sin(L)^2}} \tag{3.13}$$

The terms F_e and Ω_3 are the skew-symmetric matrices of the specific force in the global frame, f_e, and the rotation rate in the global frame, ω_e, respectively. These conversions are shown in Equations (3.14) and (3.15) respectively.

$$F_e = [Skew(f_e)] \tag{3.14}$$

$$\Omega_e = [Skew(\omega_e)] \tag{3.15}$$

The state covariance matrix, P, is also affected by the Gaussian noise corruption, or system noise covariance matrix, Q, which is calculated in Equation (3.16).

$$Q = B * E[vv^T] * B^T * \delta t \tag{3.16}$$

The Gaussian noise corruption is made up of the expected noise terms, $E[vv^T]$, and the input mapping matrix, B, shown in Equations (3.17) and (3.18) respectively.

$$E[vv^T] = \begin{bmatrix} \sigma^2_{v_a} I_{3x3} & 0_{3x3} & 0_{3x3} & 0_{3x3} \\ 0_{3x3} & \sigma^2_{v_g} I_{3x3} & 0_{3x3} & 0_{3x3} \\ 0_{3x3} & 0_{3x3} & \sigma^2_{v_{b_a}} I_{3x3} & 0_{3x3} \\ 0_{3x3} & 0_{3x3} & 0_{3x3} & \sigma^2_{v_{b_g}} I_{3x3} \end{bmatrix} \tag{3.17}$$

$$B = \begin{bmatrix} 0_{3x3} & 0_{3x3} & 0_{3x8} \\ C_b^e & 0_{3x3} & 0_{3x8} \\ 0_{3x3} & C_b^e & 0_{3x8} \\ 0_{8x3} & 0_{8x3} & I_{8x8} \end{bmatrix} \tag{3.18}$$

The variances used for this research are established in [5] and can be seen in Table (3.1).

Table 3.1: Variances Used in Process Noise Matrix (From: [5])

$\sigma^2_{v_a}$	1.0e-2
$\sigma^2_{v_g}$	2.4e-7
$\sigma^2_{v_{b_a}}$	1.2e-2
$\sigma^2_{v_{b_g}}$	8.7e-4

3.2.2 GPS/INS Measurement Update

The Inertial Navigation Solution (INS) calculated in the prediction step, or time update, of the extended Kalman filter must be corrected periodically by a measurement update to correct drift of the dead reckoning solution. The measurement update is calculated by comparing calculated ranges and range rates between the receiver and each satellite vehicle to the pseudo-range and pseudo-range rate parameters given by the GPS receiver in a closely coupled architecture. This procedure is known as the measurement innovation and is shown in Equation (3.19),

$$z = \begin{bmatrix} \delta z_\rho \\ \vdots \\ \delta z_{\dot{\rho}} \\ \vdots \end{bmatrix} = \begin{bmatrix} \rho - \hat{\rho} \\ \vdots \\ \dot{\rho} - \hat{\dot{\rho}} \\ \vdots \end{bmatrix} \tag{3.19}$$

where ρ represents the measured and corrected pseudo-range given by the receiver and $\hat{\rho}$ represents the pseudo-range calculated from the prediction step of the navigation filter and the predicted satellite vehicle positions and velocities, as shown in Equation (3.20). The predicted pseudo-range must also account for the estimated GPS clock offset error, b_{cerr}.

$$\hat{\rho}_s = \sqrt{(P_e - P_{S_e})^T (P_e - P_{S_e})} + b_{cerr} \tag{3.20}$$

The measurement vector equation, demonstrated by Equation (3.19), is made up of measurement innovations, δz_ρ, which are calculated based on the measured pseudo-range rate, $\dot{\rho}$, and the predicted pseudo-range rate, $\hat{\dot{\rho}}$. The predicted pseudo-range rate is calculated based on the ECEF position and velocity, P_e and V_e, of the receiver and the ECEF position and velocity of each Satellite Vehicle, P_{S_e} and V_{S_e}, as shown in Equation (3.21). The predicted pseudo-range rate must also account for the estimated GPS clock drift error, b_{cdft}.

$$\hat{\dot{\rho}}_s = \frac{(P_e - P_{S_e})^T (V_e - V_{S_e})}{\sqrt{(P_e - P_{S_e})^T (P_e - P_{S_e})}} + b_{cdft} \tag{3.21}$$

The measured pseudo-range rate is a product of the receiver reported doppler frequency, f_d, the speed of light, c, and the wavelength of the L1 carrier frequency, $\lambda_{L1} = 15475.42MHz$, as shown in Equation (3.22).

$$\dot{\rho}_s = -\frac{c}{\lambda_{L1}} f_d \tag{3.22}$$

Both the predicted pseudo-range and predicted pseudo-range rate are compensated by clock error terms in Equations (3.20) and (3.21) respectfully.

The rest of the measurement update can be performed once the measurement innovations have been calculated. The prediction equations are nonlinear functions of the states as represented by Equations (3.20) and (3.21). Therefore, a linearized measurement model, H, is necessary to in order to calculate the Kalman gain, K. The linearized measurement model is provided in Equation (3.23),

$$H = \left[\begin{array}{ccccccc} u_1^e & 0_{1,3} & 0_{1,3} & 0_{1,3} & 0_{1,3} & 1 & 0 \\ u_2^e & 0_{1,3} & 0_{1,3} & 0_{1,3} & 0_{1,3} & 1 & 0 \\ \vdots & \vdots & \vdots & \vdots & \vdots & \vdots & \vdots \\ u_m^e & 0_{1,3} & 0_{1,3} & 0_{1,3} & 0_{1,3} & 1 & 0 \\ \hdashline 0_{1,3} & u_1^e & 0_{1,3} & 0_{1,3} & 0_{1,3} & 0 & 1 \\ 0_{1,3} & u_2^e & 0_{1,3} & 0_{1,3} & 0_{1,3} & 0 & 1 \\ \vdots & \vdots & \vdots & \vdots & \vdots & \vdots & \vdots \\ 0_{1,3} & u_m^e & 0_{1,3} & 0_{1,3} & 0_{1,3} & 0 & 1 \end{array}\right] \tag{3.23}$$

and the ECEF-frame line-of-sight unit vectors, u_S^e, are calculated as seen in Equation (3.24).

$$u_S^e = \frac{P_{S_e} - P_e}{||P_{S_e} - P_e||} \tag{3.24}$$

Prior to performing the measurement update calculation, the measurement covariance matrix, R, must be calculated. The measurement variance for each measured pseudo-range and pseudo-range rate are factored in to the measurement covariance matrix, as seen in

Equation (3.25), assuming all measurement errors are uncorrelated.

$$R = \left[\begin{array}{cccccccc} \sigma^2_{\rho_1} & 0 & 0 & 0 & 0 & 0 & 0 & 0 \\ 0 & \sigma^2_{\rho_2} & 0 & 0 & 0 & 0 & 0 & 0 \\ \vdots & \vdots & \ddots & \vdots & \vdots & \vdots & \vdots & \vdots \\ 0 & 0 & 0 & \sigma^2_{\rho_m} & 0 & 0 & 0 & 0 \\ \hdashline 0 & 0 & 0 & 0 & \sigma^2_{\dot{\rho}_1} & 0 & 0 & 0 \\ 0 & 0 & 0 & 0 & 0 & \sigma^2_{\dot{\rho}_2} & 0 & 0 \\ \vdots & \vdots & \vdots & \vdots & \vdots & \vdots & \ddots & \vdots \\ 0 & 0 & 0 & 0 & 0 & 0 & 0 & \sigma^2_{\dot{\rho}_m} \end{array}\right] \tag{3.25}$$

A Fault Detection and Exclusion (FDE) algorithm, to be discussed in Section 3.2.3, is also performed prior to the final measurement update calculations. The FDE requires that each variance calculation is based on the carrier to noise ratio, c/n_0, of the received signal from each satellite vehicle (SV) and receiver characteristics. The pseudo-range covariance measurement is a function of the variance in the Delay-Lock-Loop (DLL), as seen in Equations (3.26) and (3.27).

$$\sigma^2_\rho = \sigma^2_{\rho_{atm}} + \sigma^2_{DLL} \tag{3.26}$$

$$\sigma_{DLL} = \lambda_c \sqrt{\frac{4d^2 B_{np}}{c/n_0}\left(2\left(1-d\right) + \frac{4d}{Tc/n_0}\right)} \tag{3.27}$$

The pseudo-range rate covariance calculation is a function of the variance in the Frequency-Lock-Loop, as seen in Equations (3.28) and (3.29).

$$\sigma^2_{\dot{\rho}} = \sigma^2_{FLL} + \frac{f^2_E}{9} \tag{3.28}$$

$$\sigma_{FLL} = \frac{\lambda}{2\pi T}\sqrt{\frac{4B_{np}}{c/n_0}\left(1 + \frac{1}{Tc/n_0}\right)} \tag{3.29}$$

The calculation of the measurement variance functions are based on work presented in [6] and [28]. The variables shown in Equations (3.27) and (3.29) are presented with used values and descriptions in Table 3.2.

Table 3.2: Pseudo-Range Variance Calculation Parameters (From: [6] and [7])

Parameter	Description	Value
$\sigma^2_{\rho_{atm}}$	Variance due to atmospheric code delay	5.22 (m)
λ_c	Code chip width	293.05 (m)
d	Correlator spacing	0.5 (chips)
B_{np}	Code loop noise bandwidth	2 (Hz)
T	Prediction integration time	2 (ms)

The Kalman gain can now be calculated as a function of the measurement model, H, the error state covariance matrix, P, and the measurement covariance matrix, R, as shown in Equation (3.30).

$$K = \frac{P^- H^T}{H P^- H^T + R} \tag{3.30}$$

The Kalman Gain is then used to update the state vector, X, in (3.31)

$$X^+ = X^- + Kz \tag{3.31}$$

and the error state covariance matrix, P, in (3.32).

$$P^+ = (I - KH)\, P^- \tag{3.32}$$

3.2.3 Fault Detection and Exclusion

A significant advantage of running the closely coupled architecture of the extended Kalman filter is the ability to perform a Fault Detection and Exclusion (FDE) algorithm.

Some of the GPS errors previously listed in Section 2.1.1, such as multipath, can sporadically affect the pseudo-range and pseudo-range rate measurements from each satellite vehicle. Fault detection and exclusion plays an indispensable role in high foliage or dense urban environments that contain many objects in which a GPS signal can be blocked by or reflected off of.

The fault detection and exclusion algorithm used in this thesis is a technique described as innovation filtering [4]. Innovation filtering is performed by comparing the normalized innovations, y, to a threshold in order to verify that the new measurements are consistent with previous information and predicted states. A threshold of $y_{max} = 3$ is used for the algorithms presented in this thesis, which allows 99.73% [4] of the genuine measurements to be passed through the innovation filter. The normalized innovations are calculated in Equation (3.33),

$$y = \frac{\delta z}{\sqrt{C_{\delta z}}} < 3 \tag{3.33}$$

where $C_{\delta z}$ is the covariance of the innovations sometimes referred to as the normalizing value. Note that in Equation (3.34)

$$C_{\delta z} = HP^{-}H^{T} + R \tag{3.34}$$

the covariance of the innovations calculation is the same as the denominator of the Kalman gain equation shown in Equation (3.30).

The fault detection and exclusion algorithm is performed prior to the calculation of the Kalman gain, the state vector update, and the error state covariance matrix update. The exclusion portion of the FDE algorithm must take place before finalizing the measurement update of the Kalman filter due to the fact that the linearized measurement model, H, and the measurement covariance matrix, R, must be updated to account for the excluded measurements. Once all parameters found in Equations (3.30 - 3.32) have been updated to account for any excluded measurements, the final update may be executed.

An example of the role played by the FDE algorithm can be seen in Figure 3.5.

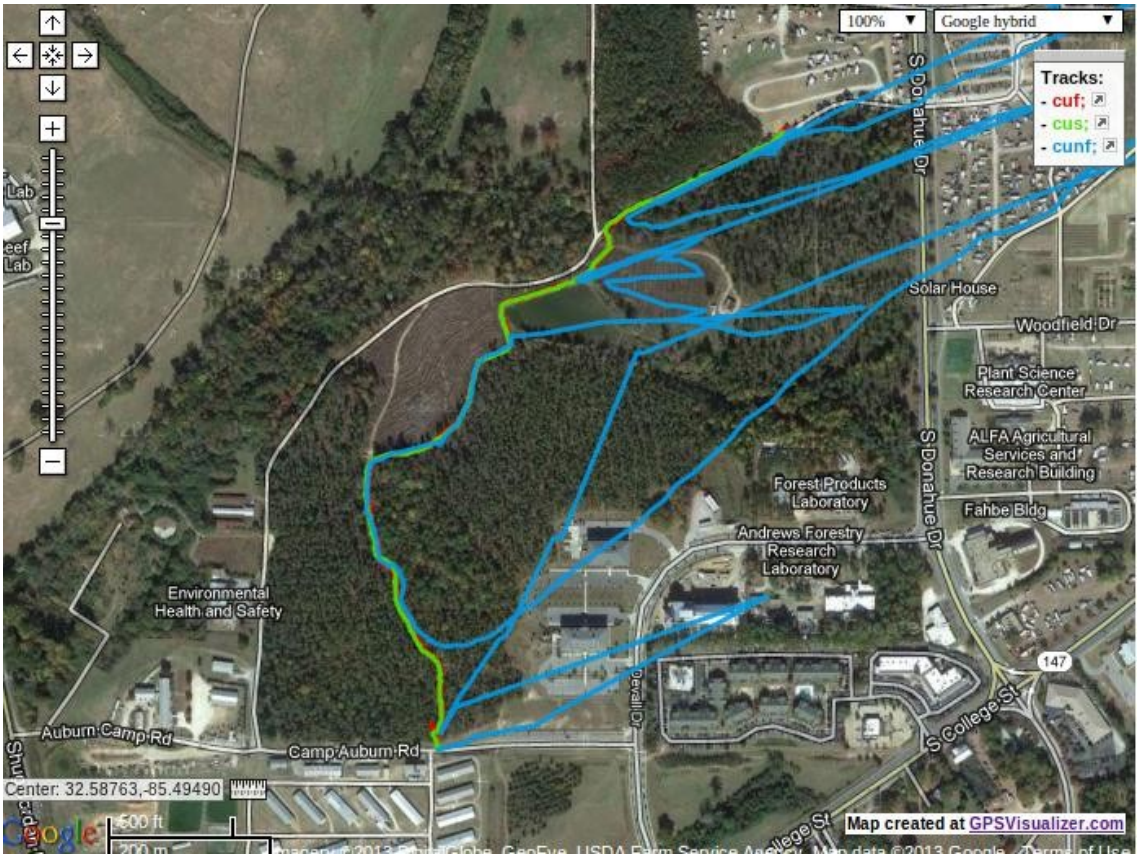

Figure 3.5: Closely coupled GPS/INS (in red) shown with uBlox position solution (in green) and GPS/INS without fault detection and exclusion (in blue)

3.3 Experimentation and Results

One objective of the research presented in this thesis is to compare sensor sets and algorithms against each other through the use of real world experimental data. This section will present the data collection system and environment utilized for all algorithms as well as highlight the performance of the GPS/INS algorithm. The comparative analysis of the various developed GPS/INS/VDM algorithms to the GPS/INS algorithm outlined in this chapter will be demonstrated in Chapter 4.

3.3.1 Experimental Data Collection Setup

The primary data collection platform for this research is the 2003 Infiniti G35 sedan shown in Figure 3.6. This vehicle is the ideal platform given the nature of the current research due to the high dynamic performance capabilities of the car.

Figure 3.6: 2003 G35 Data Collection Platform

The data collection platform is outfitted with a single board, single frequency Novatel GPS receiver and a Crossbow 400 MEMs grade IMU shown in Figure 3.1 and Figure 3.7 respectively. The G35 is also outfitted with a Septentrio multi-antenna GPS receiver, shown in Figure 3.8, for position, velocity, and attitude truth reference. The truth GPS receiver is given Real-Time Kinematic (RTK) updates in order to establish centimeter level position accuracy.

Figure 3.7: Crossbow 400 MEMs grade IMU

Figure 3.8: Septentrio Multi-Antenna GPS Receiver

3.3.2 Data Collection Environments

The research presented in this chapter uses real world experimental data in order to give the most accurate comparison of the navigation algorithms. Three different data collection environments are utilized in order to provide the best overall performance analysis for multiple scenarios. A short GPS outage scenario is demonstrated by the first data collection environment shown in Figure 3.9 and Figure 3.10. The data collection route passing under multiple interstate over passes is used to demonstrate the performance of a fused navigation system during the times of GPS outage that would occur during every day driving.

Figure 3.9: Date Collection Route 1: Short GPS Outage

Figure 3.10: Date Collection Route 1: Short GPS Outage (Street View)

The second data collection environment utilizes the 1.8 mile track at Auburn University's National Center for Asphalt Technology (NCAT) as is shown in Figure 3.11. The NCAT test track allows data collection of high dynamic maneuvers due to the lack of restrictions brought on by sharing a road with other vehicles and the the general laws of public roadways. The second data set collected to demonstrate the performance of the GPS/INS navigation algorithm is a double lane change maneuver performed on a straight section of track shown in Figure 3.12.

Figure 3.11: Aerial View of NCAT

Figure 3.12: Ground View of NCAT Straight Section Used for Double Lane Change Maneuver

A diagram describing the double lane change maneuver is seen in Figure 3.13. The high speed double lane change maneuver is used in this thesis to demonstrate the performance of the GPS/INS navigation algorithm during high dynamic driving situations. The average speed during the double lane change maneuver is 24 meters/second or approximately 55 miles/hour.

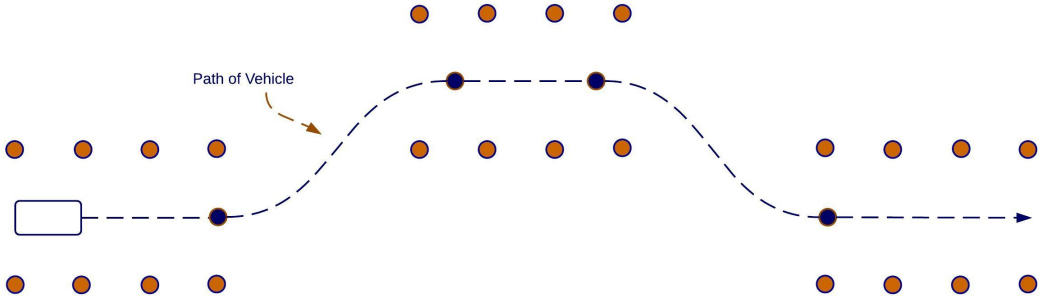

Figure 3.13: Double Lane Change Maneuver Diagram

The final data collection environment presented in this chapter is used to demonstrate the performance of the GPS/INS navigation algorithm during extended periods in the absence of GPS signals. An approximation of the route is shown in Figure 3.14 and a street view photograph of the parking garage and stadium is shown in Figure 3.15.

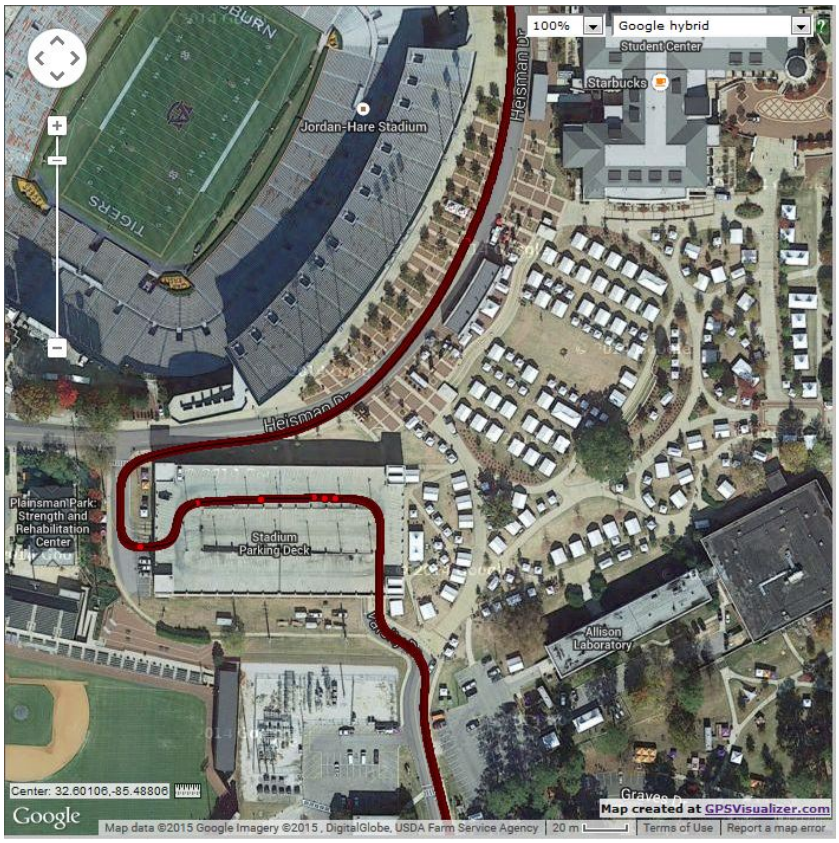

Figure 3.14: Date Collection Route 3: Extended GPS Outage

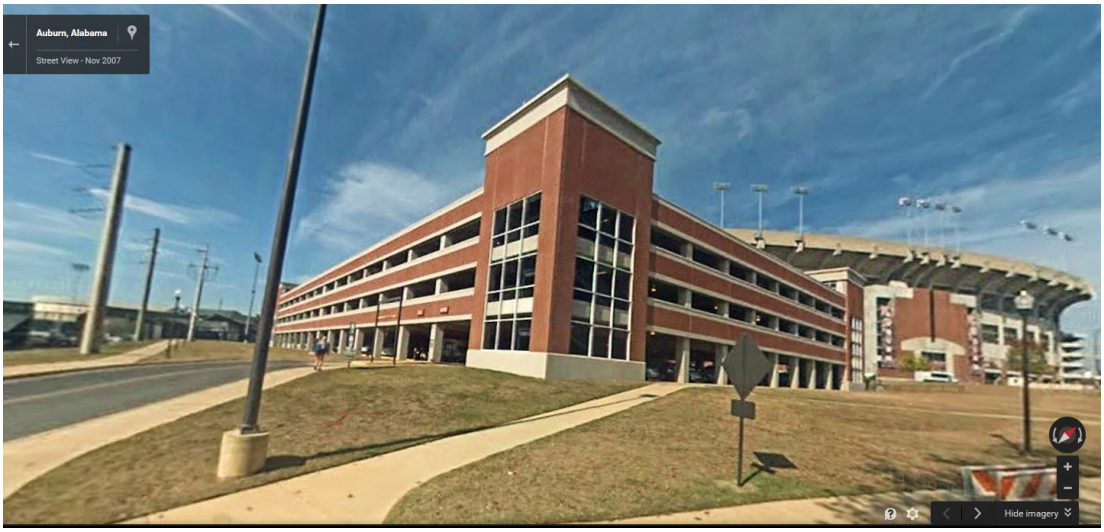

Figure 3.15: Date Collection Route 3: Extended GPS Outage (Street View)

The three data collection environments present an accurate overview of the GPS/INS navigation algorithm's performance during daily driving scenarios that are difficult to maintain an accurate navigation fix.

3.3.3 GPS/INS Navigation Results

The data collected in the scenarios described by Section 3.3.2 are used for post-process analysis of the performance of the GPS/INS navigation algorithm described in Section 3.2. A Real-Time Kinematic (RTK) GPS system is used as the benchmark truth measurement for position, velocity, and attitude (PVA) of the vehicle whenever a GPS solution is available. A full analysis of the GPS/INS navigation algorithm for the previously described environments is presented in the following subsections:

Interstate Overpass

The primary objective of driving the data collection vehicle under an interstate overpass is demonstrating the performance of the GPS/INS navigation filter during periods of short GPS signal unavailability. Figure 3.16 demonstrates the distance traveled in the eastward

direction vs time to show that the truth reference system experienced multiple short GPS outages during the data collection. The longest GPS outage was approximately 7 seconds as seen in Figure 3.16 and Figure 3.17.

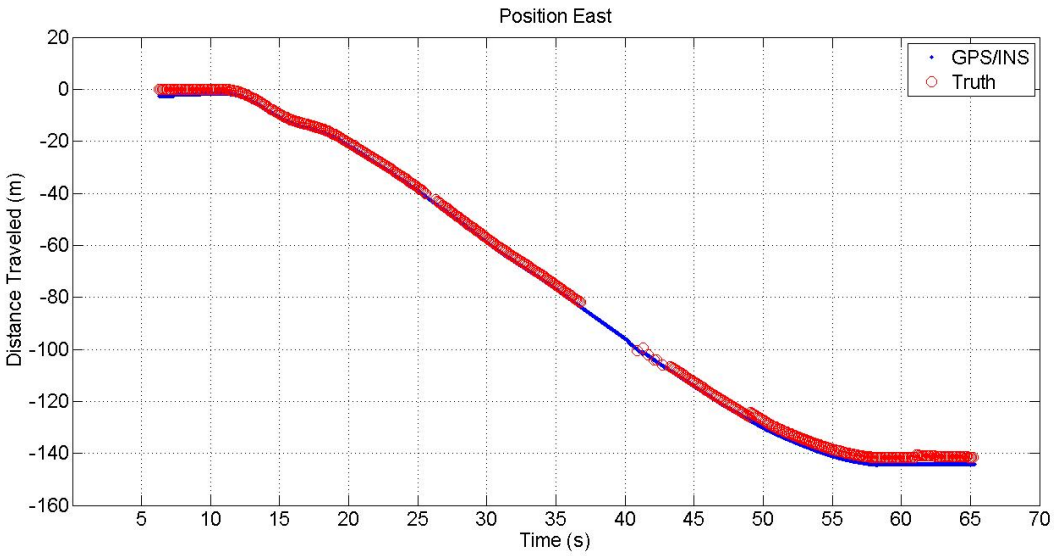

Figure 3.16: Eastward Position vs. Time

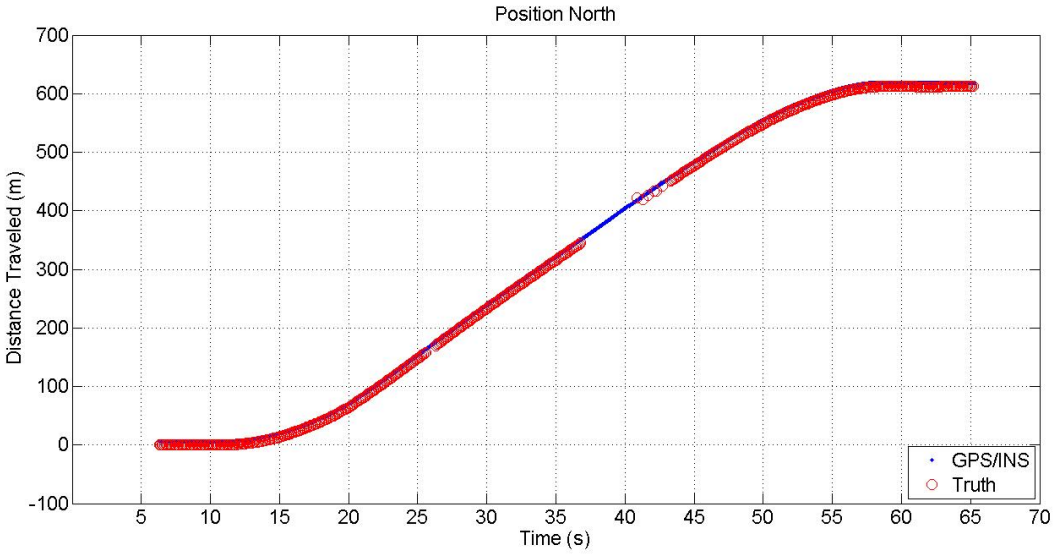

Figure 3.17: Northward Position vs. Time

A closer examination of the navigation solutions during GPS outage is demonstrated by Figure 3.18. Note that the GPS/INS solution tracks a the correct position assuming that the vehicles velocity vector was relatively constant during the time of GPS outage.

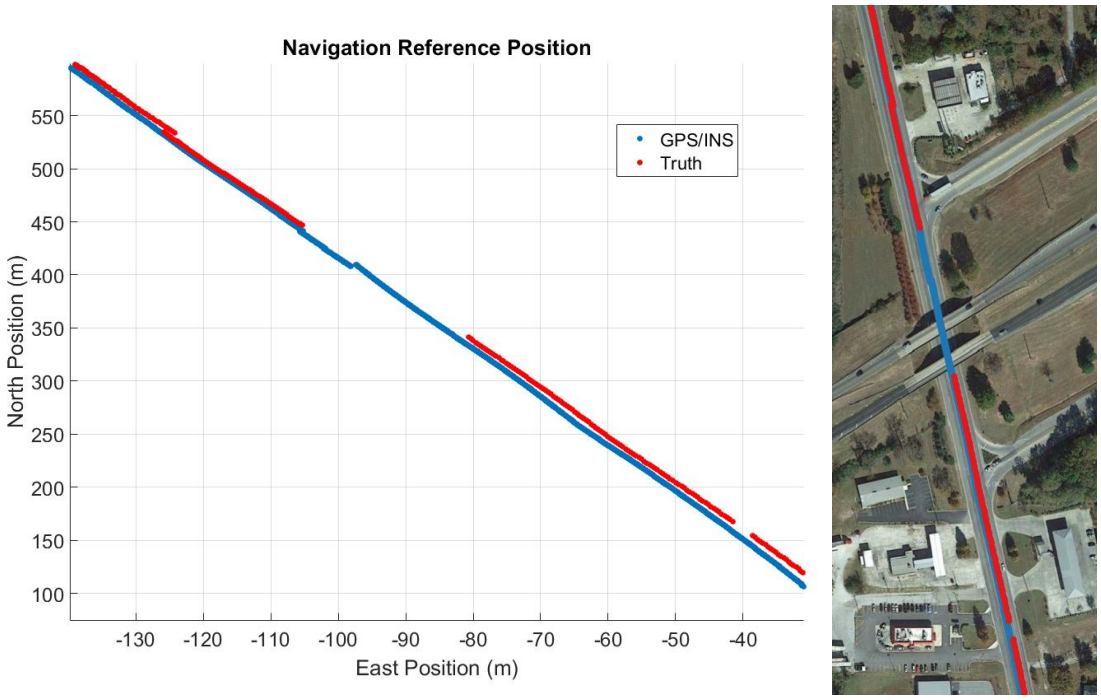

Figure 3.18: Navigation Solutions During GPS Outage

Note the sub meter jump in the position solution shown in Figure 3.18. The jump can be assumed to be the result of using information from two satellites, as seen in Figure 3.19. Figure 3.19 shows the number of available satellite signals at each epoch of the OEMstar GPS receiver overlaid with the number of faults detected by the FDE algorithm during each measurement update. The OEMstar receiver claims at least three SV's in view at all times during data collection. However, these signals raise faults as the signals may contain multipath during periods with no clear view of the sky. Towards the end of the GPS outage, two satellites pass through the FDE algorithm while the other two signals are declared faults. The likely case is that one of the passed signals was affected by multipath errors that were small enough to pass the FDE threshold. Therefore, the signal led to the minimal jump of the GPS/INS navigation solution from the expected trajectory.

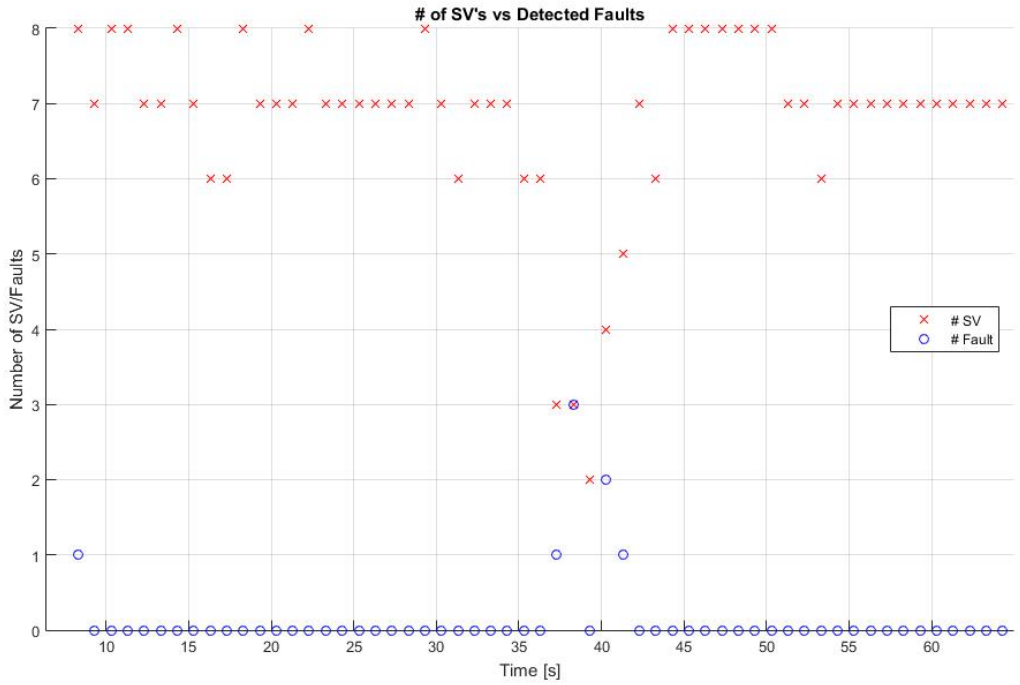

Figure 3.19: Satellite Signals and Detected Faults

Double Lane Change

The primary objective of performing a high speed double lane change maneuver is to demonstrate the performance of the GPS/INS navigation algorithm during high dynamic situations. High dynamic situations could be encountered at any moment during daily driving in order to avoid an obstacle or prevent a collision. High dynamic maneuvers can cause problems when using low-cost GPS receivers due to the low bandwidth associated with such sensors as demonstrated by Figure (3.20) and Figure (3.23). The fusion of GPS measurements with an INS allows for a high bandwidth PVA estimate between updates.

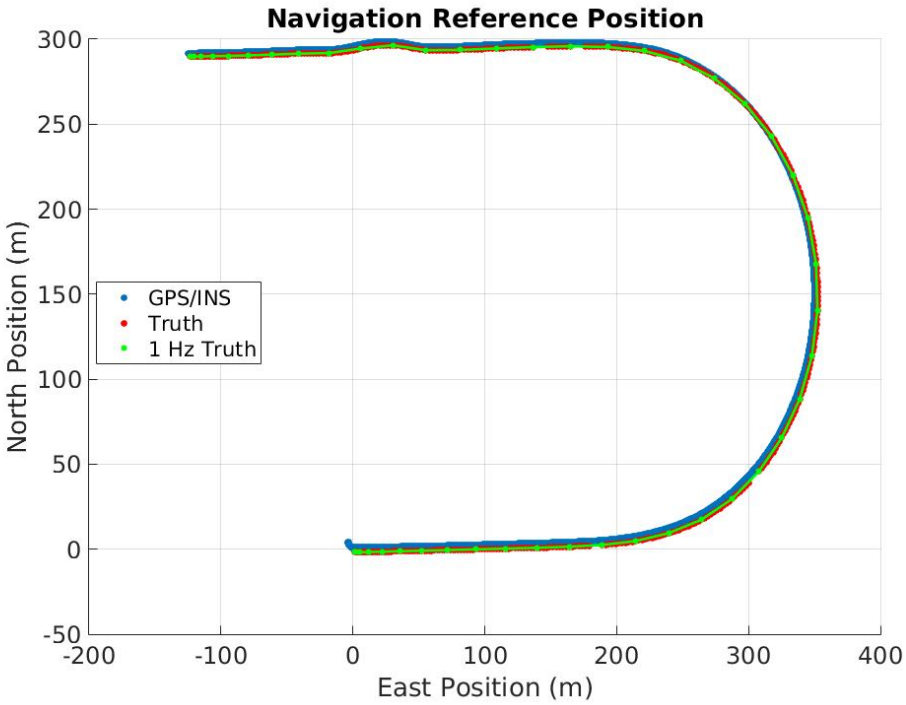

Figure 3.20: Double Lane Change Following High Speed Turn

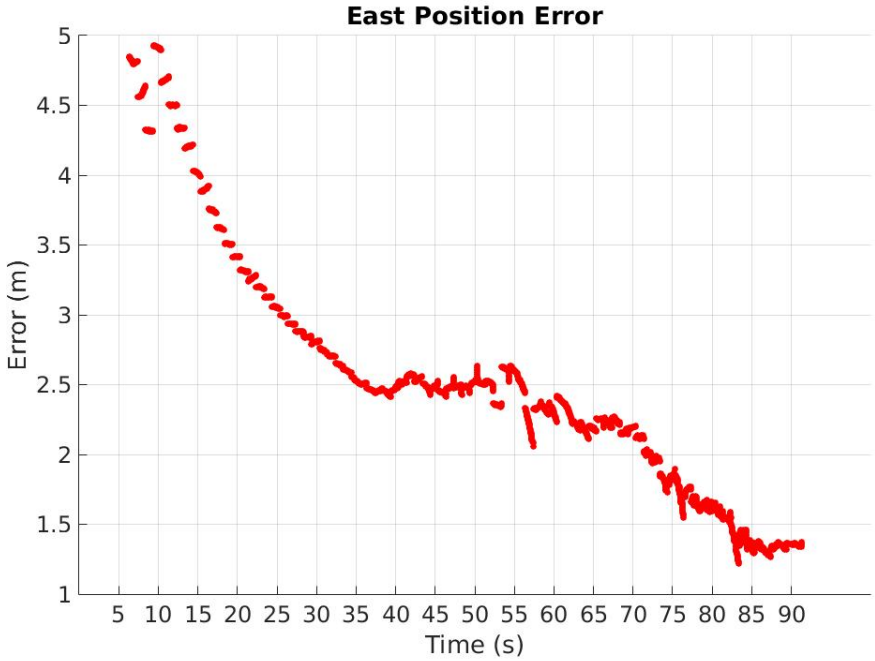

Figure 3.21: East Position Deviation from Truth Position Solution

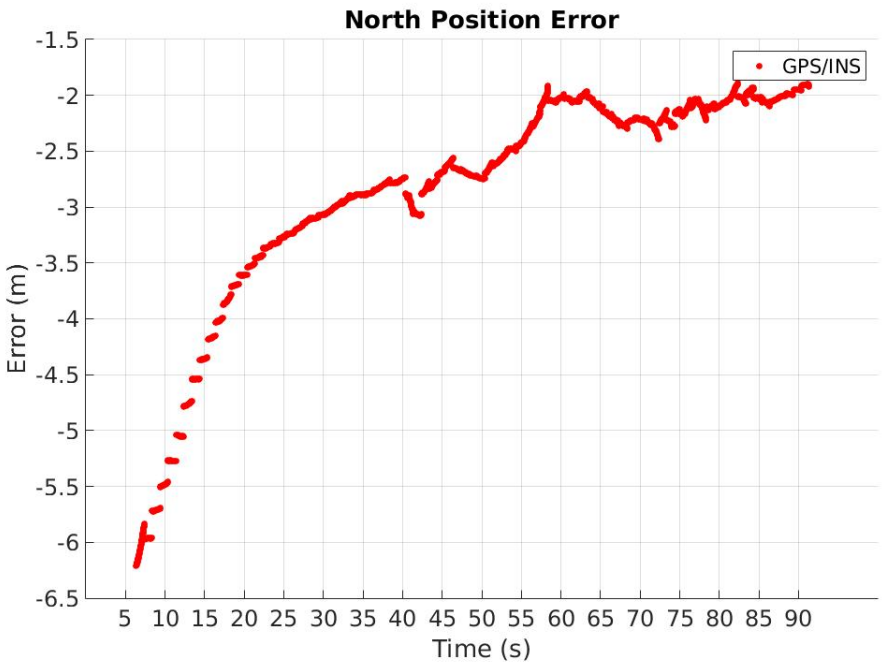

Figure 3.22: North Position Deviation from Truth Position Solution

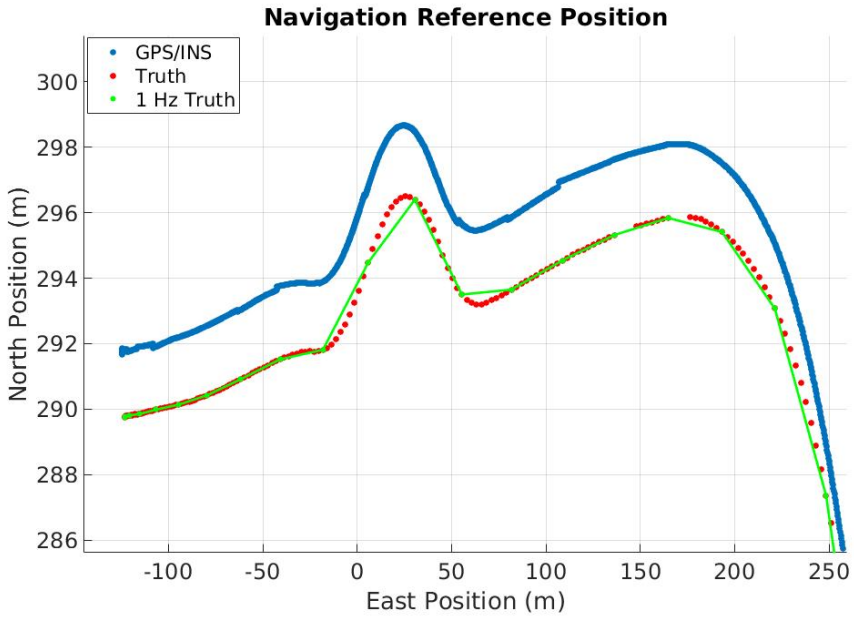

Figure 3.23: Double Lane Change Results

Note the offset between the GPS/INS navigation solution and the the truth RTK GPS solution in Figure 3.21, 3.22, and 3.23. This offset represents the absolute position bias that

cannot be overcome when using the low-cost GPS receiver. Also note the linear interpolation between the $1Hz$ simulated GPS position solution points does not follow the actual motion of the vehicle. The linear interpolation accounts for all available data points rather than only focusing on previous points as would be available to a real-time navigation solution. Therefore, fusion with the INS and/or other higher bandwidth sensors is essential for robust precision ground vehicle navigation in real-world scenarios when using a low-cost GPS receiver. Further results and analysis plots can be found in Appendix B.

Figure 3.24: Double Lane Change Results on Map

Parking Garage

The final environment to demonstrate the performance of the navigation solution focuses on extended GPS outage. An extended period of time without corrections from a GNSS receiver forces a dead reckoning navigation solution relying solely on a low-cost INS. The low-cost INS quickly drifts from the actual route driven and error increases exponentially as time increases. The magnitude of the standalone INS errors are emphasized due to the low dynamics of the vehicle during the extended period of no corrections.

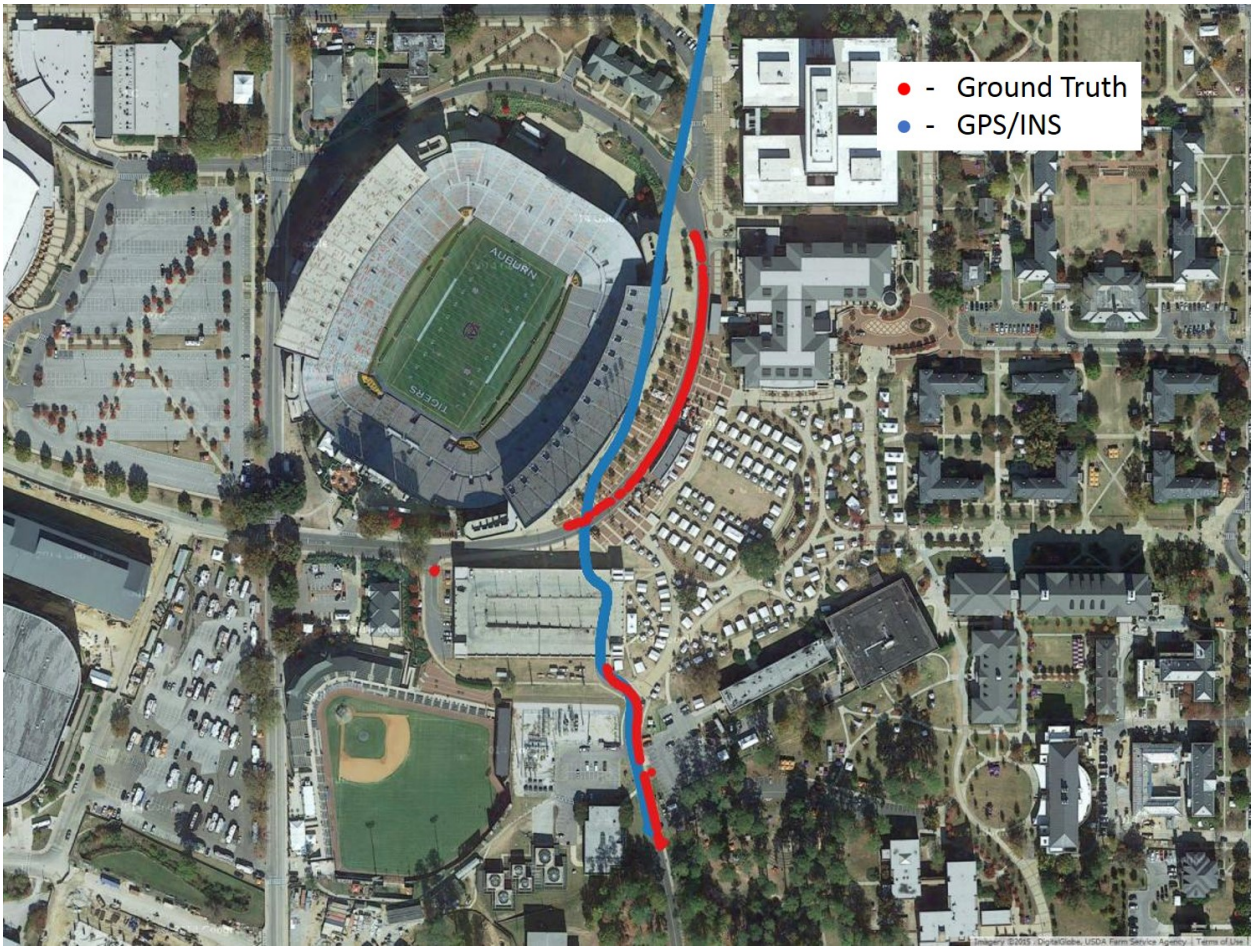

Figure 3.25: GPS/INS Extended GPS Outage Results

The performance of the GPS/INS navigation algorithm during data collection route 3 as visually compared to GPS Ground Truth is demonstrated by Figure 3.25. Note that no solution accurately tracks the position of the vehicle through the parking garage with degraded and/or no SV coverage to the GPS receivers. However, the GPS/INS solution is able to maintain what can be assumed as an accurate trajectory for a few seconds of time. The GPS/INS position solution quickly drifts greatly in the presence of such extended GNSS signal outage.

3.4 Conclusions

In this chapter, the significant advantages of aiding a GNSS receiver with an inertial navigation solution are demonstrated in multiple methods. The GPS/INS solution significantly outperforms a low cost receiver in all scenarios discussed throughout Section 3.3. The drastic advantages of fusing GPS with INS are seen throughout the scenarios presented in this chapter. Even during the moments that the highly expensive truth GPS system fails due to lack of satellite line of sight, the GPS/INS system is able to maintain a trajectory that is assumed to be correct and aligns with the truth GPS position solution upon renewed line of sight availability. The GPS/INS system does, however, demonstrate significant weaknesses during extended GNSS satellite vehicle loss of communication. The errors present on the low cost inertial measurement unit utilized by the INS grow quickly without correction updates from the GPS raw measurements.

The GPS/INS system is significantly advantageous to a standalone GPS receiver even when using low cost sensors. However, a significantly better solution for similar cost is needed in order to reliably use a low-cost sensor-fused localization system for autonomous navigation of a vehicle. A possible solution for significantly improving the base low-cost GPS/INS algorithm is explored in the next chapter.

Chapter 4

GPS/INS/VDM

As stated in Chapter 3, global navigation satellite systems (GNSS) have many advantages when considering localization and navigation with respect to a global reference frame. The many limitations of standalone GNSS/GPS navigation have also been discussed previously in this work. The baseline solution for benchmark comparison for global localization can be stated as the GPS/INS solution. The benchmark system created for low-cost comparison is outlined in Chapter 3, which also describes the many limitations of the low-cost GPS/INS navigation solution. The objective of the research presented in this chapter is to first determine whether or not aiding the GPS/INS algorithm with the measurements from a standalone vehicle dynamic model (VDM) yields any advantages. Assuming advantages through aiding the GPS/INS system are present as seen in Section 4.1, then the secondary objective of determining the optimal method in which to design a GPS/INS/VDM localization and navigation algorithm is researched.

4.1 GPS/INS/VDM Original

In attempting to assist the benchmark GPS/INS system with the vehicle dynamic model and sensor set, the initial step is to determine the measurements given by the new system as well as the accuracy of those measurements. Given the simplified VDM as described in Section 2.3, the possible measurement outputs include lateral and longitudinal velocity of the vehicle along with the body pitch and yaw of the vehicle. Unfortunately the accuracy and/or reliability of such measurements at each time epoch is unobservable for the standalone VDM system. There is however a single case in which the measurements can be assumed to have nearly perfect accuracy which is when the vehicle is static. The static vehicle phenomenon

is better known as a zero velocity update and the algorithm specifics are detailed in Section 4.1.1. The VDM inclusion algorithm is detailed further in Section 4.1.2.

4.1.1 Zero Velocity Update

The most obvious information available from inclusion of the vehicle safety sensors to utilize in the sensor fusion algorithm is the knowledge of the times when the vehicle is absolutely static. This zero velocity update forces measurement biases from the other fusion sensors to stand out against the known truth measurements from the VDM. Although zero velocity updates provide information only concerning velocity rather than absolute position information, the Kalman filter model builds up information regarding the correlation between the velocity and position errors [4]. Checks must be in place to ensure that mis-detected zero velocity updates occur in the situation of 4 wheel lock-up and sliding.

4.1.2 Algorithm Development

The primary decision prior to real algorithm development for the inclusion of the VDM in the sensor fusion architecture is whether the measurements should be brought in as a propagation step/time update or in the correction step/measurement update. Initial considerations in determining the manner in which to utilize the measurements of each system include analyzing the all measurement values and correlations as well as the coordinate frame that the measurements are reported in. The GPS/INS system is standard and the goal is to build on and aid that benchmark system rather than altering the original system. Therefore, the GPS measurements are applied as a correction step and the INS measurements are brought in through the propagation step. The initial consideration is to bring the VDM measurements in as a propagation update given that it is a dead reckoning localization system rather than a globally accurate system. The IMU gives 3 dimensional rotation rates and 3 dimensional accelerations in the local inertial frame and the VDM system provides 2 dimensional velocities and a yaw rotation rate in its local frame. Given that accelerations

are directly integrated to provide a velocity measurement at each propagation step and that the local inertial frame aligns with the local VDM frame as seen in Figure 4.1, the IMU and VDM would essentially provide redundant measurements if both are utilized in the propagation update. Therefore, the VDM system is used as a measurement update rather than a time update.

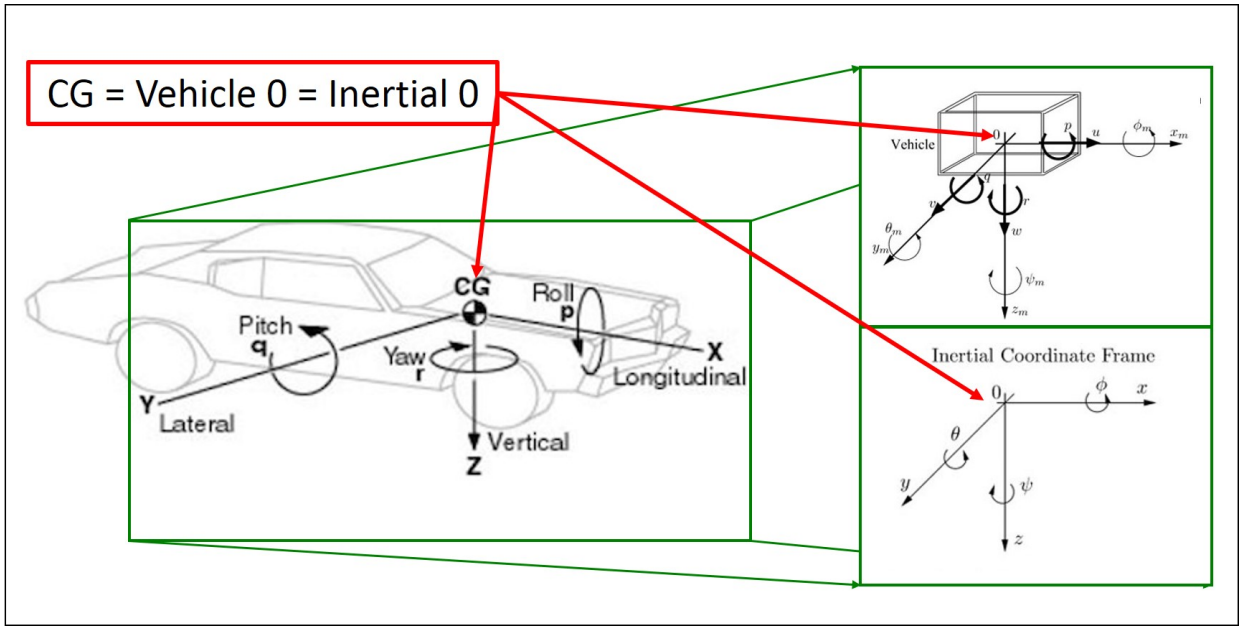

Figure 4.1: Visualization of Coordination Between Vehicle Frame and Inertial Frame

Utilization of the VDM as a measurement update also yields other significant advantages over using those measurements as a propagation update. The system description shown in Figure 4.2 describes the system architecture demonstrating that even during significant GNSS outages the localization solution is taking advantage of the full Kalman filter cycle. The measurement update allows the limitation of vast error growth present in a standalone INS utilizing low-cost accelerometers and gyros that a typical GPS/INS localization system would demonstrate during extended loss of signals from GPS satellites. This error growth in the localization solution is proven in Section 3.3.3 where the position solution error quickly grows without corrections.

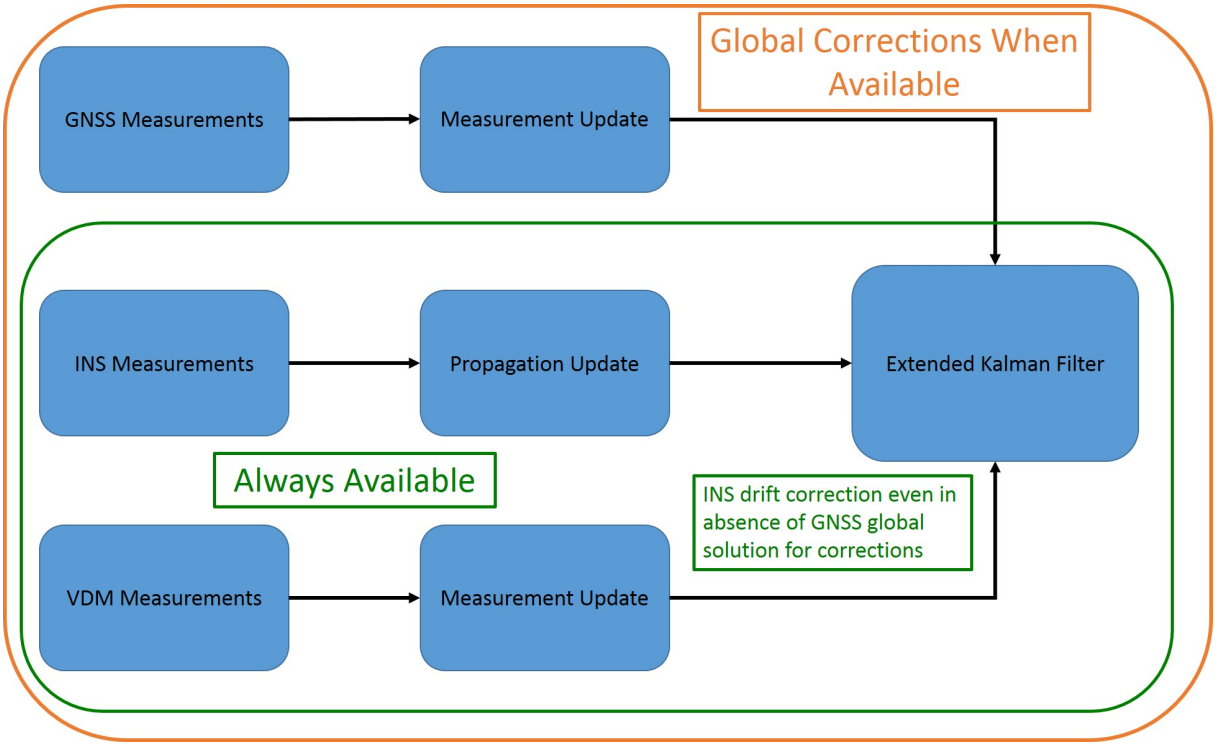

Figure 4.2: Full EKF Cycle During GNSS Absence

Since the purpose of this research is to determine the best method in which to include the VDM measurements in a sensor fused navigation algorithm, the error terms present in the VDM system, such as wheel radius and steer angle sensor bias, are estimated a priori rather than as states of the Kalman filter. Therefore, the system model remains the same as the benchmark GPS/INS system as seen in Equation (4.1).

$$X = [\ \delta P_e \quad \delta V_e \quad \delta \Psi \quad b_a \quad b_g \quad b_{cerr} \quad b_{cdft}\ ]^T \tag{4.1}$$

All EKF equations for the GPS measurement update and the INS propagation update remain identical to those described in Chapter 3 with the exception of the application of the zero velocity update as described in Section 4.1.1 above.

The vehicle dynamic model that is used to convert the raw wheel speed and steer angle measurements from the vehicle to the lateral and longitudinal velocity measurements are

found in Section 2.3. The application of the measurements in the GPS/INS/VDM algorithm initialize with the conversion of the the vehicle frame velocities to global frame velocities as seen in Equation (4.2).

$$V_e^{vdm} = C_b^e * \begin{bmatrix} V_x^{vdm} \\ V_y^{vdm} \\ V_z^{vdm} \end{bmatrix} \tag{4.2}$$

The global frame VDM velocities are then used to produce measurement innovations as seen in Equation (4.3) that will be utilized in the Kalman measurement update equations.

$$z = V_e - V_e^{vdm} \tag{4.3}$$

The measurement innovations are applied via the measurement model matrix, H, shown in Equation (4.4).

$$H = \begin{bmatrix} 0_{(3x3)} & I_{(3x3)} & 0_{(3x11)} \end{bmatrix} \tag{4.4}$$

The Kalman gain, calculated using Equation (4.5), is then used to update the state vector, X, in (4.6) and the error state covariance matrix, P, in (4.7).

$$K = \frac{P^- H^T}{H P^- H^T + R} \tag{4.5}$$

$$X^+ = X^- + Kz \tag{4.6}$$

$$P^+ = (I - KH)\, P^- \tag{4.7}$$

An important detail of note for the Kalman measurement update with measurements from the vehicle dynamic model is the determination of the measurement covariance matrix (R). The measurement covariance matrix for the GPS measurement update is calculated utilizing information given from the receiver regarding the signal strength of each incoming measurement. The vehicle dynamic model is incapable of providing information regarding

the quality of the reported measurements. Therefore, a constant measurement covariance matrix, seen in Equation (4.8), is used for all VDM measurement updates.

$$R^{vdm} = \begin{bmatrix} 1 & 0 & 0 \\ 0 & 1 & 0 \\ 0 & 0 & 1 \end{bmatrix} \tag{4.8}$$

The value of the measurement covariance matrix are set through recursive tuning based on experimental data.

The lack of knowledge of the confidence of the measurements produced by the vehicle dynamic model is major hindrance in achieving optimal performance of the Kalman filter algorithm. The Kalman filter algorithm is designed to increase weight on measurement corrections when the confidence is known to be high and decrease weight on measurement corrections when the confidence in the measurements is known to be low or unknown.

4.1.3 Experimentation and Results

The research presented in this chapter also uses real world experimental data, just as seen in Chapter 3, in order to give the most accurate comparison of the navigation algorithms. A detailed overview of the data collection environments utilized in the collection of the experimental data for post process analysis can be found in Section 3.3.2. Results from experimental data collected in environments not previously described in detail will also be presented through this chapter, but only as a redundant verification of results. The vehicle setup for experimental data collection is the same as described in Section 3.3.1 of this thesis.

Parking Garage

The parking garage data collection environment yields the greatest weakness with the GPS/INS localization system. The error growth in the INS only dead reckoning navigation solution quickly causes extreme drift in the absence of a measurement update. A primary

advantage to using the vehicle dynamic model as a measurement update rather than a time update is the availability of a full Kalman update process including the propagation step and the correction step, even in the absence of GNSS measurements. Due to the truth system's dependency upon GNSS availability, only a visual analysis of the performance of the GPS/INS/VDM with respect to the GPS/INS solutions is possible. The raw position measurement in the East North frame can be seen in Figure 4.3. An overlay of the position solution on a map is also presented in Figure 4.3 to give a better medium for visual analysis.

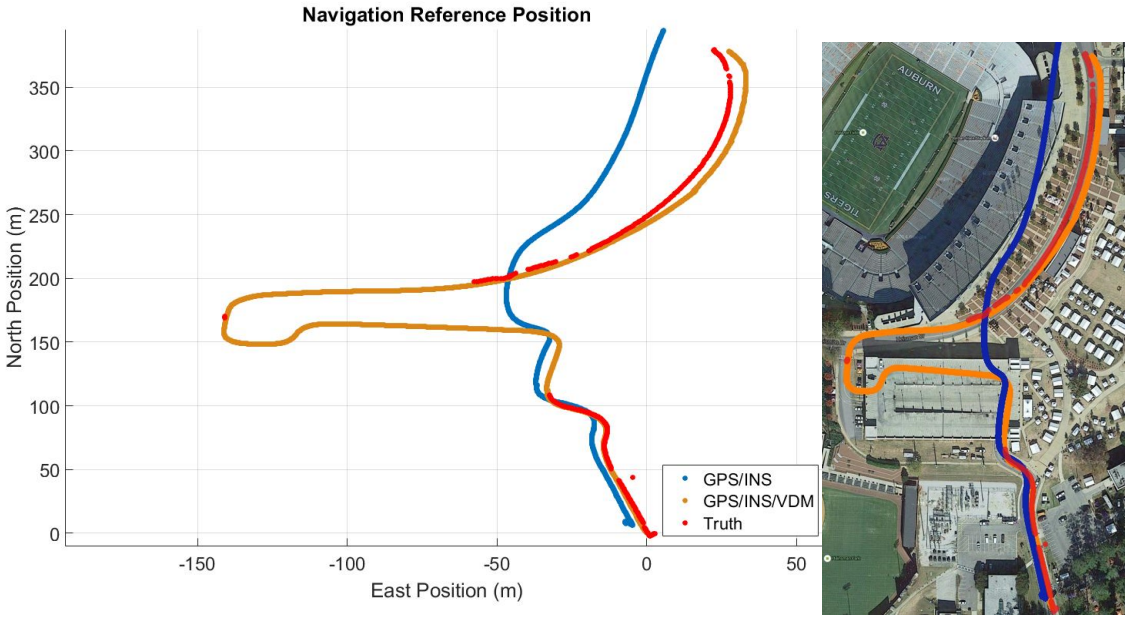

Figure 4.3: Localization Compare Results Extended GPS Outage

The performance of the GPS/INS/VDM can be seen to vastly exceed the performance of the GPS/INS system in Figure 4.3. Truth validation is not possible during the GNSS signal outage while utilizing the current truth data system, but the GPS/INS/VDM localization solution can be seen to approximately follow the assumed trajectory given the layout of the parking garage as seen in Figure 4.3. Note also the the GPS/INS/VDM solution is only slightly offset from the ground truth solution upon reacquisition where the GPS/INS solution is over 1 kilometer from the ground truth solution at the time of reacquisition.

Double Lane Change

The double lane change maneuver is now analyzed in order to demonstrate the performance of each filter algorithm under high vehicle dynamics. The maneuver itself is described in detail in Section 3.3.2 and the performance of the GPS/INS algorithm is discussed in Section 3.3.3. The GPS/INS algorithm maintained an accurate trajectory throughout this maneuver with a global position offset due to the lower quality of the GPS receiver utilized in this research. This maneuver is important to consider in regards to an autonomous vehicle's localization solution performance since the double lane change accurately portrays the trajectory of sudden obstacle avoidance. After proving in Section 4.1.3 that the GPS/INS/VDM algorithm demonstrates drastically improved performance in a specific navigation scenario, it is important to verify performance of the GPS/INS/VDM algorithm for alternate scenarios that may be experienced by an autonomous vehicle in a real world situation. A visual representation of the two navigation algorithms vs truth is given for the double lane change maneuver in Figure 4.4. Note that the visual inspection yields that the GPS/INS/VDM solution is drifting away from truth during and after the performance of the double lane change maneuver. The position solution for the entire data collection for the GPS/INS algorithm, the GPS/INS/VDM algorithm, and the ground truth is presented in Figure 4.5. As mentioned in Section 3.3.2, the double lane change maneuver is performed at approximately 55 mph following a 180° turn with an 8° bank at an even greater velocity.

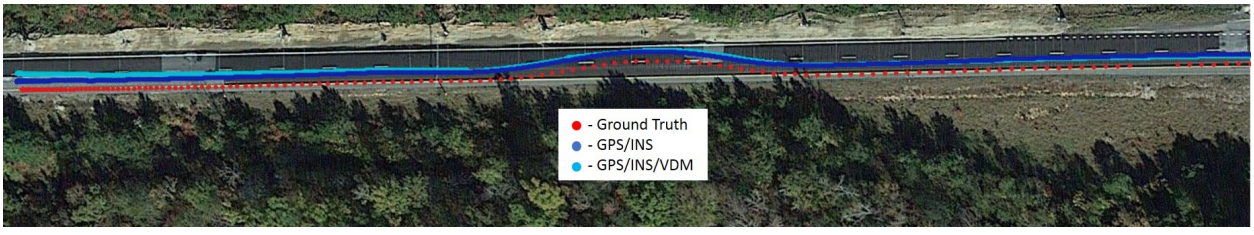

Figure 4.4: Double Lane Change Following High Speed Turn

Figure 4.5: Double Lane Change Following High Speed Turn Full Route

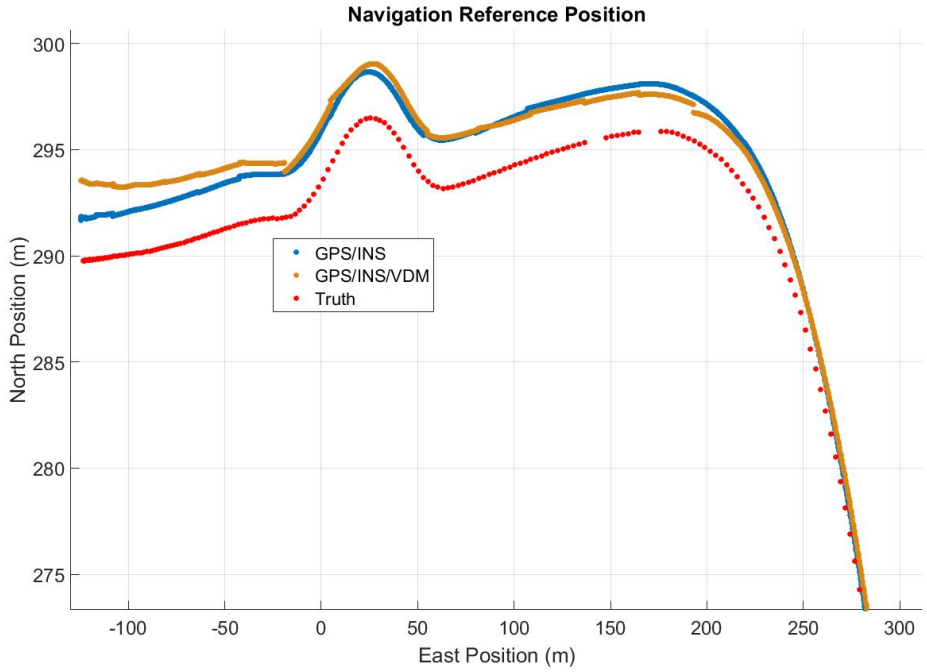

Figure 4.6: Double Lane Change East North Position Visualization

A plot of the east north position solution overlaid on a map in Figure 4.4 is displayed in Figure 4.6. The northward drift of the GPS/INS/VDM position solution is more apparent in this visualization. This drift is due to the simplified linear bicycle vehicle dynamic model's inability to fully capture dynamics when the vehicle experiences wheel slip due to high lateral dynamics. Further error analysis plots can be seen in Figure 4.7 through Figure 4.9. Note the sawtoothing in the vehicle frame lateral velocity error as the vehicle model drifts and then receives corrections from the GPS measurements. This is assumed to be caused by the errors present in the VDM velocity measurements during the high dynamics.

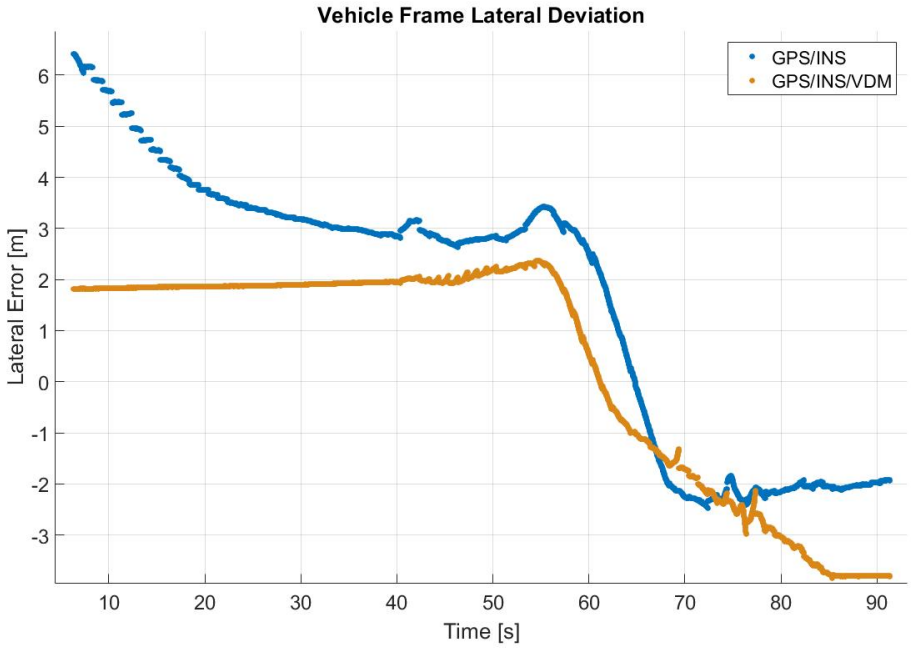

Figure 4.7: Double Lane Change Vehicle Frame Lateral Position Deviation from Ground Truth

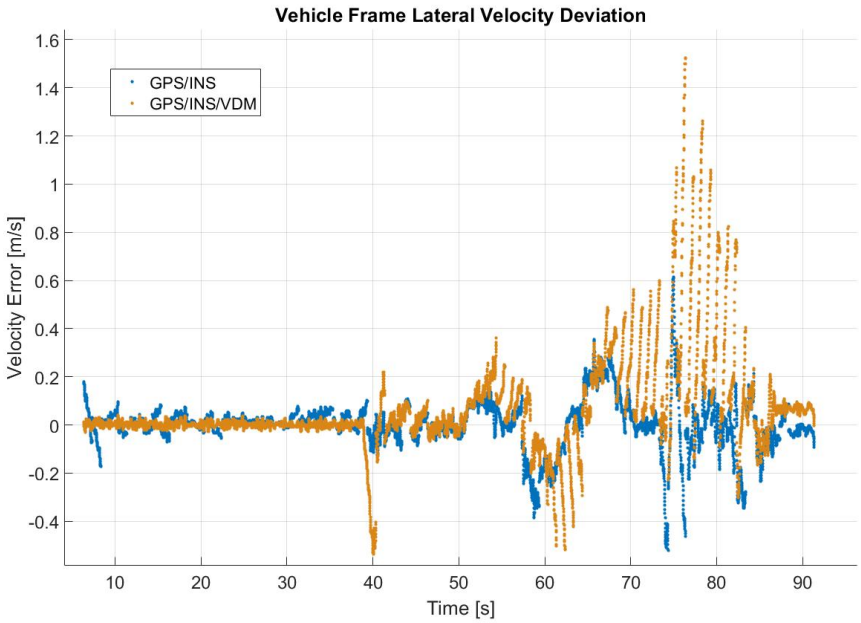

Figure 4.8: Double Lane Change Vehicle Frame Lateral Velocity Deviation from Ground Truth

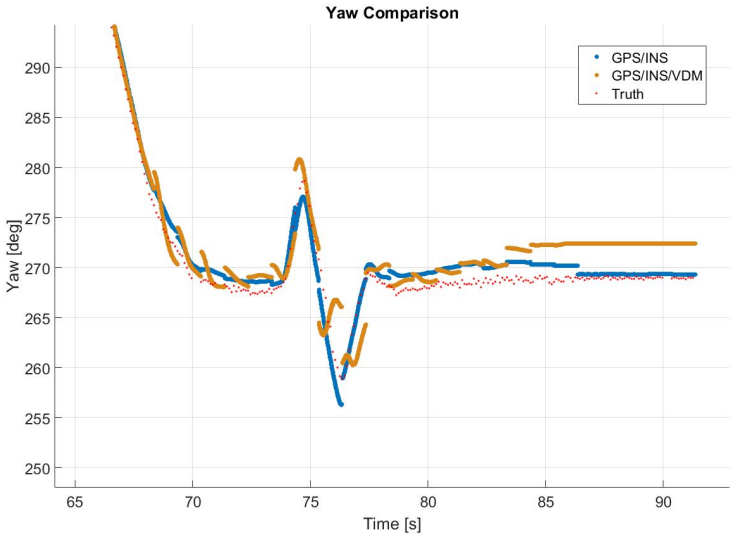

Figure 4.9: Double Lane Change Vehicle Yaw Visualization

Further error analysis plots of the entire double lane change maneuver can be seen in Appendix B.

High Speed NCAT Track

In order to analyze performance of the GPS/INS/VDM algorithm under higher dynamics that are not at the extreme of the double lane change maneuver, data along the same route at the NCAT track without finishing with the double lane change maneuver was utilized. A detailed view of the East North Position results can be seen below in Figure 4.10.

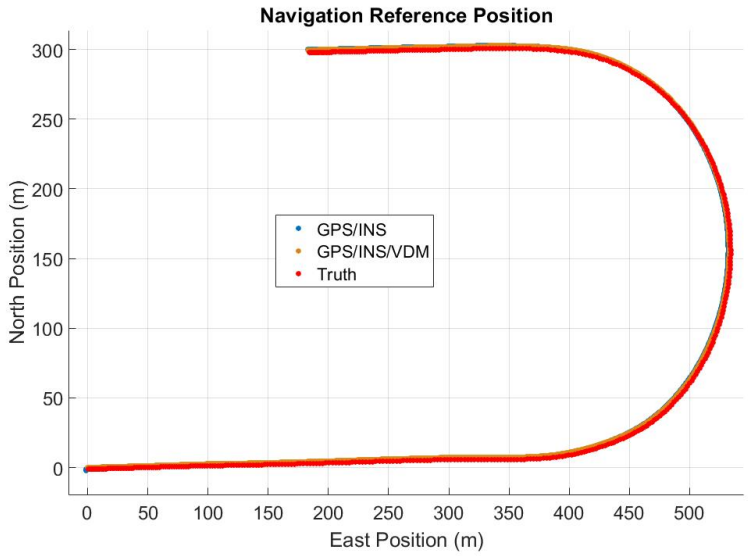

Figure 4.10: High Speed Banked Turn at NCAT Track

The curve is taken at approximately 65 mph for the entire 180° of the turn on the track. This trajectory at such a velocity is used to test system performance exceeding normal interstate driving scenarios generating lateral accelerations of approximately 5 m/s^2. Figure 4.11 through Figure 4.13 demonstrate the same error analysis plots as seen for the double lane change maneuver in Section 4.1.3.

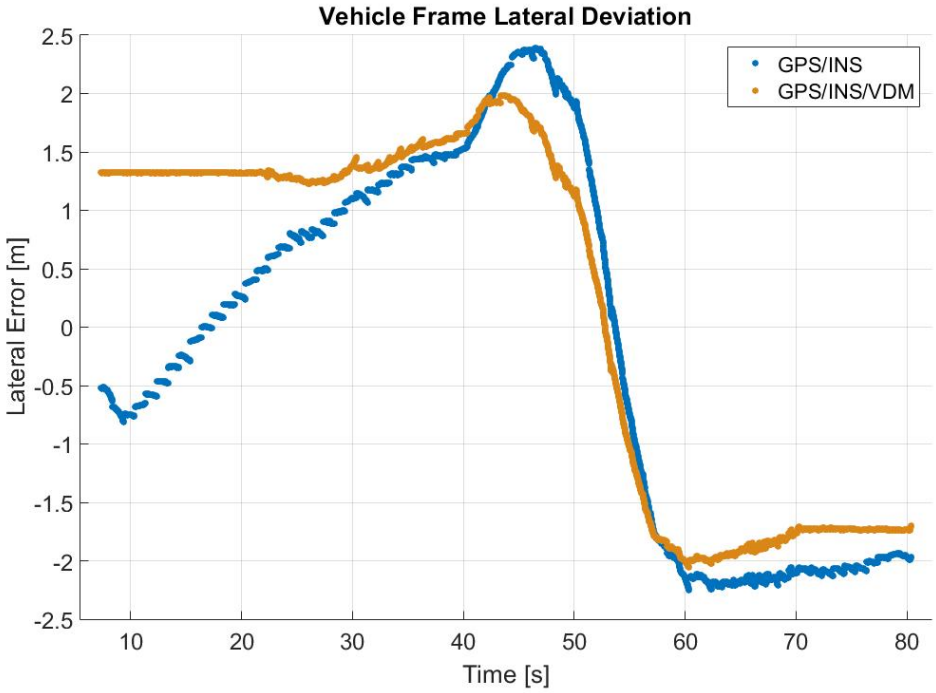

Figure 4.11: 65 mph Track Vehicle Frame Lateral Position Deviation from Ground Truth

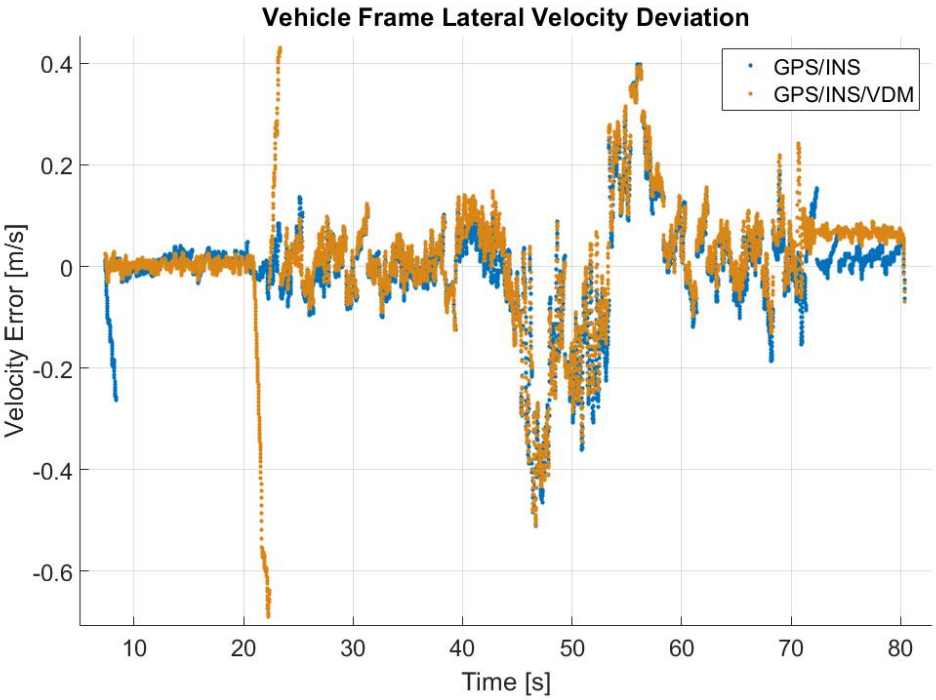

Figure 4.12: 65 mph Track Vehicle Frame Lateral Velocity Deviation from Ground Truth

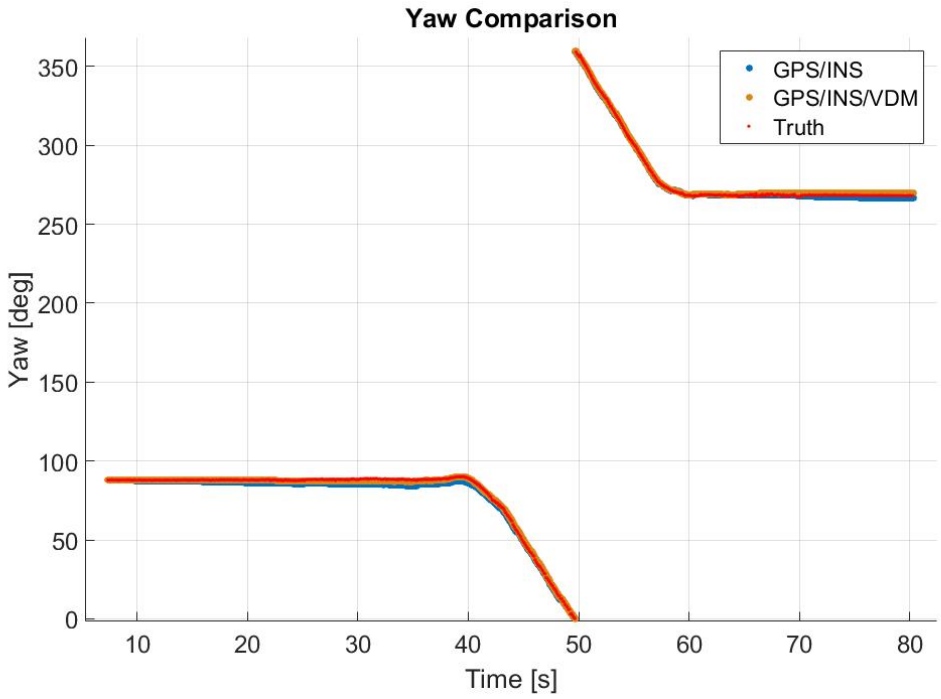

Figure 4.13: 65 mph Track Vehicle Yaw Visualization

Note that the localization algorithm including the vehicle dynamic model degraded performance at the high dynamics required to perform a double lane change. However, the GPS/INS/VDM algorithm at least matches, and in some cases exceeds, the performance of the GPS/INS algorithm even in situations with dynamics considered above the threshold of everyday interstate driving. This point is further illustrated by considering the vehicle frame longitudinal position and velocity error analysis in Figure 4.14 and Figure 4.15.

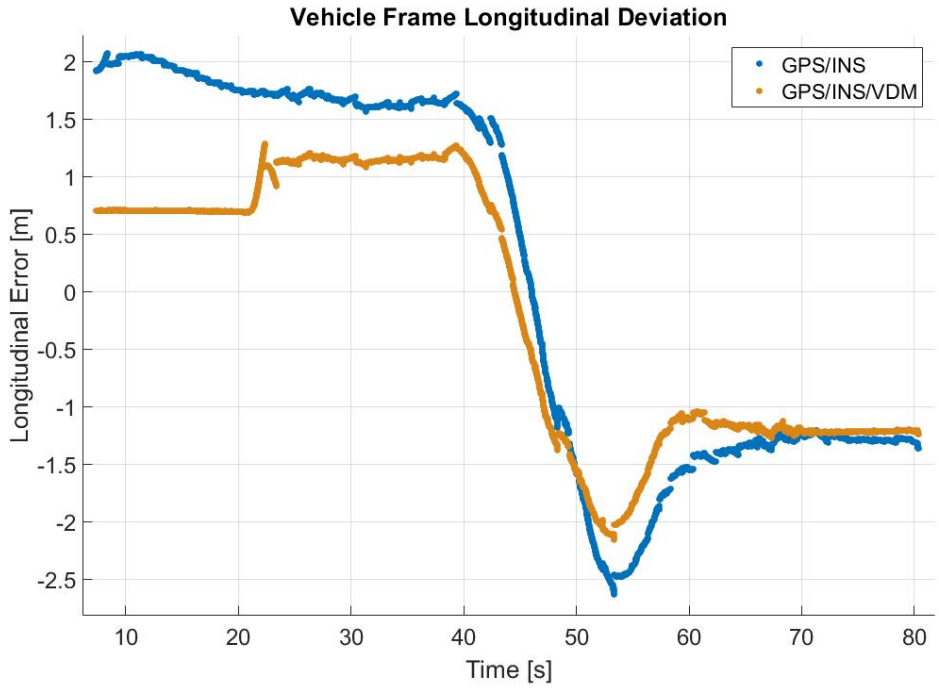

Figure 4.14: 65 mph Track Vehicle Frame Longitudinal Position Deviation

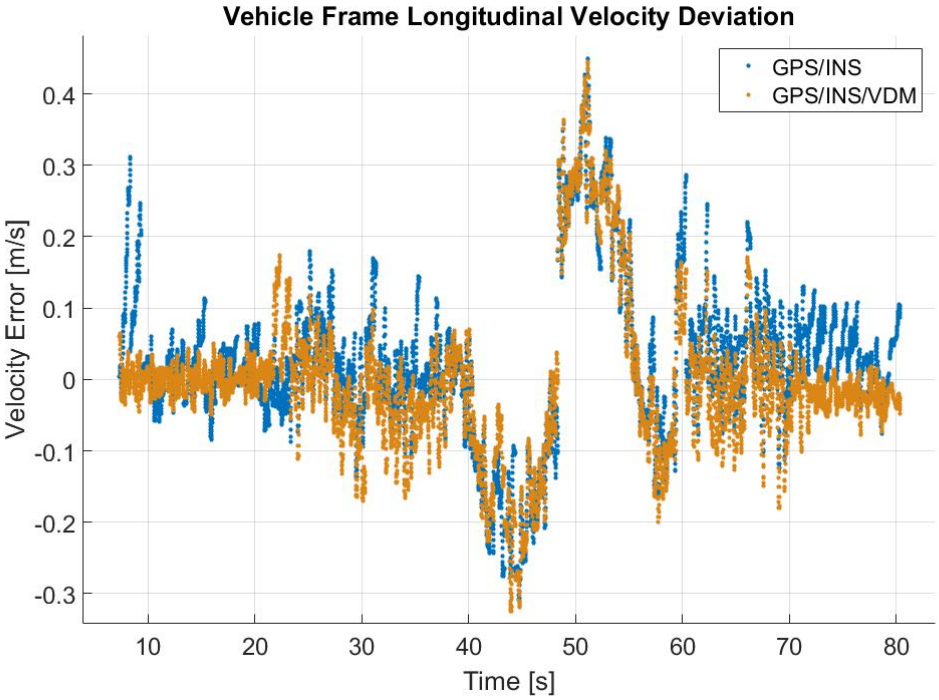

Figure 4.15: 65 mph Track Vehicle Frame Longitudinal Velocity Deviation

The global position bias that shifts from positive to negative or vise versa seen in Figure 4.11 and Figure 4.14 are products of the global offset between the low-cost GPS receiver and the RTK-GPS receiver. The reason for the bias shift can be visualized in Figure 4.16. Note that as the vehicle performs the 180° turn that the ground truth position offset shifts from the driving direction right side of the vehicle to the driving direction left side of the vehicle. The bias offset remains nearly constant in the East and North reference frame.

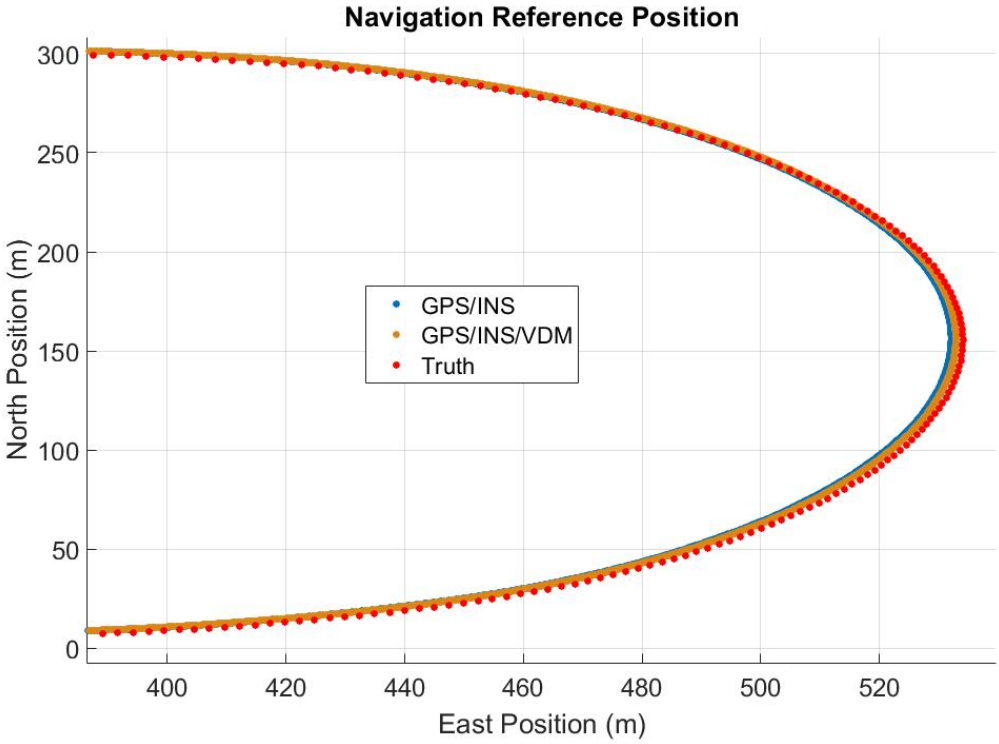

Figure 4.16: Demonstration of Position Bias to Ground Truth

Back Road

The final experimental dataset used to quantify algorithm performance for the GPS/INS and GPS/INS/VDM navigation filters is collected on a simple back road near the NCAT track. This route is heavily wooded and contains many trajectory alterations. Due to the lack of GNSS line of sight to most SV's along this route, a comprehensive data analysis is not possible. A visual of position solutions overlaid on a map, seen in Figure 4.17, is used as

a reference for visual analysis of performance of both localization algorithms in the presence of sporadic GPS coverage.

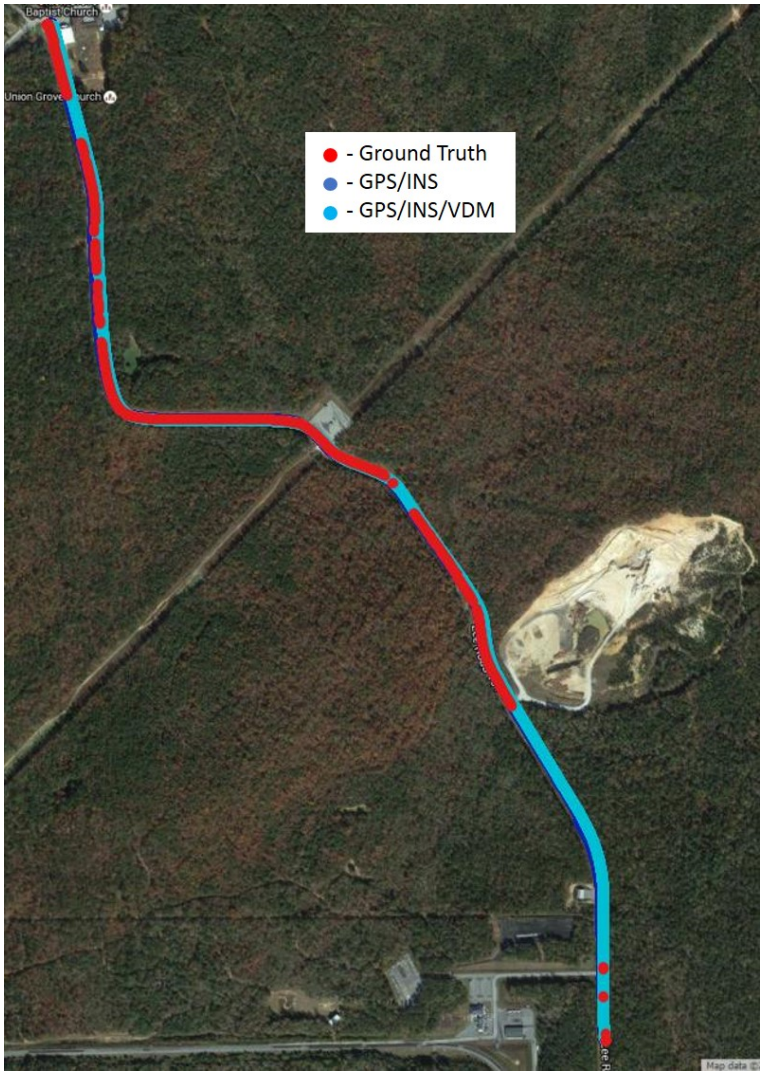

Figure 4.17: Backroad Position Solution Overlaid on Map

Note that both localization algorithms maintain accurate trajectory based on assumptions of the trajectory of the road seen in the map even when the ground truth system fails.

4.2 GPS/INS/VDM Complementary Covariance Filtering

The original goal of the research presented in this thesis was to determine if the use of a vehicle dynamic model and basic vehicle sensors would yield any benefits over a standard

GPS/INS navigation solution. The results presented throughout this Section 4.1 have proven that there is benefit in inclusion of the vehicle dynamic model and basic vehicle sensors when designing a low cost solution. The GPS/INS/VDM system performs at least as well as the GPS/INS algorithm and at times actually better than the GPS/INS algorithm in all except the high dynamic scenarios that could be experienced by an autonomous vehicle. The greatest restriction to both systems in all scenarios is the lower quality of the global position solution. Research is currently being performed that will yield RTK level accuracy from a low-cost single frequency receiver [35].

The GPS/INS/VDM localization algorithm did show degraded performance in comparison to the GPS/INS algorithm in the most extreme dynamic case of the double lane change maneuver simulating obstacle avoidance at highway speeds. The failure to outperform the baseline algorithm in all scenarios gives way to the research presented in this section. The greatest shortcoming of the original algorithm is the use of a constant measurement covariance that does not model the true nature of the vehicle dynamic model system and drastically limits the capabilities of the extended Kalman filter algorithm. The variance of the vehicle sensor measurements is not constant, but the change in variance of the measurements is unobservable when treating the VDM system as a standalone system. When considering the GPS/INS/VDM navigation system, it can be recognized that two of the included systems are complementary in nature. The INS and VDM generate similar measurements in the same coordinate frame as demonstrated by Figure 4.18 initially seen in Section 4.1.2.

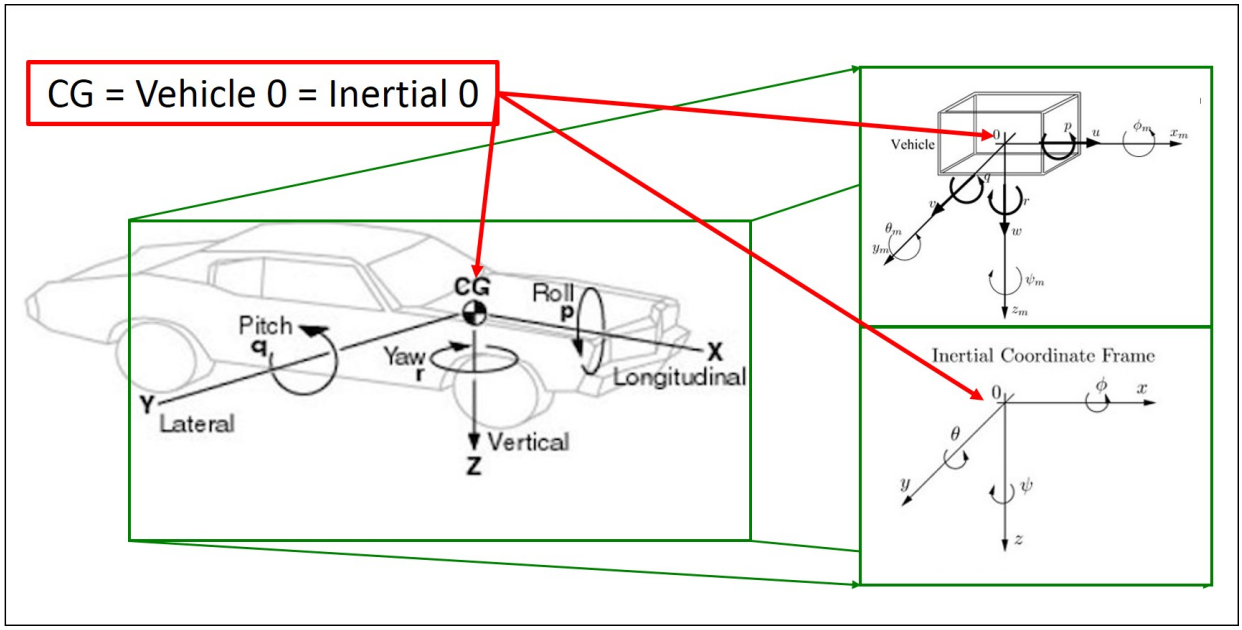

Figure 4.18: Visualization of Coordination Between Vehicle Frame and Inertial Frame

The vehicle sensor measurements can be severely degraded by external sources:

- lateral and longitudinal road grade (seen in Figure 4.19)
- lateral and longitudinal wheel slip
  - worst case: sliding and/or spinout
  - minor slip during any acceleration or braking scenario
- linear model breaks down at high dynamics

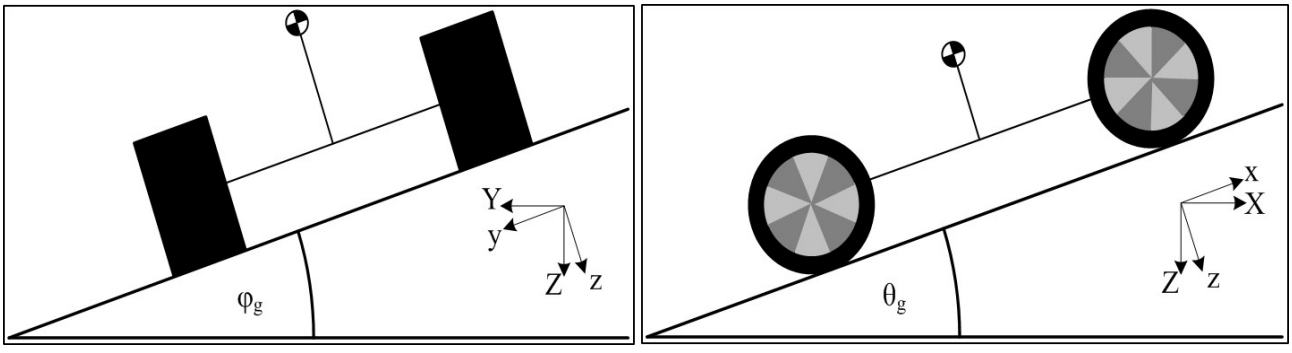

Figure 4.19: Visualization of Coordination Between Vehicle Frame and Inertial Frame

The most significant external source of error on the VDM is lateral and longitudinal wheel slip, which can be detrimental to the VDM measurement solutions in the worst case scenario. The INS measurements are virtually unaffected by these external sources. The INS suffers from high noise characteristics in terms of standalone navigation, but the INS is easily able to identify high dynamic maneuvers by simply setting a threshold on the raw IMU measurements. By monitoring the IMU raw measurements, it is possible to predict when the VDM measurements are degraded and adjust the variance on the measurements. The architecture of the navigation filter utilizing complementary covariance filtering (CCF) can be visualized using the diagram shown in Figure 4.20.

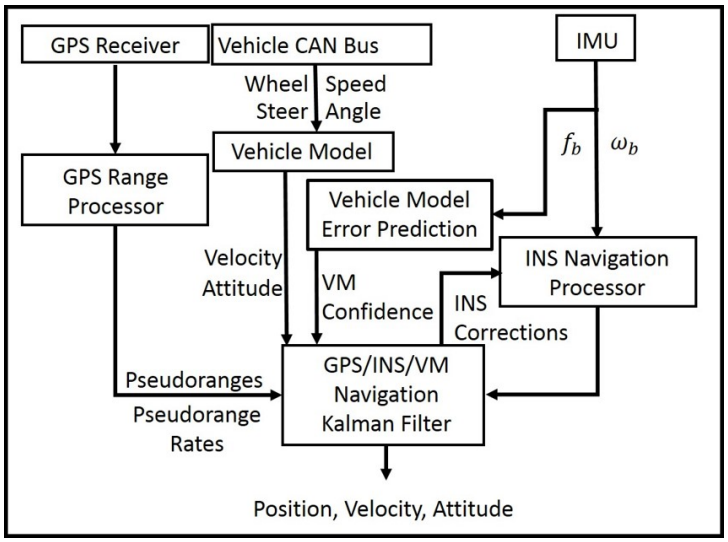

Figure 4.20: Closely Coupled GPS/INS/VDM Integration Architecture with Complementary Covariance Filtering

The complementary covariance filter algorithm analyzes the raw IMU measurements that correspond to the specific output measurements of the VDM i.e. lateral and longitudinal velocity. A thresholding technique is applied to the IMU measurements that correspond to the lateral and longitudinal velocity and the variance parameter of either the lateral velocity (σ_y^{vdm}), longitudinal velocity (σ_x^{vdm}), or both is adjusted with respect to the corresponding IMU raw measurements. The vehicle frame covariance measurements are then converted to

the ECEF coordinate frame as demonstrated in Equation (4.9).

$$R_e^{vdm} = C_b^e * \begin{bmatrix} \sigma_x^{vdm} \\ \sigma_y^{vdm} \\ \sigma_z^{vdm} \end{bmatrix} \tag{4.9}$$

Where:

$$\sigma^{vdm} = f(f_b, \omega_b) \tag{4.10}$$

4.2.1 Experimentation and Results

The complementary covariance filter version of the GPS/INS/VDM localization algorithm is designed to improve upon limitations of the original GPS/INS/VDM algorithm. Therefore, this section of the thesis will focus on the scenarios that present the greatest difficulties to a navigation algorithm. First, the parking garage scenario yielded the most drastic improvements of the GPS/INS/VDM algorithm over the GPS/INS algorithm so it is necessary to verify that the complementary covariance algorithm performs at least as well as the original algorithm including the vehicle dynamic model. Second, the double lane change maneuver must be analyzed as it demonstrates the inherent weakness of the original GPS/INS/VDM algorithm. The results from the other data collection environments discussed in previous sections of this thesis can be seen in Appendix B.

Parking Garage

Once again, the parking garage data collection environment yields the greatest weakness with the GPS/INS localization system due to the extended GNSS outage and no constraints of INS error growth. The position solution for all three localization algorithms is presented in Figure 4.21 to give a better medium for visual analysis. As expected, the CCF version of the GPS/INS/VDM algorithm performs similarly to the original algorithm. One note of

performance gain is that the CCF algorithm accepts and corrects to the GPS global updates more quickly upon reacquisition of measurements from the satellites.

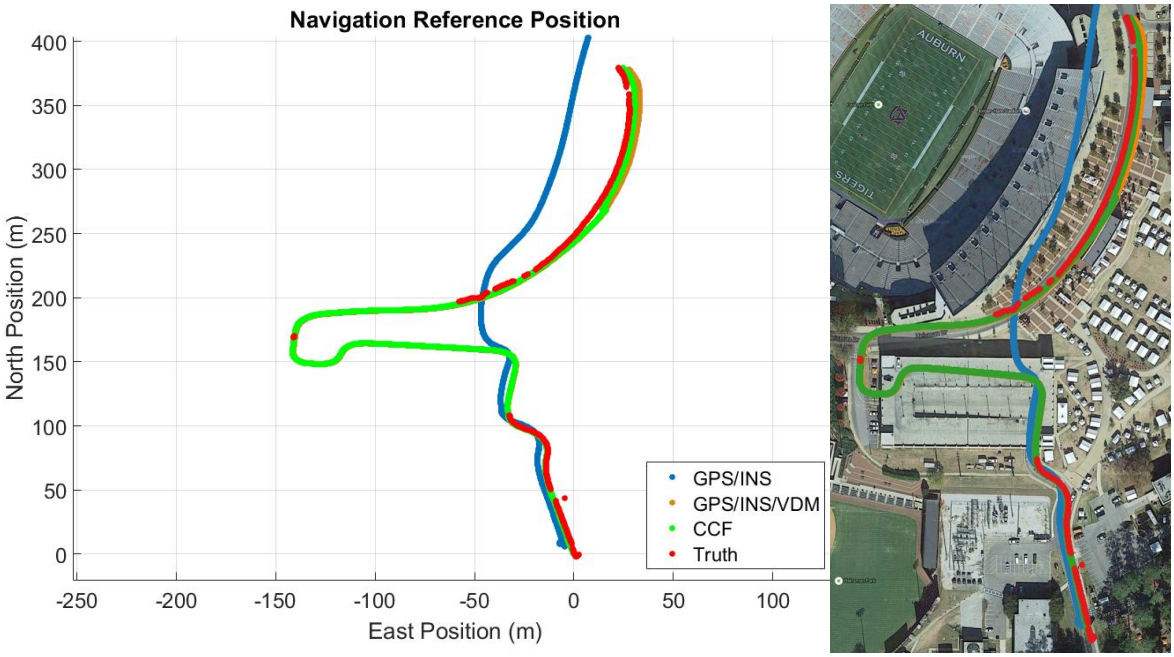

Figure 4.21: Localization Results Comparison During Extended GPS Outage

Double Lane Change

The double lane change maneuver is the one driving scenario that yields degraded performance for the original GPS/INS/VDM localization algorithm vs. GPS/INS. Figure 4.23 gives a visual overview of the solution for all three localization algorithms, as well as the ground truth solution, for the entire data collection route overlaid on a map. The performance of the new CCF algorithm is analyzed through the actual double lane change maneuver. Figure 4.22 gives a visual overview through this specific section of the data collection route.

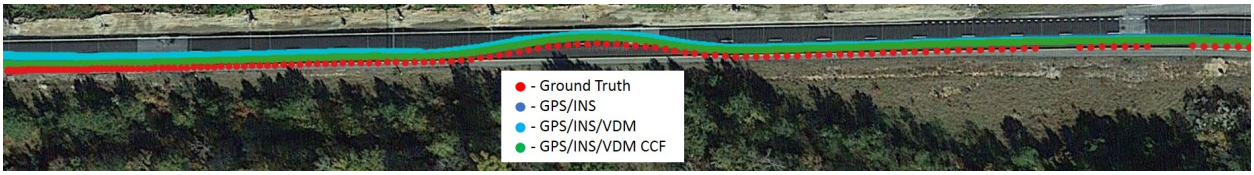

Figure 4.22: Double Lane Change Following High Speed Turn

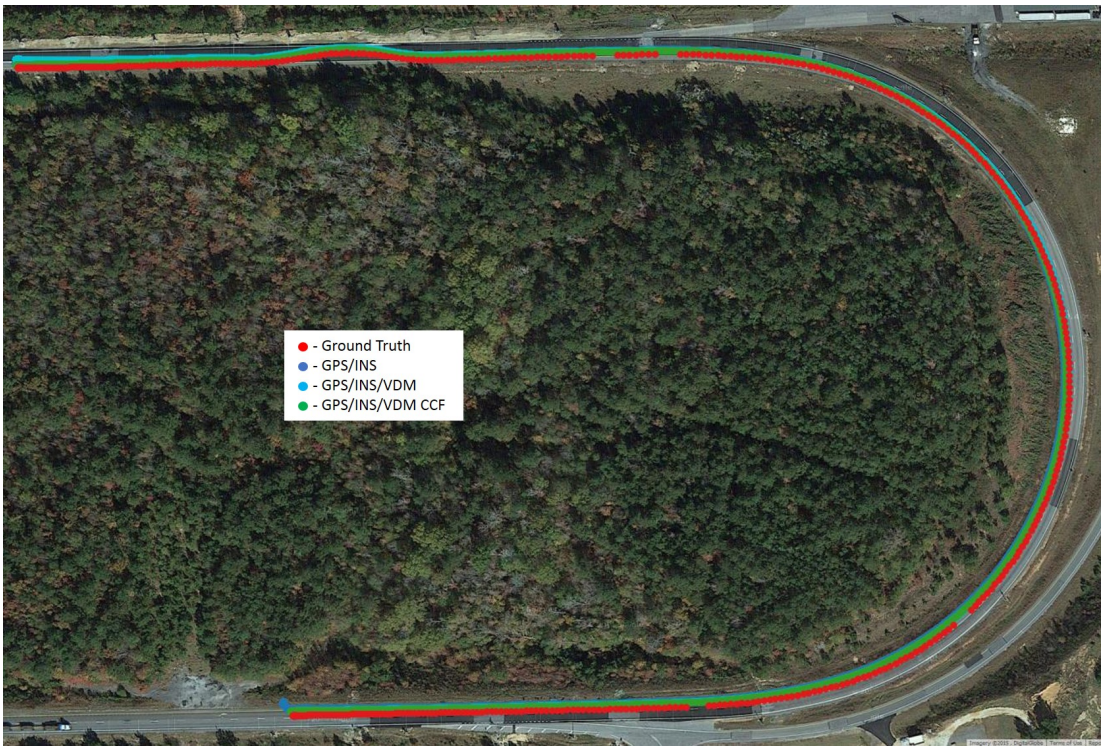

Figure 4.23: Double Lane Change Following High Speed Turn Full Route

Note that the initial visual comparison demonstrates that the CCF algorithm is not following the error trend recognized in the original GPS/INS/VDM algorithm's position solution. A zoomed in plot of the position solution for the double lane change maneuver for the GPS/INS algorithm, the GPS/INS/VDM algorithm, GPS/INS/VDM CCF algorithm, and the ground truth is presented in Figure 4.24. As mentioned in Section 3.3.2, the double lane change maneuver is performed at approximately 55 mph following an 180° turn with an 8 degree bank at an even greater velocity.

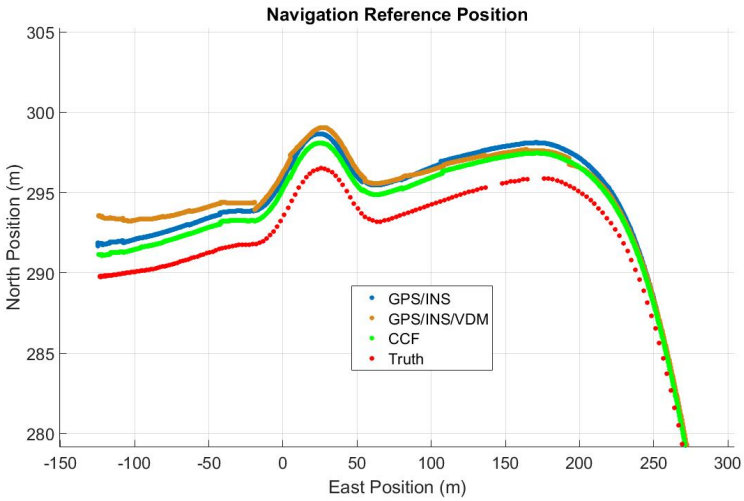

Figure 4.24: Double Lane Change East North Position Visualization

Figure 4.24 demonstrates that the new CCF algorithm resolves the inability of the original GPS/INS/VDM algorithm to handle extreme dynamic situations. A simple demonstration of the CCF algorithm increasing covariance values during periods of high dynamics is shown in Figure 4.25. These values are converted to the global coordinate frame to apply within the Kalman update.

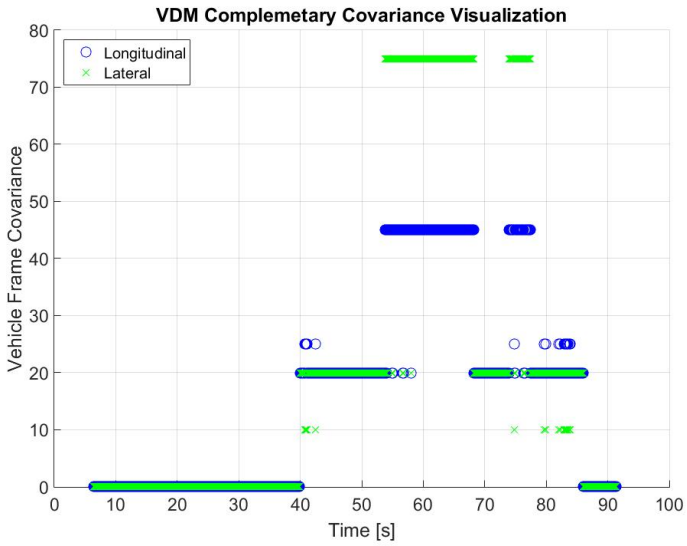

Figure 4.25: Vehicle Frame Covariance Values During Double Lane Change Maneuver

Further error analysis plots can be seen in Figure 4.26 through Figure 4.28. Note that the saw-toothing in the vehicle frame lateral velocity error seen in the original GPS/INS/VDM deviation is not present in the GPS/INS/VDM CCF algorithm solution.

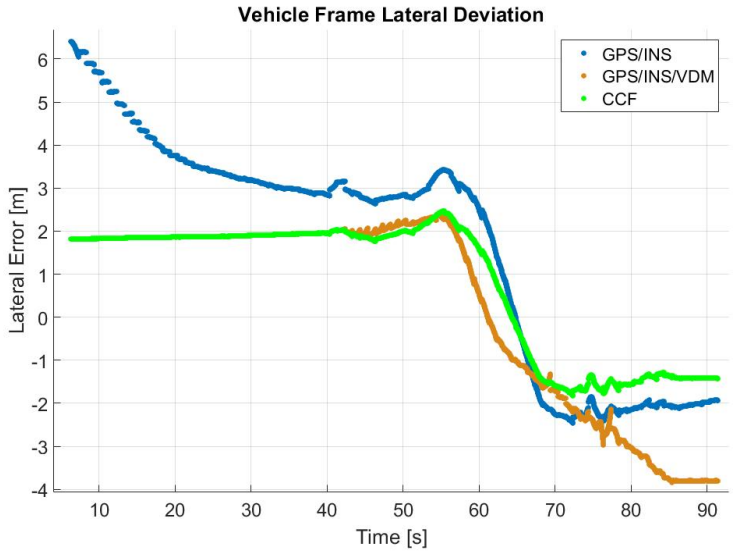

Figure 4.26: Double Lane Change Vehicle Frame Lateral Position Deviation from Ground Truth

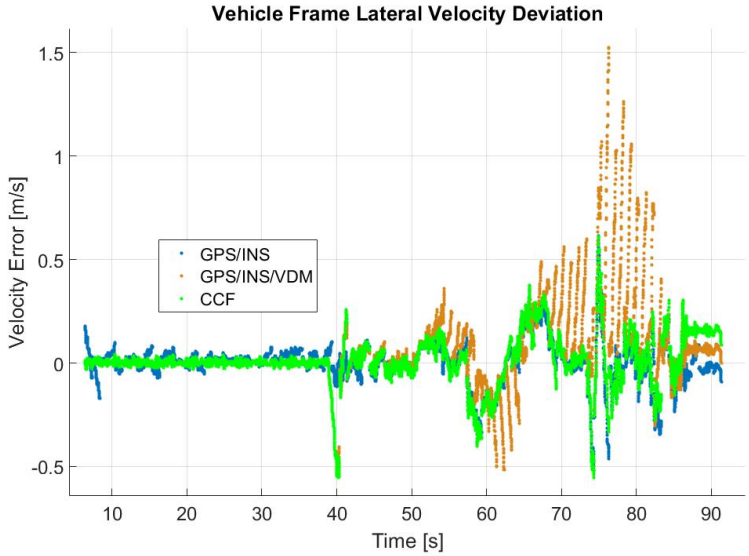

Figure 4.27: Double Lane Change Vehicle Frame Lateral Velocity Deviation from Ground Truth

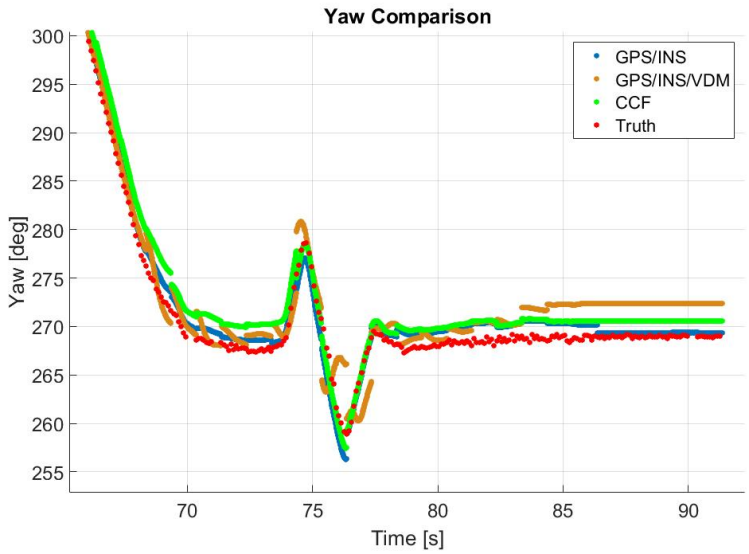

Figure 4.28: Double Lane Change Vehicle Yaw Visualization

Further error analysis plots of the entire double lane change maneuver comparing all three localization algorithm variations can be seen in Appendix B. The analysis of the high speed track run, as discussed in Section 4.1.3, comparing the solutions from all three algorithms can also be seen in Appendix B.

Back Road

The final experimental data set used to quantify algorithm performance for the GPS/INS, GPS/INS/VDM, and GPS/INS/VDM CCF navigation filters is analyzed on the back road near the NCAT track. This route is heavily wooded and contains many trajectory alterations as previously mentioned in Section 4.1.3. A visual of position solutions overlaid on a map, seen in Figure 4.29a, is used as a reference for visual analysis of performance of all localization algorithms in the presence of sporadic GPS coverage.

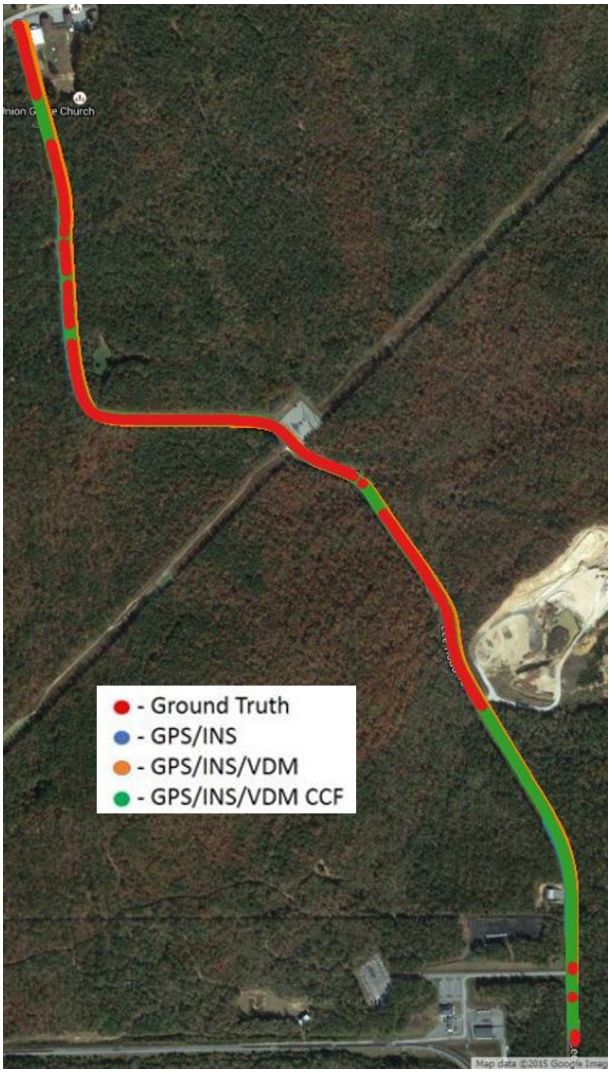

(a) Backroad Full Position Solution

(b) Backroad End Position Solution

Note that all three localization algorithms maintain accurate trajectory based on the assumption of the trajectory of the road seen in the map even when the ground truth system fails. However, upon closer visual inspection a difference between solutions was noticed at the end of the data collection route. Figure 4.29b shows the difference between position solutions. Note that both the GPS/INS algorithm and original GPS/INS/VDM position solution are shifted from the now available ground truth solution in both position and trajectory. Further visual analysis showed the original GPS/INS/VDM algorithm contains the offset in trajectory around the final curve of the route. It should be noted that while this curve was taken at relatively low speeds, approximately 40 mph, the curve is extremely

sharp and has an off camber grade. The navigation solutions of all algorithms along with ground truth entering, during, and exiting the final turn are shown in Figure 4.30. Note that the original GPS/INS/VDM localization algorithm carries a slightly altered trajectory out of the turn in comparison to the ground truth solution and GPS/INS/VDM CCF algorithm's solution.

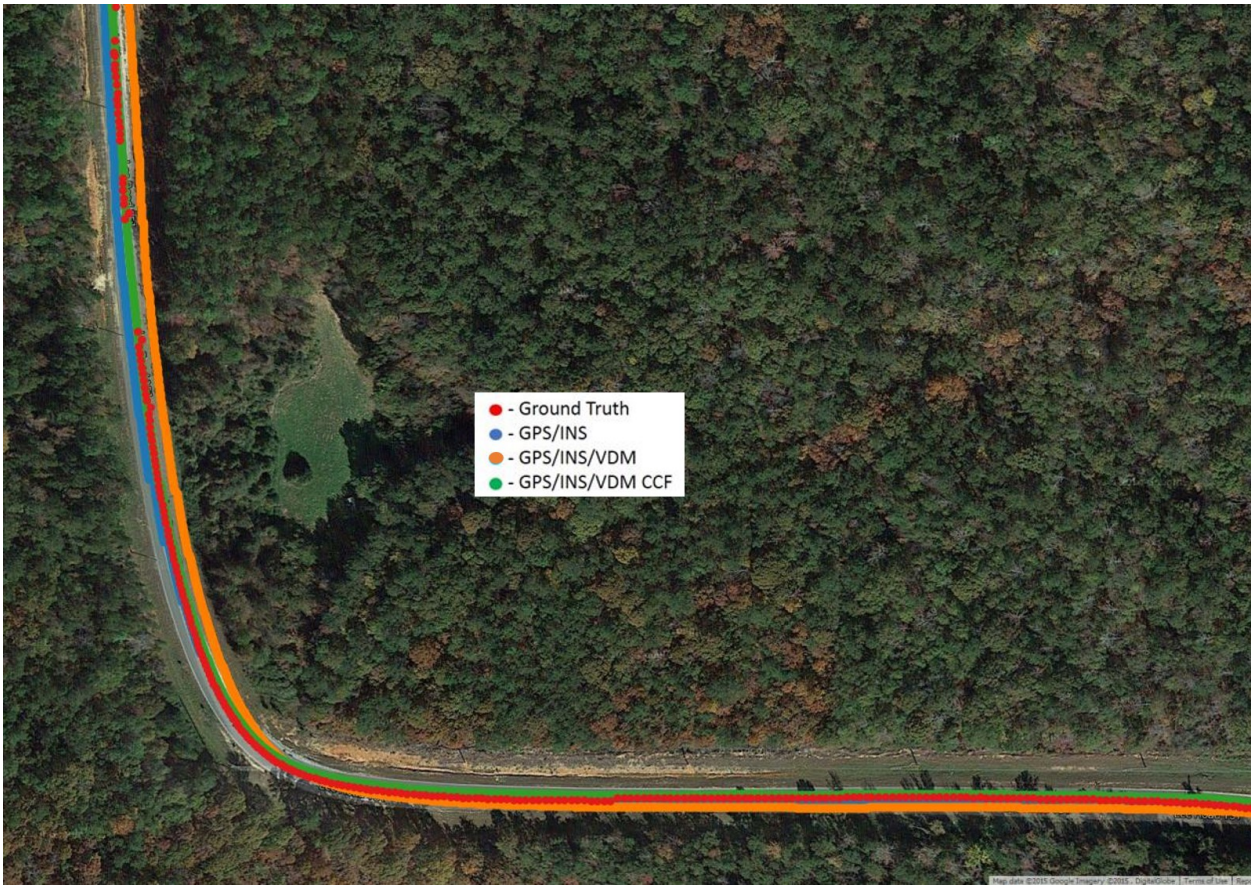

Figure 4.30: Backroad Final Turn Position Solution Overlaid on Map

4.2.2 Conclusions

Section 3.3.3 of this thesis demonstrated that the inclusion of a VDM and vehicle sensor measurements generally adds a significant advantage in overall localization solution and algorithm robustness at little to no cost added to the production of a vehicle. However, the original GPS/INS/VDM algorithm did falter under certain situations. The high dynamics

and wheel slip associated with the double lane change maneuver and other extreme scenarios generate tire forces that exceed the linear region of the tire curve as well as errors that are unobservable to the standalone vehicle dynamic model. The complementary covariance filter added to the measurement update of the GPS/INS/VDM algorithm improves the accuracy assumption of the VDM measurements during the high dynamic situations. By utilizing the fact that the quality of the VDM measurements is drastically reduced during the periods of high dynamics, the EKF algorithm is able to weight these measurement updates less heavily. With these improvements, the updated GPS/INS/VDM algorithm with complementary covariance filtering is able to achieve improved or at least equivalent performance over the baseline GPS/INS localization solution for all situations.

Chapter 5

Conclusions and Future Work

5.1 Conclusions

The question of whether or not a vehicle model and vehicle sensors would be of benefit to a GPS/INS navigation system was the initial motivation that led to the research presented within this thesis. Many researchers attempt to use vehicle model constraints to limit the error growth of lower quality IMU's; however, the nonholonomic velocity constraints associated with an Ackerman vehicle model are violated in the presence of minimal dynamic motion as shown by Ryan in [2]. With knowledge of the limitations of vehicle model constraints, utilizing the vehicle model along with vehicle sensors as a measurement system is the basis of this thesis. Multiple vehicle model variations are taken in to account to ensure the optimal balance between accuracy and simplicity as shown in Section 2.2. Also, the primary consideration for inclusion of the vehicle dynamic model measurements is the method in which to utilize the measurements within the sensor fusion algorithm. Careful consideration led to the conclusion that the optimal method for inclusion of the vehicle dynamic model measurement is through a measurement update in the EKF as described in detail in Section 4.1.2.

A benchmark GPS/INS algorithm was developed in Chapter 3 in order to have a baseline system to compare developed VDM algorithms against. The benchmark GPS/INS system utilizes the same low-cost sensors as the developed VDM algorithms. The design of the benchmark system is based on literature published by Paul Groves in [4] in order to ensure comparison to a known standard.

Initial investigations into the inclusion of a vehicle dynamic model measurement system in a sensor fused localization algorithm yielded promising results showing significant

improvement over the benchmark GPS/INS system in various scenarios. The VDM inclusion demonstrated the greatest improvements during periods of extended GPS outage at low vehicle dynamics. Utilizing the VDM measurements as a measurement update in the EKF algorithm allows the algorithm to continue to take advantage of the full Kalman filter cycle even in the absence of global positioning measurement update. The dead-reckoning measurement updates prevent the extreme drift of the localization solution generally associated with standalone INS dead-reckoning.

While the initial design GPS/INS/VDM localization algorithm provided promising improvements over the baseline in most scenarios, degraded performance was found in scenarios that include high dynamics. The degraded performance can be attributed to the constant covariance used for the VDM measurement update. An assumption of constant covariance for the measurements produced by the VDM system must be made when considering the standalone system. However, when considering all other measurements available in the GPS/INS/VDM algorithm, a complementary nature is exhibited. The INS and VDM generate similar measurement outputs in the same coordinate frame, assuming the IMU is mounted at the center of gravity of the vehicle. Since the INS can be used to detect high dynamics, an algorithm was designed that predicts VDM accuracy, or covariance, based on the measurements of the INS. The addition of the CCF in the VDM measurement update resolves the localization performance problems of the original GPS/INS/VDM algorithm seen in high dynamic situations. With the CCF improvements, the updated GPS/INS/VDM algorithm is able to achieve improved, or at least equivalent, performance over the baseline GPS/INS localization solution for all situations. Therefore, this thesis demonstrates that the inclusion of the VDM system along with ESC sensors provides an optimal low-cost ground vehicle localization solution when considering production cost and performance.

5.2 Future Work

5.2.1 Production Sensor Inclusion and Map Matching

Future work in the improvement of a low-cost system for ground vehicle navigation may see multiple updates as the pursuit of a production autonomous vehicle continues. Additional sensors, such as optical and ranging sensors, may be incorporated in order to improve robustness. These sensors can be combined with map matching techniques that could add vast improvements in both accuracy as well as robustness of the localization algorithm. A visualization of basic map matching is demonstrated by Figure 5.1. By converting the map features recognized by the optical and ranging sensors to global coordinates based on the PVT solution of the vehicle, the extracted features can be directly compared to a highly accurate stored map.

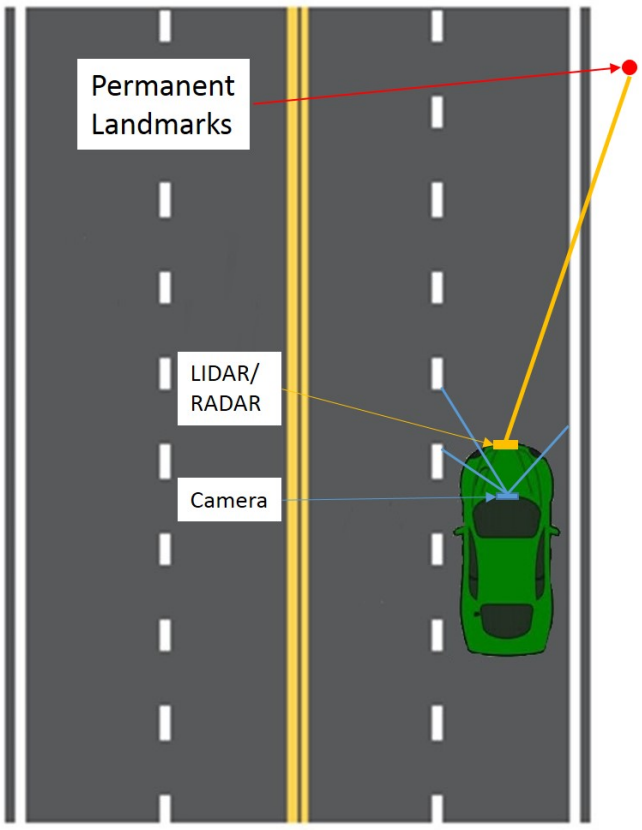

Figure 5.1: Map Matching Visualization

While the map matching technique may require high initial costs, the cost of implementation in each vehicle is negligible once the map is generated. Figure 5.2 shows possible algorithm flow chart for inclusion of all predicted production sensors into a full integration filter. Note that a map and landmark database are listed as prior knowledge which will add no cost directly to the production of a vehicle.

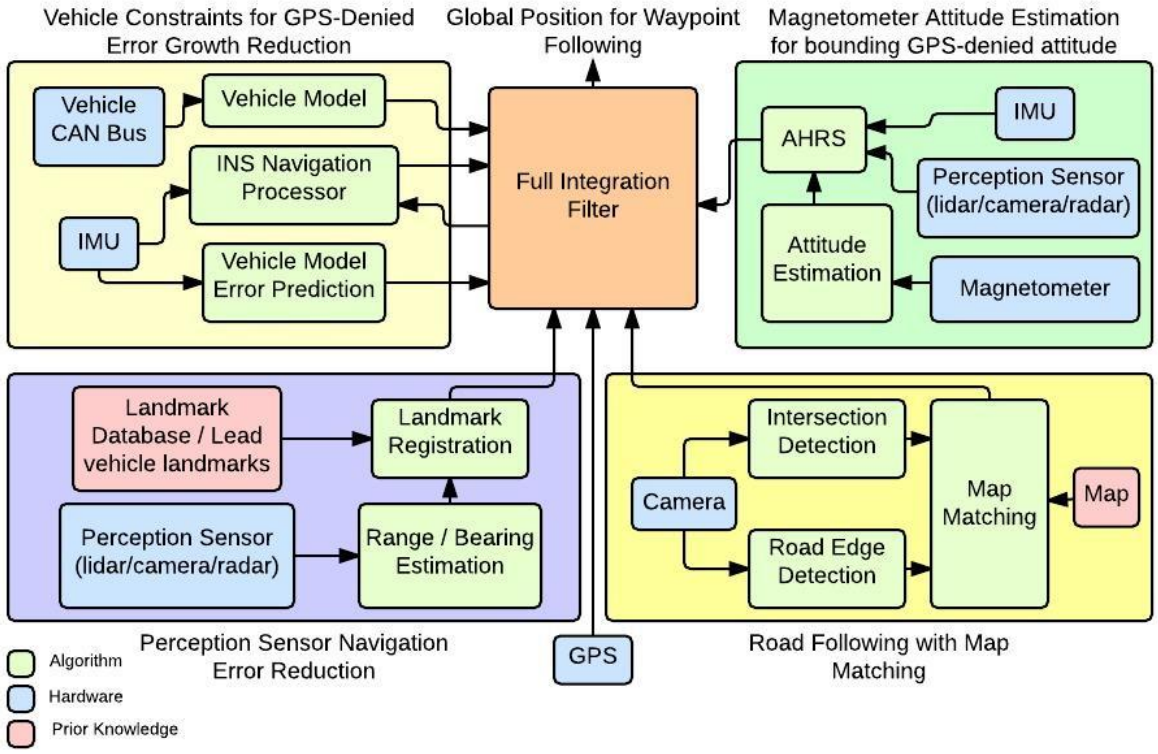

Figure 5.2: Full System Projection

The future focus of autonomous vehicle localization will be dominated by concerns for safety and robustness so that the system can recognize and handle failures of any type. Redundancy of measurements, as seen in Figure 5.2, will most likely be the optimal method to ensure the required robustness without increasing production costs.

5.2.2 On-line Estimation of Vehicle Parameters

The GPS/INS/VDM algorithm currently estimates essential vehicle parameters required by the VDM a priori. Many parameters used by the VDM can be considered constant and an a priori value estimation is acceptable. However, the vehicle mass, tire radius, and steering angle scale factor ratio can be variable between trips, or even during a single trip. As the algorithm moves to real-time, the on-line estimation of these variable vehicle parameters will become a necessity. A new state vector, seen in Equation (5.1), will be used in order to estimate the needed error states.

$$X = [\ \delta P_e \quad \delta V_e \quad \delta \Psi \quad b_a \quad b_g \quad b_{cerr} \quad b_{cdft} \quad b_{mass} \quad b_{wrad} \quad b_{str}\ ]^T \tag{5.1}$$

Where b_{mass} is the mass offset of the vehicle from the a priori estimate, b_{wrad} is the estimated scale factor offset for the a priori estimate of the radius at each wheel, and b_{str} is the scale factor offset for the a priori estimate of the ratio between the steering wheel angle and the steer angle at the wheels. On-line estimation of the variable vehicle parameters will increase the accuracy of the VDM measurements.

5.2.3 Experimental Comparison of VDM Inclusion Techniques

Finally, further methods of VDM inclusion must be analyzed in order to ensure that the inclusion of the VDM in the EKF measurement update yields the highest level of performance. Research of prior publications relating to this thesis found two methods in which the VDM could be utilized in a sensor fusion algorithm. First, the unified model technique outlined by Crocoll in [3] combines the INS and VDM by forming one augmented rigid body model out of both systems. A diagram demonstrating the propagation step of the Kalman filter utilizing the unified model is shown in Figure 5.3. The primary benefit of the unified model technique is to remove redundant measurements while utilizing both sensors in the propagation step.

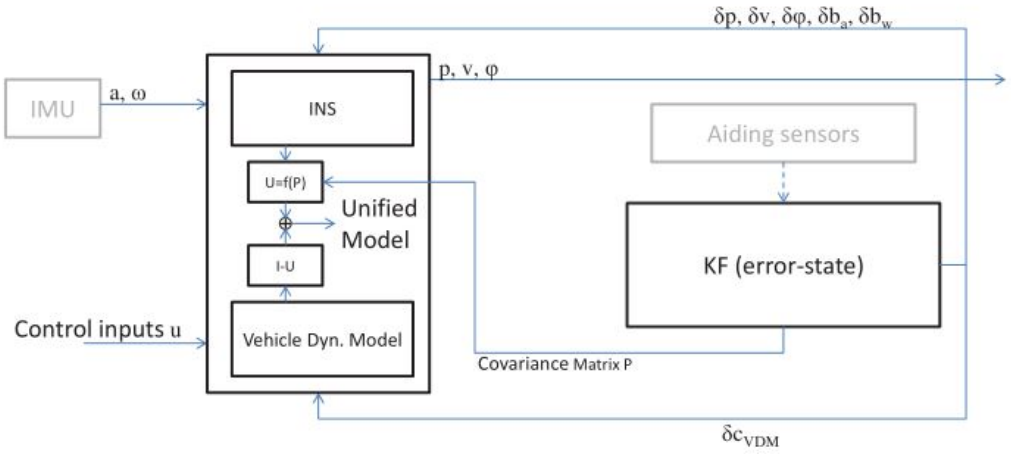

Figure 5.3: Unified Model Structure [3]

Stochastic cloning is the second technique, found throughout research, for bringing in the VDM to aid in localization. Stochastic cloning, as outlined by Roumeliotis in [36], takes into account the cross-correlation terms between state estimates of the same quantities. The state of the Kalman filter is augmented by creating two identical copies of the state estimate. The cloned state does not evolve with time, yielding a static quantity, which allows the previous state estimate to be available to evaluate the current measurement uncertainty. As the VDM is propagated forward in time, the interdependencies between measurements at concurrent time steps can be accounted for.

Both methods described in this section demonstrate a possibility for improving the localization performance of the GPS/INS/VDM algorithm. An experimental comparison of all algorithms will provide valuable information in determining the optimal method for the inclusion of VDM measurements within the EKF algorithm for localization. Though, the methods described in this thesis may still be preferred due to the ease of implementation.

Bibliography

[1] D. M. Bevly and S. Cobb, *GNSS for Vehicle Control*. Artech House, 2009.

[2] J. Ryan, "A fully integrated sensor fusion method combining a single antenna gps unit with electronic stability control sensors," Master's thesis, Auburn University, 2011.

[3] P. Crocoll, L. Gorcke, G. F. Trommer, and F. Holzapfel, "Unified model technique for inertial navigation aided by vehicle dynamics model," *ION ITM*, 2013.

[4] P. D. Groves, *Principles of GNSS, Inertial, and Multisensor Integrated Navigation Systems*. Artech House, 2013.

[5] D. Gebre-Egziabher, "Design and performance analysis of a low-cost aided dead reckoning navigator," Ph.D. Dissertation, Stanford University, 2004.

[6] E. D. Kaplan and C. J. Hegarty, *Understanding GPS: Principles and Applications*. Artech House, 2006.

[7] H. Leppakoski, H. Kuusniemi, and J. Takala, "RAIM and complementary kalman filtering for GNSS reliability enhancement," in *Proc. IEEE/ION Position, Location, And Navigation Symp*, 2006, pp. 948–956.

[8] S. Martin, "Closely coupled gps/ins relative positioning for automated vehicle convoys," Master's thesis, Auburn University, 2011.

[9] G. H. Elkaim, M. Lizarraga, and L. Pedersen, "Comparison of low-cost gps/ins sensors for autonomous vehicle applications," *ION PLANS*, pp. 1133–1144, 2008.

[10] E. Abbott and D. Powell, "Land-vehicle navigation using gps," *Proceedings of the IEEE*, vol. 87, no. 1, pp. 145–162, 1999.

[11] Y. Kubo, T. Kindo, A. Ito, and S. Sugimoto, "Dgps/ins/wheel sensor integration for high accuracy land-vehicle positioning," *ION NTM*, pp. 555–564, 1999.

[12] G. Dissanayake, S. Sukkarieh, E. Nebot, and H. Durrant-Whyte, "The aiding of a low-cost strapdown inertial measurement unit using vehicle model constraints for land vehicle applications," *IEEE Transactions on Robotics and Automation*, vol. 17, no. 5, pp. 731–747, October 2001.

[13] J. Gao, M. G. Petovello, and M. E. Cannon, "Development of precise gps/ins/wheel speed sensor/yaw rate sensor integrated vehicular positioning system," *ION NTM*, 2006.

[14] J. Gao, "Gps/ins/g sensors/yaw rate sensor/wheel speed sensors integrated vehicular positioning system," *ION GNSS*, 2006.

[15] J. Gao, M. G. Petovello, and M. E. Cannon, "Gps/low-cost imu/onboard vehicle sensors integrated land vehicle positioning system," *EURASIP Journal on Embedded Systems*, 2007.

[16] T. Li, M. G. Petovello, and G. Lachapelle, "Ultra-tight coupled gps/vehicle sensor integration for land vehicle navigation," *Navigation*, vol. 57, no. 4, pp. 248–259, 2010.

[17] A. Somieski, C. Hollenstein, E. Favey, and C. Schmid, "Low-cost sensor fusion dead reckoning using a single-frequency gnss receiver combined with gyroscope and wheel tick measurements," *ION*, 2010.

[18] A. C. Hazlett, "Differential wheel speed sensor integration with gps/ins for land vehicle navigation," Master's thesis, State University of New York at Buffalo, 2013.

[19] A. C. Hazlett, J. L. Crassidis, D. P. Fuglewicz, and P. Miller, "Differential wheel speed sensor integration with gps/ins for land vehicle navigation," *American Institute of Aeronautics and Astronautics*.

[20] P. Bonnifait, P. Bouron, D. Meizel, and P. Crubille, "Dynamic localization of car-like vehicle using data fusion of redundant abs sensors," *Navigation*, vol. 56, pp. 429–441, 2003.

[21] M. Kochem, N. Wagner, C. Hamann, D. Hamann, and R. Isermann, "Data fusion for precise dead reckoning of passenger cars," in *IFAC 15th Triennial World Congress*, 2002.

[22] D. Betaille and P. Bonnifait, "Vehicle modeling and multi-sensor smoothing techniques for post-processed vvehicle localisation," *ION*, 2002.

[23] X. Ma, S. Sukkarieh, and J.-H. Kim, "Vehicle model aided inertial navigation," *IEE Proceedings Intelligent Transportation Systems*, vol. 2, pp. 1004–1009, October 2003.

[24] W. Travis, "Methods for minimizing navigation errors induced by ground vehicle dynamics," Master's thesis, Auburn University, 2006.

[25] F. A. P. Lie and D. Gebre-Egziabher, "Synthetic air data system," *Journal of Aircraft*, vol. 50, no. 4, August 2013.

[26] M. Koifman and I. Y. Bar-Itzhack, "Inertial navigation system aided by aircraft dynamcs," *IEEE Transactions on Control Systems Technology*, vol. 7, no. 4, pp. 487–493, July 1999.

[27] D. C. Salmon and D. M. Bevly, "An exploration of low-cost sensor and vehicle model solutions for ground vehicle navigation," *ION PLANS*, pp. 462–471, 2014.

[28] B. W. Parkinson and J. J. Spilker, *The global positioning system: theory and applications volume I.* Aiaa, 1996.

[29] A. Dempster, "Correlators for l2c: Some considerations," *Inside GNSS*, vol. 1, no. 7, pp. 32–37, October 2006.

[30] G. Seeber, *Satellite geodesy*. Walter De Gruyter Inc, 2003.

[31] M. Grewal, L. Weill, and A. Andrews, *Global Positioning Systems, Inertial Navigation, and Integration*. john Wiley and Sons, Inc., 2001.

[32] H. Olsson, "Vehicle data acquisition using can," OptimumG, Tech. Rep., 2012. [Online]. Available: http://www.optimumg.com/docs/CANTechTip.pdf

[33] T. D. Gillespie, *Fundamentals of Vehicle Dynamics*. Society of Automotive Engineers, Warrendale, PA, 1992.

[34] J. Wall, "A study of the effects of stochastic inertial sensor errors in dead-reckoning navigation," Master's thesis, Auburn University, August 2007.

[35] G. Wbbena, M. Schmitz, and A. Bagge, "Ppp with ambiguity resolution using rtcm-ssr," *IGS Workshop, 23.-27.06.2014, Pasadena, CA, USA*, 2014.

[36] S. I. Roumeliotis and J. W. Burdck, "Stochastic cloning: A generalized framework for processing relative state measurements," *Robotics and Automation*, vol. 2, pp. 1788–1795, May 2002.

Appendix A

Navigation Coordinate Frames and Transformations

Coordinate frames and coordinate frame transformations are a crucial component of any navigation algorithm. Precision navigation of any object requires the knowledge of the object's position, velocity, and orientation with respect to a frame of reference. The navigation frame of reference can be a global reference or local reference which describes the object's position, velocity, and orientation with respect to an initial position or origin. Many different sensors require certain reference frames in order to yield proper measurements. For example, a GPS unit outputs measurements in some form of global reference frame and an IMU only has the ability to give measurements that apply to the body frame of the IMU or whichever vehicle it is mounted. For this reason, sensor fused navigation requires constant conversion between coordinate reference frames. The remainder of this chapter will focus on the coordinate frames used in the navigation algorithms researched in this thesis and the conversions between each reference frames.

A.1 Global Reference Frames

Global reference frames are essential to a GPS receivers calculation of position and velocity. As described previously, GPS calculations are based on the relative distance and velocity between the receiver and any visible satellite vehicle. As all standard GPS satellite vehicles are not located on the Earth, a reference frame is required in order to relate that off Earth position and velocity in a vector form to a receiver position and velocity on Earth or near Earth. The Earth-Centered-Earth-Fixed or ECEF reference frame is most often recognized as the standard global reference frame for navigation. The ECEF frame works well for defining position and velocity but has limitations when visualization of position

is required due to the fact that it is based on an origin at the center of the Earth. The Geodetic Reference System is an alternate coordinate system for the Earth that allows a visualization advantage by defining positions based on the surface of the Earth. Both global reference frames are based on the World Geodetic System (WGS) or specifically the latest revision, WGS 84. WGS 84 comprises of a standard model of the Earth's geoid and Earth's gravitational field that consists of the parameters listed in Table A.1 [4]. Each global coordinate frame and their relation to each other are visually described by Figure A.1.

Table A.1: Parameters of the WGS84 Ellipsoid(From: [4])

Parameter	**WGS84 Value**
Equatorial Radius, R_0	6,378,137.0 m
Polar Radius, R_P	6,356,752.31425 m
Flattening, f	1/298.257223563
Eccentricity, e	0.0818191908425

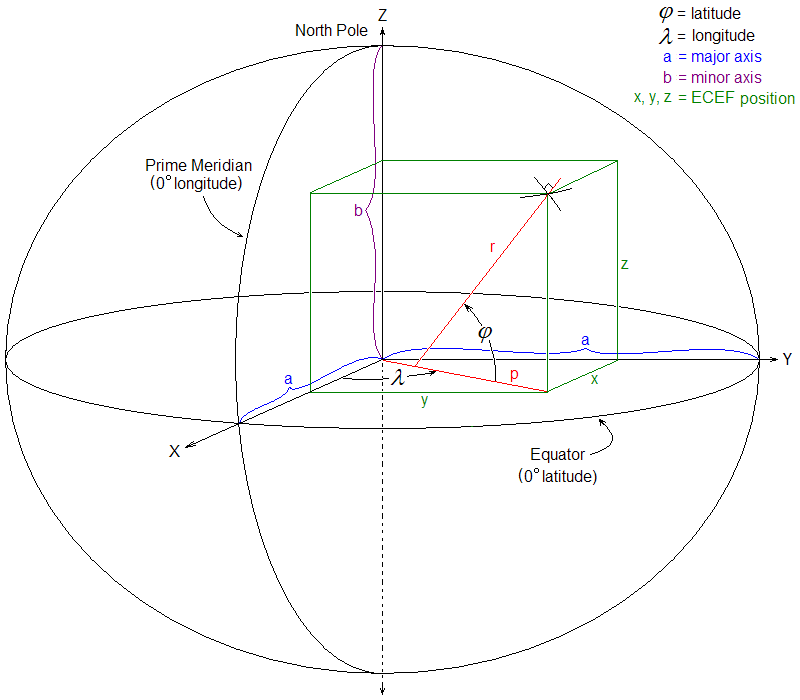

Figure A.1: Visualization of Global Coordinate Frames

A.1.1 ECEF Reference Frame

The ECEF coordinate reference frame is a three axis, X, Y, and Z, frame with an origin at the Earth's center of mass. The Z-axis extends from the origin towards the north pole (true not magnetic) along the Earth's axis of rotation. The X-axis is at a 90° offset from the Z-axis and points from the origin towards the point in which the Earth's equator and prime meridian intersect. The Y-axis is at a 90° offset from the the Z-axis and the X-axis and points at a point on the Earth's equator located 90° east of the Earth's prime meridian. Any variable described in the ECEF frame will be denoted by (e) [4]. The ECEF coordinate reference frame is used as the primary reference frame for all navigation algorithms in this thesis.

A.1.2 Geodetic Reference System

The geodetic reference system is based on the Earth's surface, as previously stated, and comprises of three mutually orthogonal coordinates. The geodetic latitude, L, is the angle of intersection between a line drawn normal to the ellipsoid to a point on the surface of the ellipsoid and the equatorial plane. Geodetic latitude differs from geocentric latitude in that geocentric is the angle between the equatorial plane and a line to the point of interest from the center of the earth as seen in Figure A.2. The exact difference between geocentric and geodetic latitude is seen in (A.1), where geocentric latitude is described by Φ.

$$tan\Phi = (1 - e^2)tanL \tag{A.1}$$

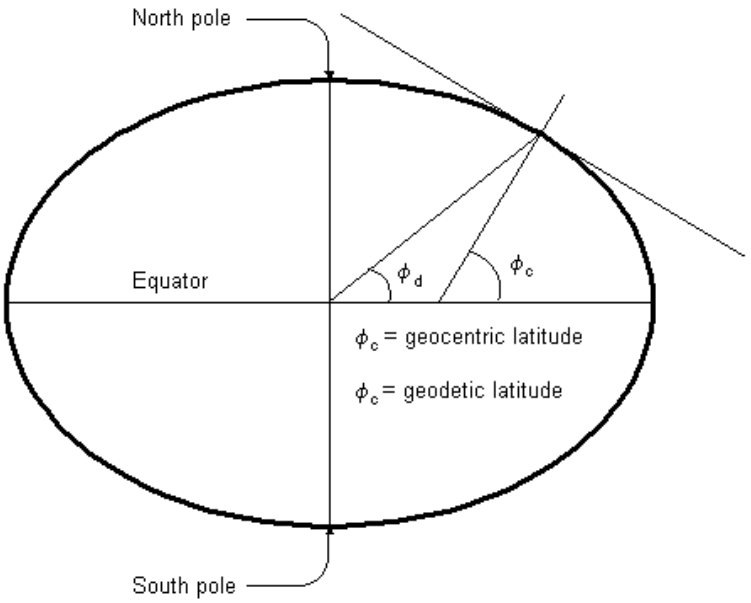

Figure A.2: Geodetic vs Geocentric Latitude

Conventionally latitude is positive in the northern hemisphere and negative in the southern hemisphere. The longitude, λ, is the angle between the point of interest and the prime meridian subtended in the equatorial plane. Longitude is typically positive in the eastward

direction from the prime meridian and negative in the westward direction. The height, h, is defined as height above nominal sea level which is also known as altitude. The geodetic reference system is essential for conversions between the ECEF frame and local coordinate frames [4].

A.2 Local Reference Frame

A local navigation frame is necessary in order to define an object's orientation. This thesis uses the East-North-Up (ENU) reference frame which is denoted l and in which the axes are aligned with the topographic directions: east, north, and vertical as seen in Figure A.3. The origin of the local reference frame is defined by the initialization of the navigation algorithm. The Euler attitude angles are used to describe a vehicle's orientation relative to the local navigation frame. The Society of Automotive Engineers (SAE) defines the Euler angles of a vehicle as seen in Figure A.4 where zero roll, pitch, and yaw equates to the vehicle sitting perfectly tangential to Earth's ellipsoid and the front of the vehicle directed toward the North.

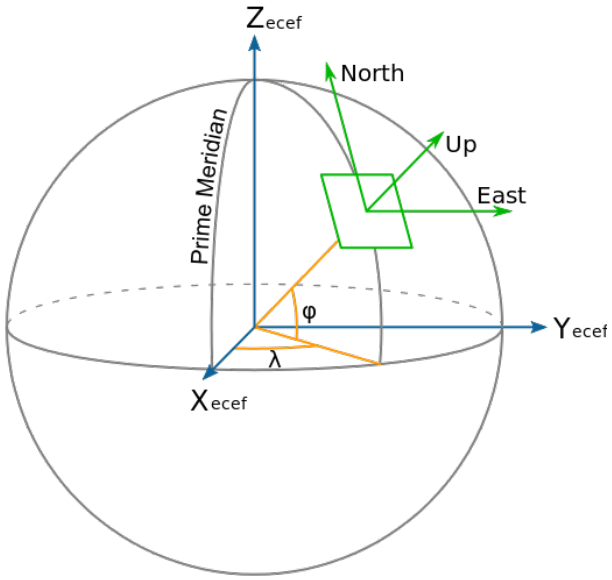

Figure A.3: ENU Reference Frame

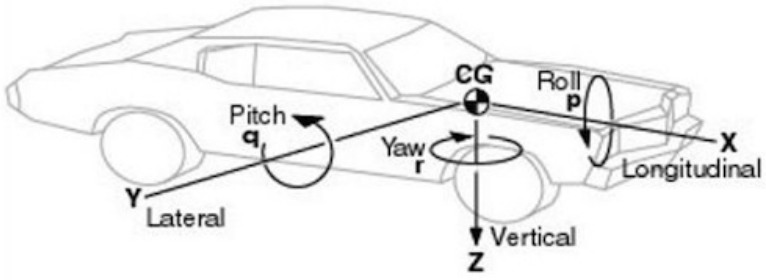

Figure A.4: SAE Reference Frame

A.3 Body Reference Frame

The body frame or vehicle frame describes the reference frame with origin at the objects center of mass. The body frame maintains the alignment shown in Figure A.4 and the axes remain fixed with respect to the body at all times. The body frame is essential to navigation when using inertial sensors. Assuming the inertial sensor is mounted at or near enough to the body center or gravity to yield negligible errors, all axes of a 6-DOF IMU will align with the body frame of the given vehicle and maintain this relationship throughout navigation. The symbol b will be used throughout this thesis to denote the body frame.

A.4 Coordinate Frame Transformations

Coordinate frame transformations are essential to any sensor fusion navigation algorithm for reasons previously stated. A simple transformation, such as the local navigation frame transformation of the ENU frame to the NED frame, is all that is needed at times. However, some transformations can be much more complex, such as the transformation from the global ECEF frame to the body frame of an object or vehicle. A detailed description and all necessary equations for each coordinate frame transformation used within this thesis can be found within the following subsections.

A.4.1 ECEF to LLH

The transformation from the global ECEF reference frame to the geodetic LLH reference frame, as well as the inverse transformation, is essential to most other transformations within this thesis. The transformation from LLH to ECEF will be described first as the inverse transformation is significantly more complex. The conversion from LLH to ECEF depends most significantly on the radii of curvature of the ellipsoid. The radii of curvature consists of two radius of curvature's. The first radius of curvature is for north-south motion, denoted R_N, which is known as the meridian radius of curvature. The second radius of curvature is for east-west motion, denoted R_E, which is known as the transverse radius of curvature. The meridian and transverse radius of curvature can be calculated as functions of geodetic latitude using (A.2) and (A.3) respectively.

$$R_N(L) = \frac{R_0(1-e^2)}{(1-e^2 sin^2 L)^{3/2}} \tag{A.2}$$

$$R_E(L) = \frac{R_0}{\sqrt{1-e^2 sin^2 L}} \tag{A.3}$$

The extra parameters required to solve (A.2) and (A.3) can be found in Table A.1 [4]. The transverse radius of curvature with respect to geodetic latitude is then used along with the geodetic LLH position coordinates to calculate the ECEF X, Y, and Z position as shown in (A.4) [4].

$$x^e = (R_E(L) + h) cosL cos\lambda \tag{A.4a}$$

$$y^e = (R_E(L) + h) cosL sin\lambda \tag{A.4b}$$

$$z^e = [(1-e^2)R_E(L) + h] sinL \tag{A.4c}$$

The conversion from ECEF to LLH is more complicated than the conversion described in (A.4) as previously stated. The height, h, is a function of latitude and the latitude, L, is a function of both height and latitude, as seen in (A.5). Therefore, latitude and height must

be solved for iteratively. Note that the four-quadrant arctangent function must be used to solve for latitude in (A.5a).

$$L = arctan_2\left(\frac{z^e[R_E(L)+h]}{\sqrt{(x^e)^2+(y^e)^2}[(1-e^2)R_E(L)+h]}\right) \tag{A.5a}$$

$$\lambda = arctan\left(\frac{y^e}{x^e}\right) \tag{A.5b}$$

$$h = \frac{sqrt(x^e)^2+(y^e)^2}{cosL} - R_E(L) \tag{A.5c}$$

A.4.2 ECEF to Local

The local navigation is essential to defining the orientation of the object or vehicle in which navigation is necessary. The transformation from the global ECEF frame to a local tangent plane can be achieved by forming a transformation matrix consisting of terms using the geodetic latitude and longitude of the local tangent-plane origin. The conversion from Earth frame to local frame is represented by (A.6) and the transformations from local to ECEF is achieved using (A.7) [4]).

$$C_e^l = \begin{pmatrix} -sinL_l cos\lambda_l & -sinL_l sin\lambda_l & cosL_l \\ -sin\lambda_l & cos\lambda_l & 0 \\ -cosL_l cos\lambda_l & -cosL_l sin\lambda_l & -sinL_l \end{pmatrix} \tag{A.6}$$

$$C_l^e = \begin{pmatrix} -sinL_l cos\lambda_l & -sin\lambda_l & -cosL_l cos\lambda_l \\ -sinL_l sin\lambda_l & cos\lambda_l & -cosL_l sin\lambda_l \\ cosL_l & 0 & -sinL_l \end{pmatrix} \tag{A.7}$$

A.4.3 Local to Body

The final direct transformation to be described converts the local tangent navigation frame to the body frame of the object or vehicle. This transformation is made up of a set of rotation matrices defined by the Euler attitude angles, roll (ϕ), pitch (θ), and yaw (ψ), as

demonstrated by (A.8), (A.9), and (A.10) respectively.

$$R_\phi = \begin{pmatrix} 1 & 0 & 0 \\ 0 & cos\phi_b^l & sin\phi_b^l \\ 0 & -sin\phi_b^l & cos\phi_b^l \end{pmatrix} \tag{A.8}$$

$$R_\theta = \begin{pmatrix} cos\theta_b^l & 0 & -sin\theta_b^l \\ 0 & 1 & 0 \\ sin\theta_b^l & 0 & cos\theta_b^l \end{pmatrix} \tag{A.9}$$

$$R_\psi = \begin{pmatrix} cos\psi_b^l & sin\psi_b^l & 0 \\ -sin\psi_b^l & cos\psi_b^l & 0 \\ 0 & 0 & 1 \end{pmatrix} \tag{A.10}$$

The rotation matrices are multiplied to form the transformation matrix as demonstrated by (A.11).

$$C_b^l = R_\phi * R_\theta * R_\psi \tag{A.11}$$

A.4.4 ECEF to Body

The global ECEF reference frame transformation to vehicle body reference frame is a reasonably simple calculation once C_b^l and C_l^e have been calculated using Equation (A.11) and (A.7) respectively. The transformation matrix for the ECEF to body frame transformation is defined as C_b^e. The ECEF to body transformation matrix is especially important throughout each navigation algorithm used in this thesis due to the fact that all attitude information is maintained through this transformation matrix. The transformation matrix is initially calculated using (A.12).

$$C_b^e = C_l^e * \left(C_b^l\right)^T \tag{A.12}$$

The roll, pitch, and yaw of the object or vehicle can be extracted from the ECEF to body transformation matrix by first calculating C_b^l using (A.13),

$$C_b^l = C_e^l * C_b^e \tag{A.13}$$

and then calculating each Euler angle using (A.14). Note that the four-quadrant arctangent function must be used in (A.14a) and (A.14c).

$$\phi = arctan_2\left(\left(C_b^l\right)_{3,2}, \left(C_b^l\right)_{3,3}\right) \tag{A.14a}$$

$$\theta = -arcsin\left(C_b^l\right)_{3,1} \tag{A.14b}$$

$$\psi = arctan_2\left(\left(C_b^l\right)_{2,1}, \left(C_b^l\right)_{1,1}\right) \tag{A.14c}$$

The Euler angles found in Equation (A.14) are used in navigation to define the orientation of the body being navigated. Defining the orientation angles in this manner also allows for easy visualization for the designer and end user of the navigation algorithm.

Appendix B

Extra Result Plots

B.1 GPS/INS

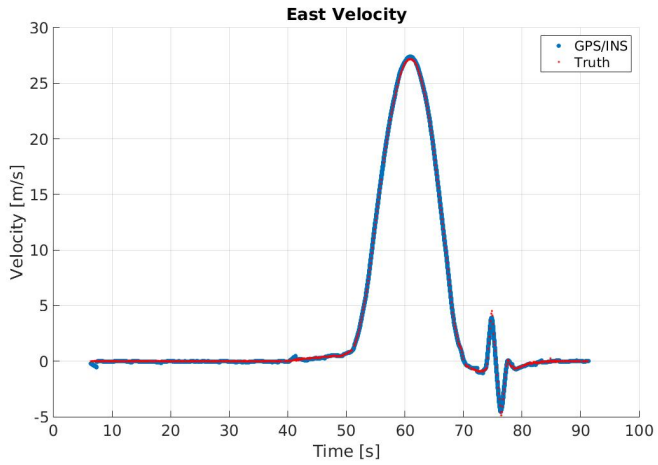

Figure B.1: Double Lane Change East Velocity Truth Compare

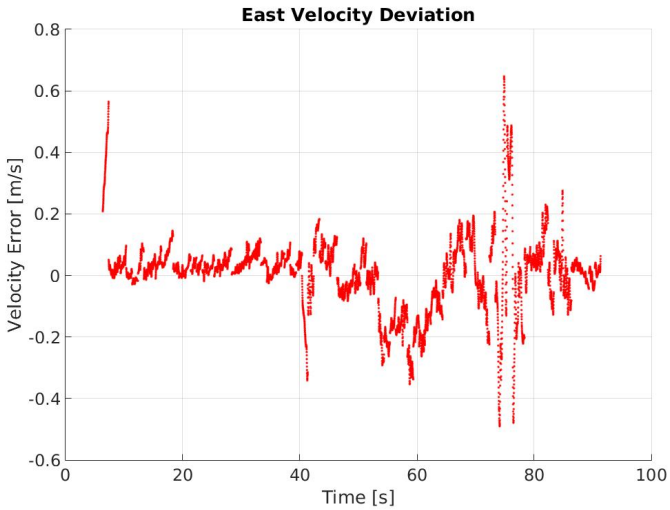

Figure B.2: Double Lane Change East Velocity Deviation from Velocity Truth Solution

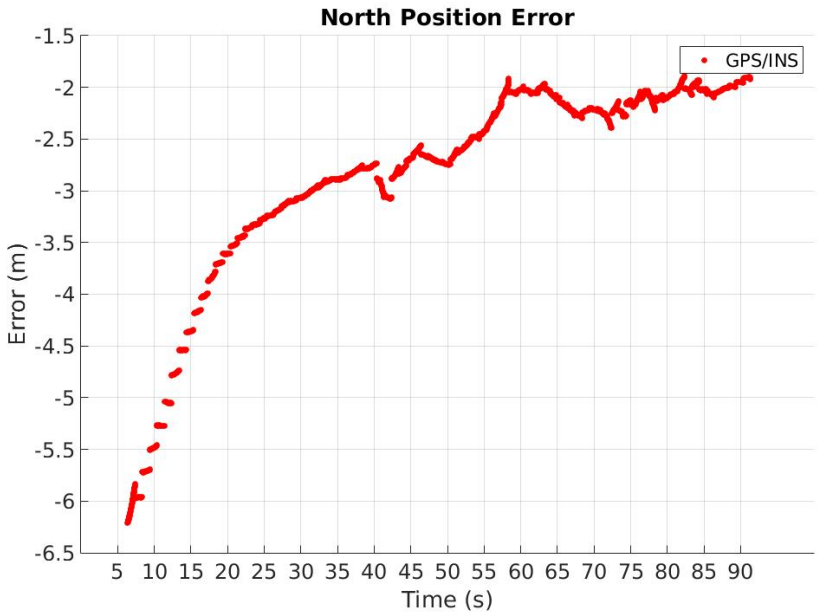

Figure B.3: Double Lane Change North Position Deviation from Truth Position Solution

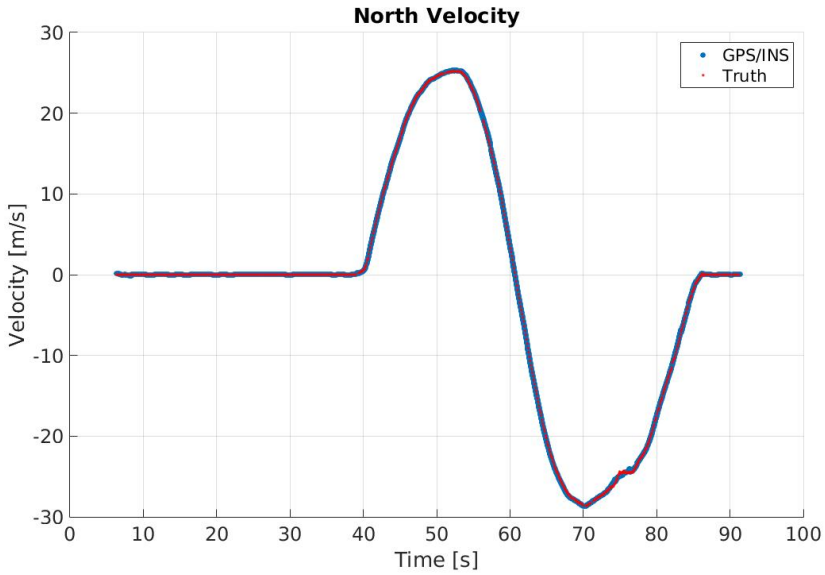

Figure B.4: Double Lane Change North Velocity Truth Compare

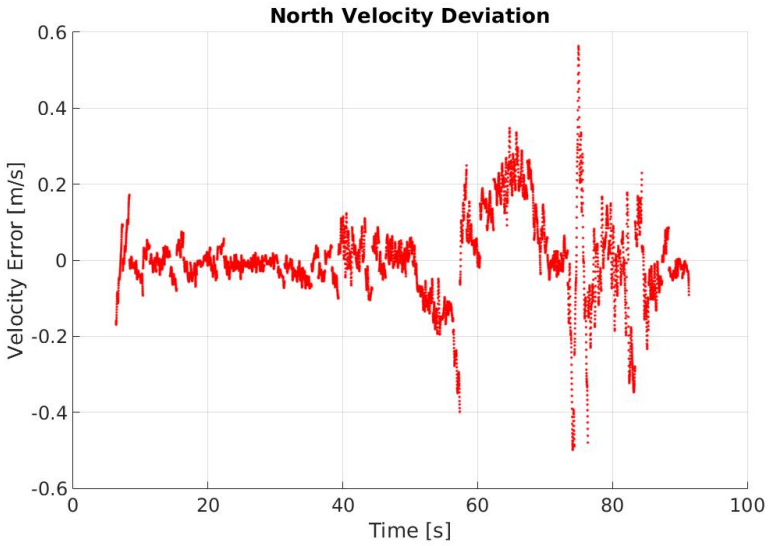

Figure B.5: Double Lane Change North Velocity Deviation from Truth Velocity Solution

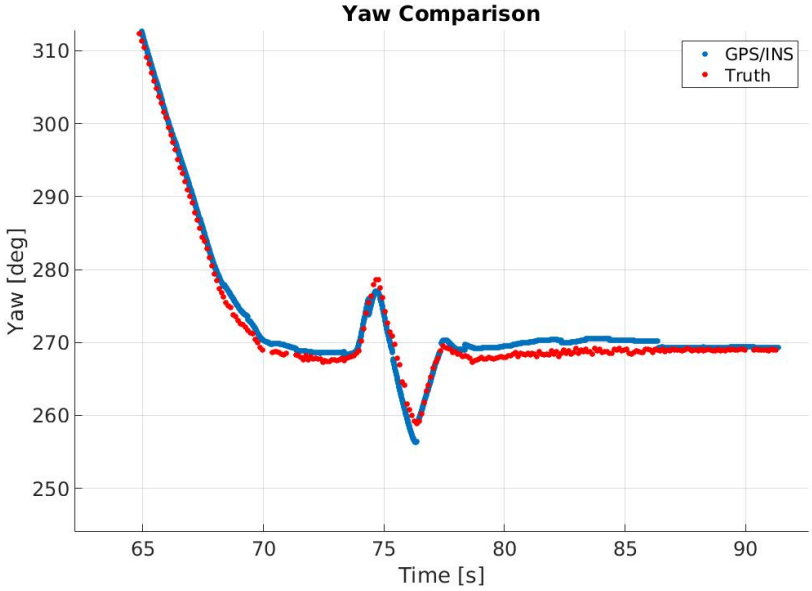

Figure B.6: Double Lane Change Yaw Truth Compare

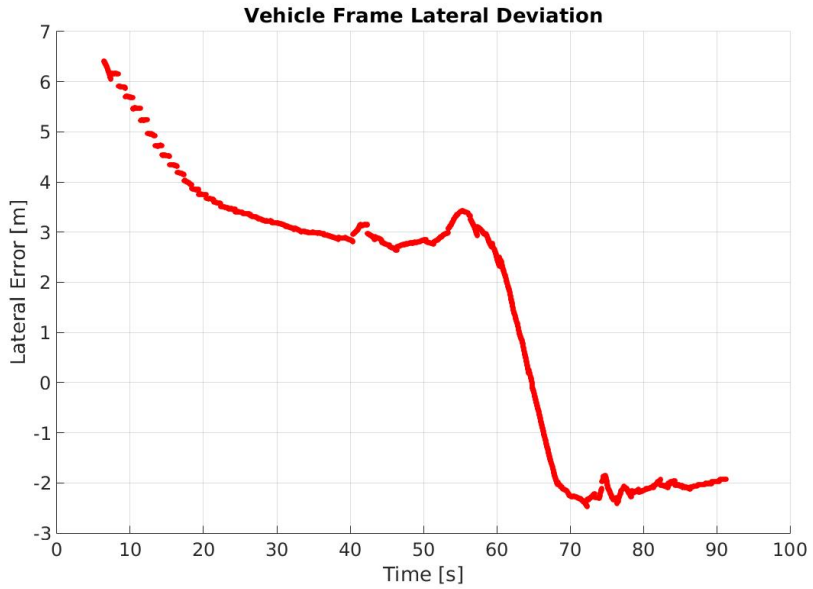

Figure B.7: Double Lane Change Vehicle Body Frame Lateral Position Error

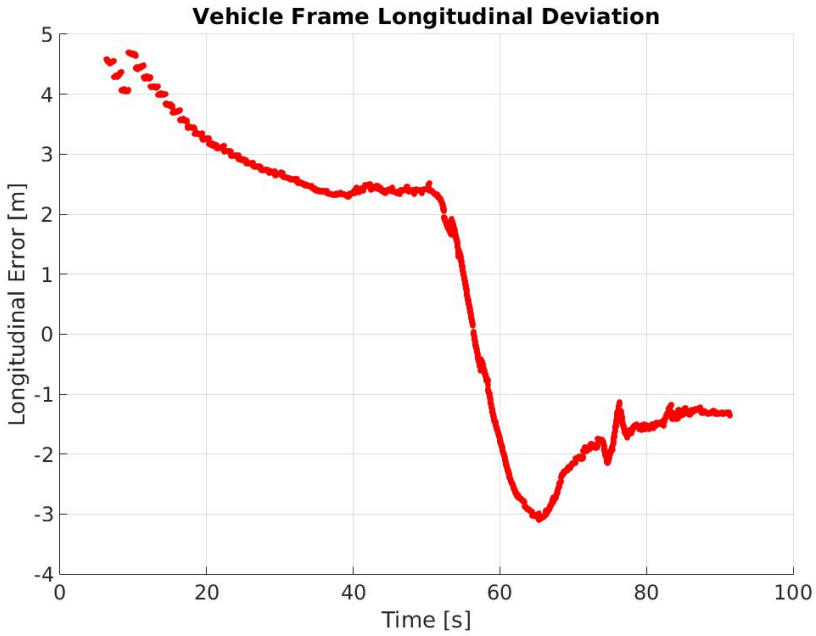

Figure B.8: Double Lane Change Vehicle Body Frame Longitudinal Position Error

B.2 GPS/INS/VDM

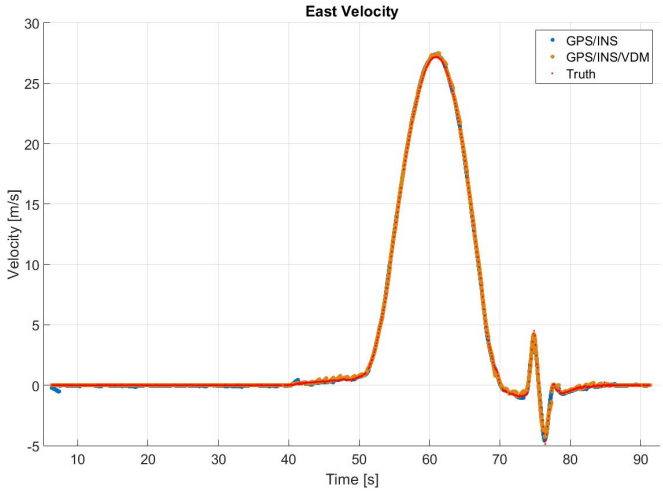

Figure B.9: Double Lane Change Velocity East Truth Compare

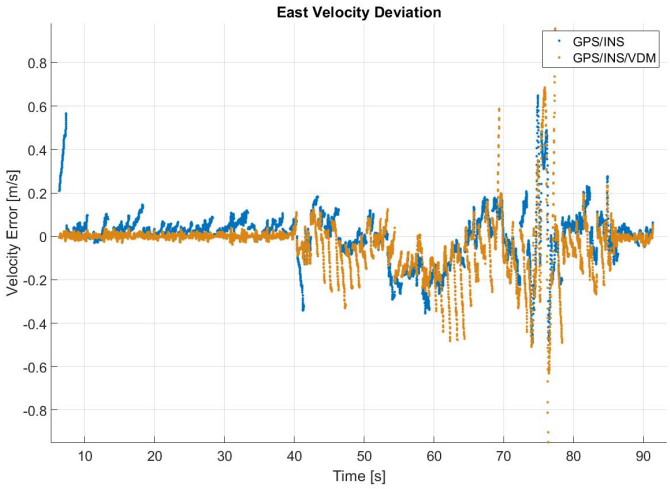

Figure B.10: Double Lane Change East Velocity Deviation from Truth Velocity

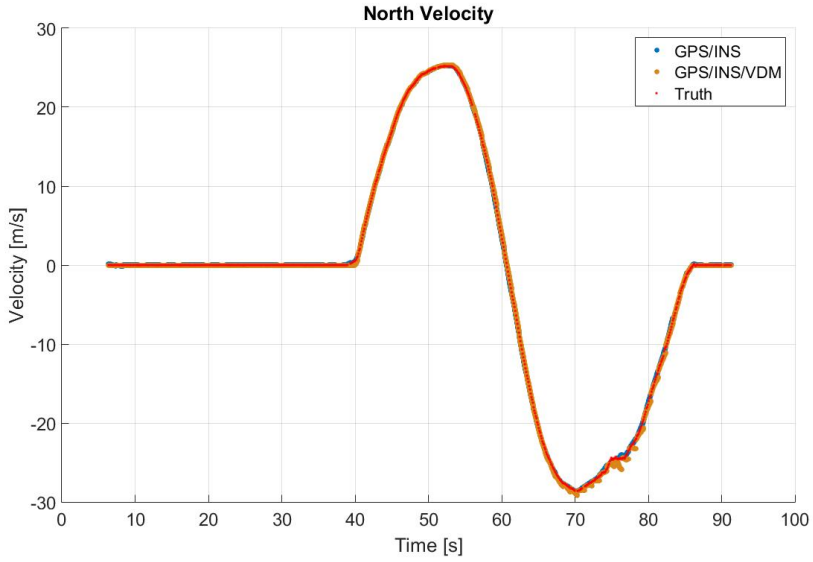

Figure B.11: Double Lane Change Velocity North Truth Compare

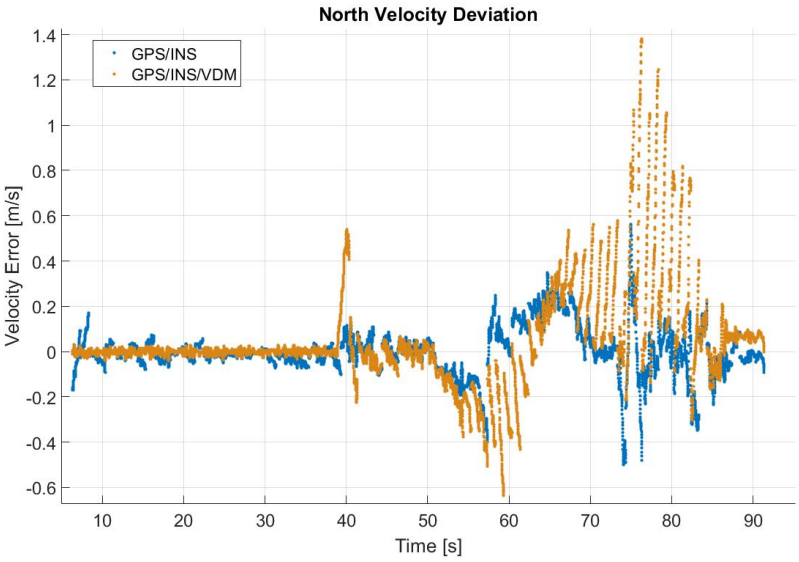

Figure B.12: Double Lane Change North Velocity Deviation from Truth Velocity Solution

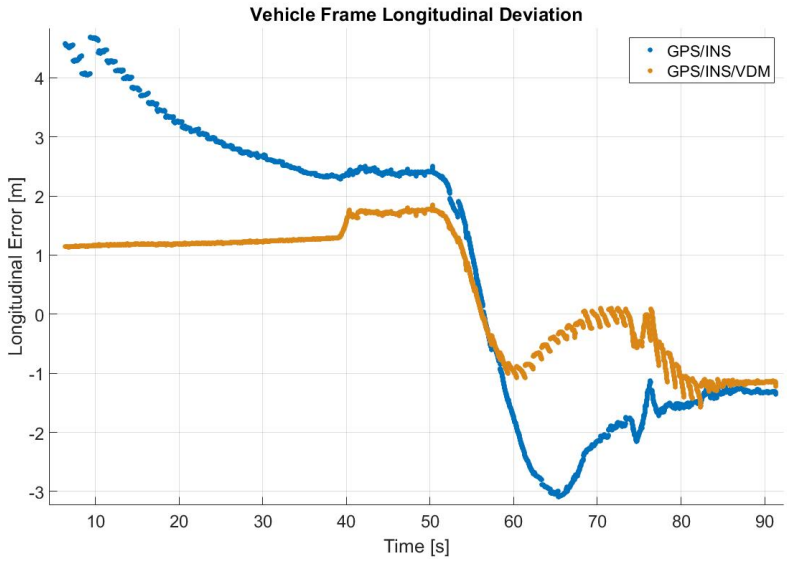

Figure B.13: Double Lane Change Vehicle Body Frame Longitudinal Position Error

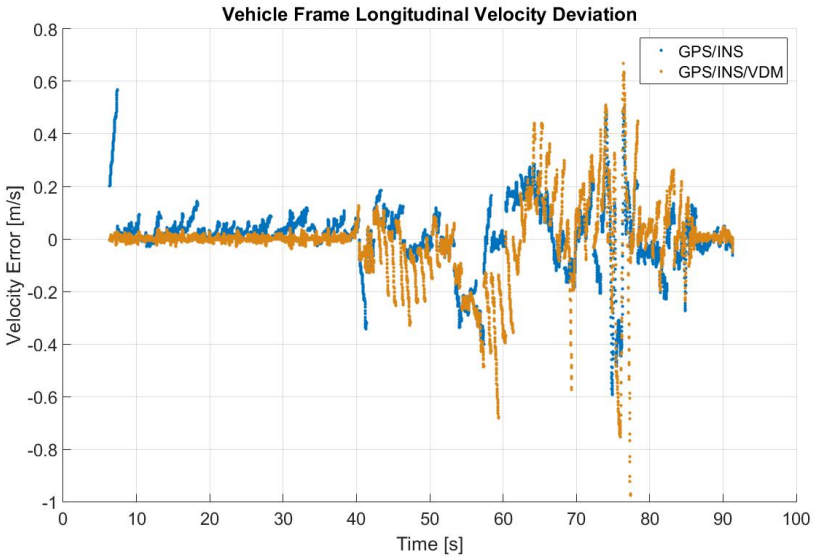

Figure B.14: Double Lane Change Vehicle Body Frame Longitudinal Velocity Error

B.3 GPS/INS/VDM CCF

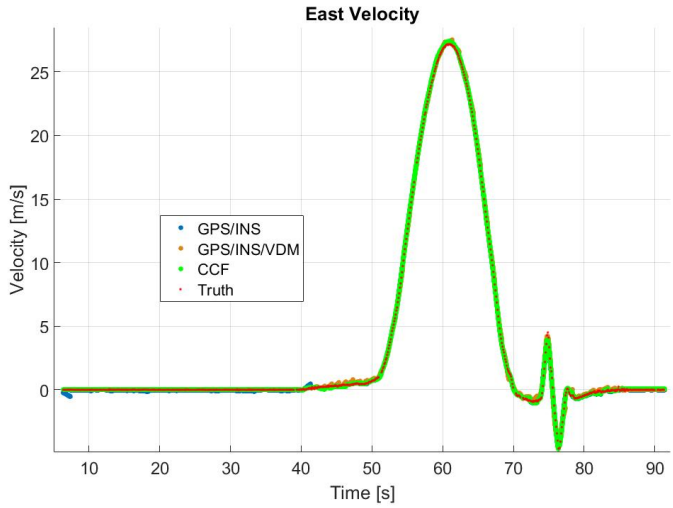

Figure B.15: Double Lane Change Velocity East Truth Compare

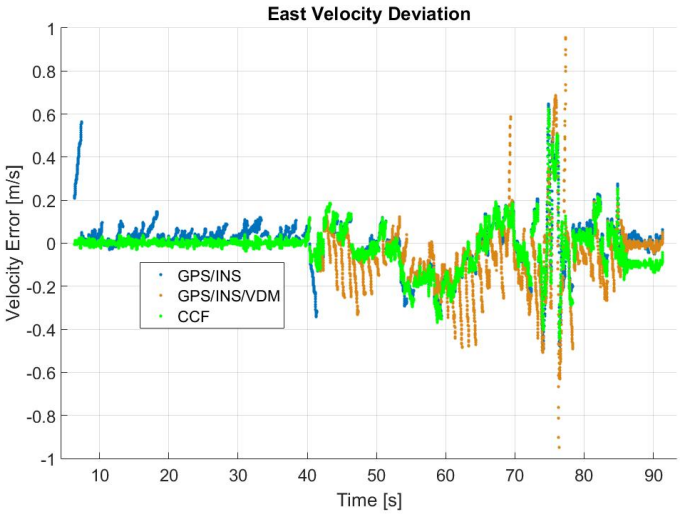

Figure B.16: Double Lane Change East Velocity Deviation from Truth Velocity

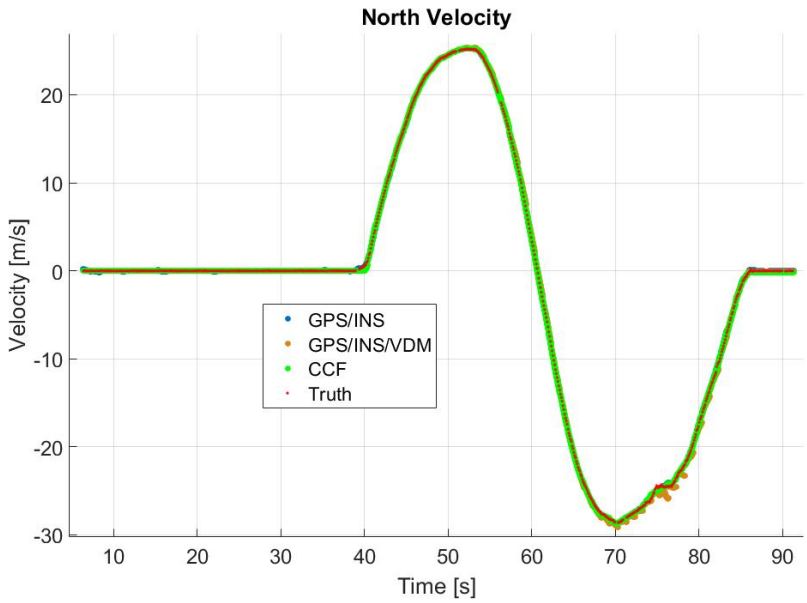

Figure B.17: Double Lane Change Velocity North Truth Compare

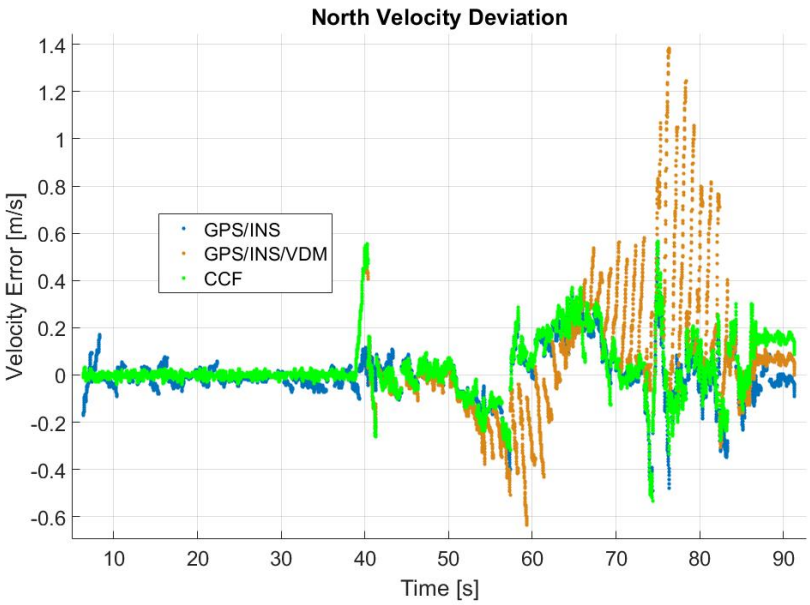

Figure B.18: Double Lane Change North Velocity Deviation from Truth Velocity Solution

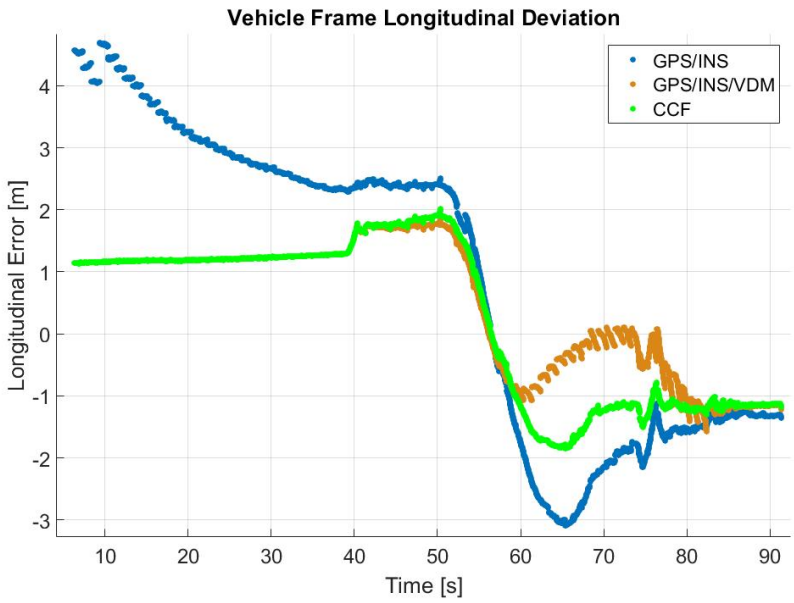

Figure B.19: Double Lane Change Vehicle Body Frame Longitudinal Position Error

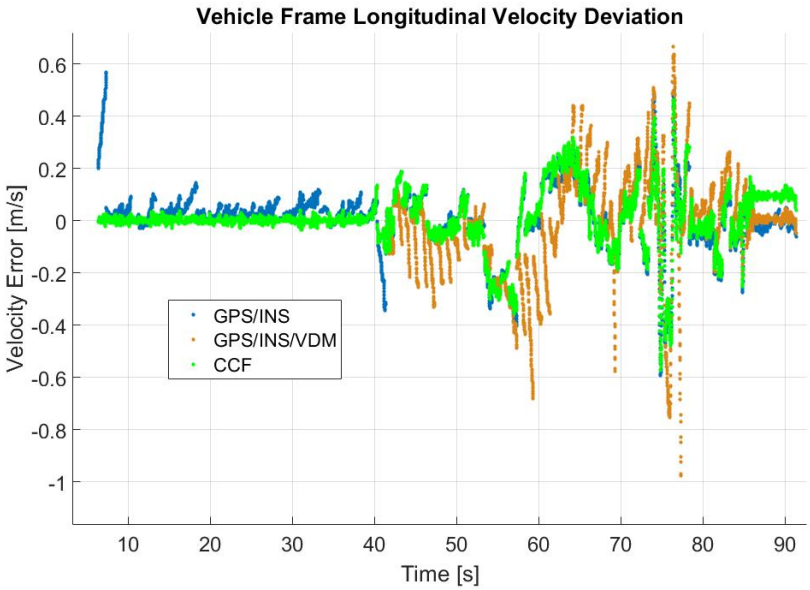

Figure B.20: Double Lane Change Vehicle Body Frame Longitudinal Velocity Error

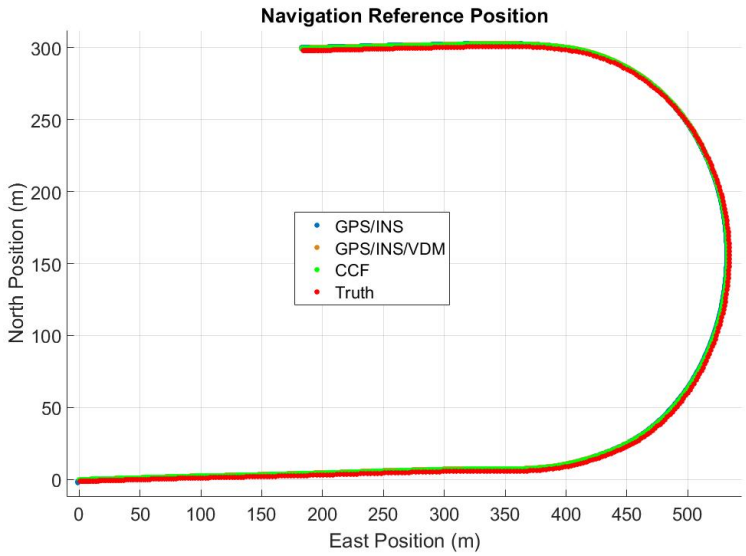

Figure B.21: High Speed Banked Turn at NCAT Track

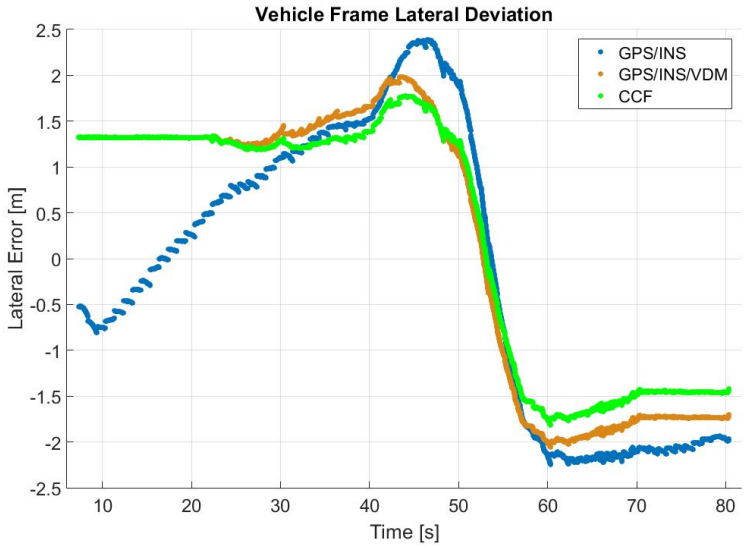

Figure B.22: 65 mph Track Vehicle Frame Lateral Position Deviation from Ground Truth

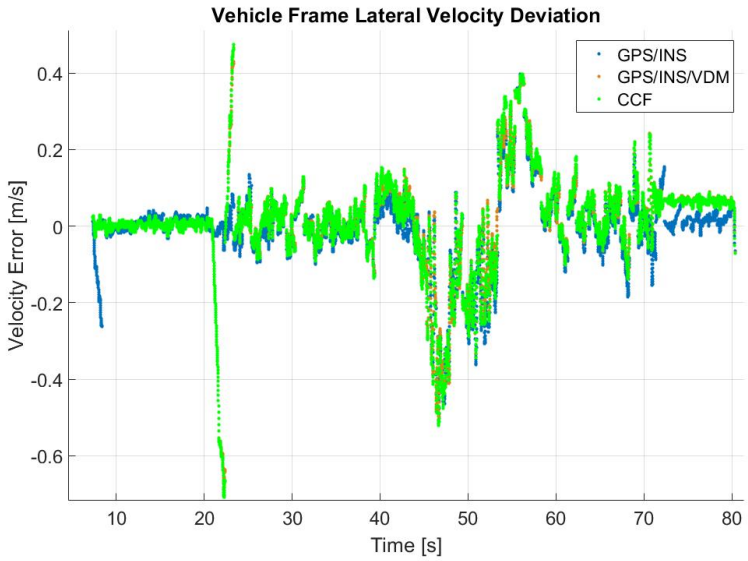

Figure B.23: 65 mph Track Vehicle Frame Lateral Velocity Deviation from Ground Truth

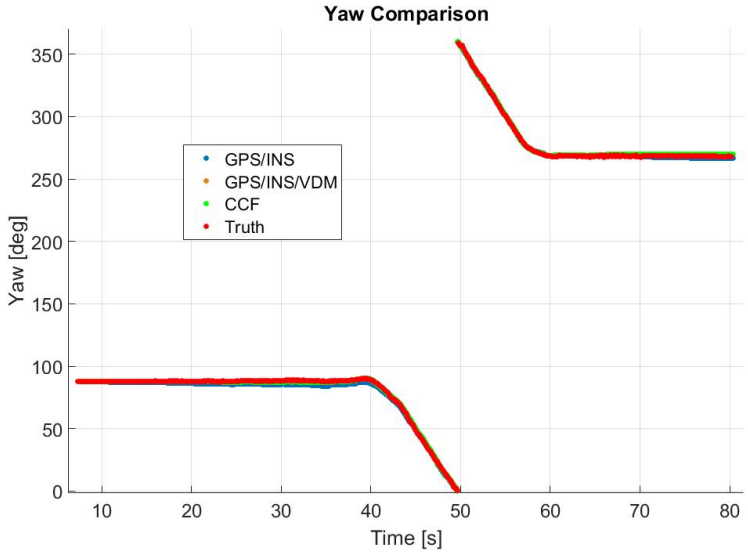

Figure B.24: 65 mph Track Vehicle Yaw Visualization

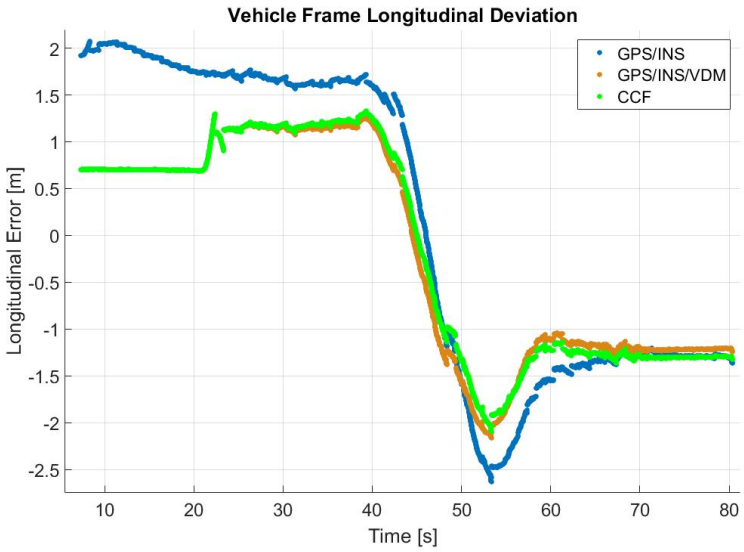

Figure B.25: 65 mph Track Vehicle Frame Longitudinal Position Deviation from Ground Truth

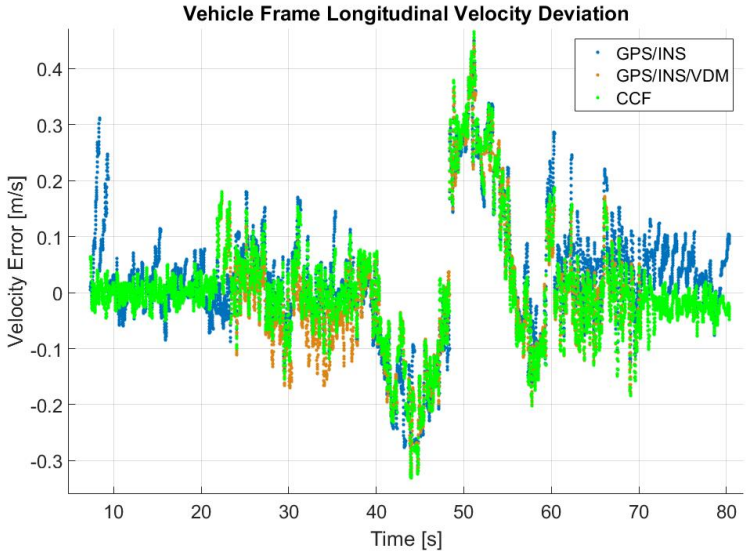

Figure B.26: 65 mph Track Vehicle Frame Longitudinal Velocity Deviation from Ground Truth